

**A Precision Search for Exotic Scalar and Tensor Couplings in  
the Beta Decay of Polarized  $^{37}\text{K}$**

by

Melissa Anholm

A Thesis submitted to the Faculty of Graduate Studies of  
The University of Manitoba  
in partial fulfillment of the requirements of the degree of

DOCTOR OF PHILOSOPHY

Department of Physics and Astronomy  
University of Manitoba  
Winnipeg

# Abstract

The nuclear weak interaction is known to feature both vector and axial-vector couplings in a dominant role, however the presence of scalar and tensor couplings cannot be ruled out entirely. In beta decay physics, the Fierz interference,  $b_{\text{Fierz}}$ , is an observable comprised of a linear combination of scalar and tensor couplings, and can be measured as an adjustment to the shape of the resultant beta energy spectrum. A precision measurement experiment is conducted to observe the  $\beta^+$  decay of spin-polarized  $^{37}\text{K}$  from an atom cloud intermittently confined by a magneto-optical trap, and the beta energy spectra are observed in two detectors on opposing sides of the cloud, along the axis of polarization. This geometry, combined with a knowledge of the polarization, allows the superratio asymmetry to be constructed, providing an observable which is particularly sensitive to the value of  $b_{\text{Fierz}}$ , while simultaneously eliminating contributions from a variety of systematic effects. Geant4 simulations are used to model scattering effects that could mimic the signal being searched for. The resulting measurement gives  $b_{\text{Fierz}} = +0.033 \pm 0.084(\text{stat}) \pm 0.039(\text{syst})$ , consistent with the Standard Model.

# Acknowledgements

People to acknowledge here include: John Behr, Gerald Gwinner, Dan Melconian.  
Also: Spencer Behling, Ben Fenker, Alexandre Gorelov, James McNeil, Danny Ashery.

# Contents

<b>Abstract</b>	ii
<b>Acknowledgements</b>	iii
<b>Contents</b>	vi
<b>List of Figures</b>	vii
<b>List of Tables</b>	ix
<b>1 Background</b>	1
1.1 Beta Decay within the Standard Model . . . . .	1
1.2 A Generalized Description of the Weak Interaction . . . . .	3
1.3 Mathematical Formalism . . . . .	4
1.4 Our Decay . . . . .	5
1.5 The Shake-off Electron Spectrum . . . . .	7
1.6 Fierz Interference – The Physical Signature . . . . .	8
<b>2 Considerations and Implementation of Atomic Techniques</b>	10
2.1 An Overview of Magneto-Optical Traps . . . . .	10
2.1.1 Zeeman Splitting . . . . .	11
2.1.2 Doppler Cooling . . . . .	11
2.1.3 Atom Trapping with a MOT . . . . .	12
2.2 Optical Pumping . . . . .	13
2.3 An Overview of the Double MOT System and Duty Cycle . . . . .	13
2.4 The AC-MOT and Polarization Setup . . . . .	17
2.5 Measurement Geometry and Detectors . . . . .	19
2.5.1 Microchannel Plates and Electrostatic Hoops . . . . .	19
2.5.2 Beta Detectors . . . . .	20
2.5.3 The Photoionization Laser . . . . .	23

<b>3</b>	<b>Calibrations and Data Selection</b>	<b>25</b>
3.1	An Overview of Available Data . . . . .	25
3.2	Preliminary Data Selection with the rMCP . . . . .	27
3.3	Calibrations with the rMCP . . . . .	30
3.4	Measurements of the Atom Cloud . . . . .	35
3.5	Electron Run Data Selection and Preliminary Cuts . . . . .	38
3.6	Further Cuts Using the DSSD . . . . .	40
3.7	Further Cuts Using the Scintillators . . . . .	41
3.8	Timing Improvements with the Leading Edge and Scintillator Walk Correction . . . . .	42
<b>4</b>	<b>Simulations</b>	<b>46</b>
4.1	Considerations for Software Upgrade Implementation . . . . .	46
4.2	Simulations for the Ninety-eight Percent Branch and the Two Percent Branch . . . . .	48
4.3	The Simple Monte Carlo and Response Function . . . . .	49
4.4	Modeling the Scattering Effects from the Cloud . . . . .	63
4.5	Simulating the Background and Time of Flight . . . . .	66
<b>5</b>	<b>Analysis and Estimates of Systematic Effects</b>	<b>71</b>
5.1	Comparing Simulations to Experimental Data: The General Methodology . . . . .	71
5.2	Evaluation of Systematic Effects . . . . .	79
5.2.1	Beta Scattering . . . . .	79
5.2.2	Detector Calibrations and Thresholds . . . . .	80
5.2.3	The Atomic Cloud . . . . .	82
5.2.4	The Response Function's Low Energy Tail . . . . .	86
5.2.5	Background Events . . . . .	86
5.2.6	Material Thicknesses . . . . .	86
<b>6</b>	<b>Results and Conclusions</b>	<b>88</b>
6.1	Measured Limits on $b_{Fierz}$ and $A_\beta$ . . . . .	88
6.2	Other Possible Future Work for the Collaboration: $R_{\text{slow}}$ . . . . .	91
6.2.1	Motivation . . . . .	91
6.2.2	The Decay Process . . . . .	92
6.2.3	Status of the $R_{\text{slow}}$ Measurement . . . . .	93
6.3	Conclusions . . . . .	94
<b>Bibliography</b>		<b>95</b>
<b>Appendices</b>		<b>98</b>

<b>A Notable Differences in Data Selection between this and the Previous Result</b>	<b>98</b>
A.1 Polarization Cycle Selection . . . . .	98
A.2 Leading Edge / Trailing Edge and Walk Correction . . . . .	98
A.3 TOF Cut + Background Modelling . . . . .	98
A.4 BB1 Energy Threshold . . . . .	99
<b>B A PDF</b>	<b>100</b>
B.1 JTW . . . . .	100
B.2 Holstein . . . . .	102
<b>C Notation</b>	<b>108</b>
<b>D SuperRatio</b>	<b>118</b>

# List of Figures

1.1	A level diagram for the decay of $^{37}\text{K}$ . . . . .	6
1.2	Naive Beta Energy Spectrum and Superratio Asymmetry to Measure $b_{\text{Fierz}}$ . . . . .	9
2.1	Components of a Magneto-Optical Trap . . . . .	14
2.2	The TRINAT experimental set-up, viewed from above . . . . .	15
2.3	The 2014 duty cycle for transferring, cooling, trapping, and optically pumping $^{37}\text{K}$ . . . . .	16
2.4	The AC-MOT and Optical Pumping Cycle . . . . .	17
2.5	Diagram of the TRINAT Detection Chamber . . . . .	21
2.6	A Photo from Inside the TRINAT Detection Chamber . . . . .	22
3.1	Timing sums for the rMCP, run 447. . . . .	29
3.2	Cloud Position for run 447 for various rMCP timing sum cuts . . . . .	30
3.3	rMCP Calibration . . . . .	33
3.4	Photoion Hit Positions in 2D . . . . .	34
3.5	Photoion Hit Positions at 535 V/cm, as a function of AC-MOT Time	37
3.6	LE and TE Timing Peaks . . . . .	43
3.7	SOE TOF Walk and Correction . . . . .	44
3.8	Experimental Scintillator Spectra . . . . .	45
4.1	Fit to Mono-Energetic Spectrum, 5000 keV . . . . .	54
4.2	Fit to Mono-Energetic Spectrum, 3000 keV . . . . .	55
4.3	Fit to Mono-Energetic Spectrum, 1500 keV . . . . .	56
4.4	Fit to Mono-Energetic Spectrum, 1000 keV . . . . .	57
4.5	Fit to Mono-Energetic Spectrum, 750 keV . . . . .	58
4.6	Lineshape Parameter Fits (Part 1) . . . . .	59
4.7	Lineshape Parameter Fits (Part 2) . . . . .	60
4.8	Lineshape Parameter Fits (Part 3) . . . . .	61
4.9	Lineshape Parameter Fits (Part 4) . . . . .	61
4.10	Goodness of Fit for Modeled Response Functions . . . . .	62

4.11	Simulated Beta emission angle w.r.t. the detector vs adjusted SOE–Beta TOF . . . . .	66
4.12	(SOE–Beta) TOF . . . . .	69
4.13	Averaged Superratio Asymmetry by TOF . . . . .	70
5.1	SetB Superratio Asymmetry . . . . .	73
5.2	SetC Superratio Asymmetry . . . . .	74
5.3	SetD Superratio Asymmetry . . . . .	75
5.4	$\chi^2$ Map for Runset B . . . . .	76
5.5	$\chi^2$ Map for Runset C . . . . .	77
5.6	$\chi^2$ Map for Runset D . . . . .	78
5.7	Scattering Effects in the Asymmetry . . . . .	80
5.8	Response Function Comparison . . . . .	83
5.9	$A_\beta$ Position Error . . . . .	84
5.10	$b_{\text{Fierz}}$ Position Error . . . . .	85
6.1	$\chi^2$ Map for All Data . . . . .	89
C.1	"Notes 0" . . . . .	112
C.2	"Notes 1" . . . . .	113
C.3	"Notes 2" . . . . .	114
C.4	"Notes 3" . . . . .	115
C.5	"Notes 4" . . . . .	116
C.6	"Notes 5" . . . . .	117

# List of Tables

3.1	List of Electron Runs . . . . .	26
3.2	List of Recoil Runs . . . . .	26
3.3	Cloud Position and Size . . . . .	36
5.1	Scintillator Calibrations . . . . .	81
6.1	Error Budget . . . . .	90
C.1	Kinematic Terms Guide . . . . .	109
C.2	Angular Momentum Notation . . . . .	109
C.3	Multipole Notation . . . . .	110
C.4	Selected Integrals from Holstein's Eq. (51) . . . . .	111

# Chapter 1

## Background

The nuclear weak force is one of four fundamental forces described within physics. It mediates the process of beta decay, which is of particular interest to us here. Although beta decay is generally well understood, it presents a unique opportunity for precision measurements to search for physics beyond the Standard Model within the Weak coupling. By observing the kinematics and angular correlations involved in the decay process, one gains access to a wealth of information about the form of the operators mediating the decay.

### 1.1 Beta Decay within the Standard Model

A nucleus undergoing beta decay converts one of its protons (neutrons) into a neutron (proton), and simultaneously emits a lepton and anti-lepton. The daughter nucleon remains bound in place of its parent, and the overall electric charge of the nucleus is changed by -1 (+1), with the extra charge being carried away by the anti-lepton (lepton). In particular, at the nucleon level, three beta decay processes are possible:

$$p \rightarrow n + e^+ + \bar{\nu}_e \tag{1.1}$$

$$n \rightarrow p + e^- + \nu_e, \tag{1.2}$$

$$p + e^- \rightarrow n + \nu_e \tag{1.3}$$

where the processes described in Eqs. 1.1 and 1.3 are energetically disallowed for an unbound proton, however there is no similar requirement for Eq. 1.2.

Limiting the focus of this discussion to Eq. 1.1, we note that this expression provides no information at all about the momenta or spin of the outgoing daughter particles. This behaviour is governed by the form of the Weak coupling that mediates the decay.

Within the field of nuclear physics, it is common to classify beta decay processes as being either “Allowed” or “Forbidden” (sometimes with an associated number to describe the extent to which it is Forbidden), where Forbidden processes are generally suppressed but not truly forbidden. In an Allowed transition, the positron and anti-neutrino are treated as being created at the nuclear centre, and as a result they may not carry away any *orbital* angular momentum. However, since the outgoing leptons both have spin  $S = 1/2$ , it is still possible for the total nuclear angular momentum,  $J$ , to be changed in an Allowed decay. This implies that an Allowed transition must *always* change the total nuclear angular momentum by either 0 or  $\pm 1$ .

The Allowed decays traditionally are further separated into a “Fermi” singlet in which there is no change to nuclear angular momentum ( $\Delta J = 0$ ) and therefore the two leptons are required to have anti-parallel spins, and a “Gamow-Teller” triplet [1], where the projection of the nuclear angular momentum is changed by  $\pm 1$ .

This implies that the total nuclear angular momentum is changed by  $\Delta J = \{0, \pm 1\}$  during a Gamow-Teller transition. A mixed transition is also possible, however we note that the  $J_i = J_f = 0$  decays must always be pure Fermi transitions, because there is no way to produce this result from two outgoing leptons with parallel spins. [2] [3] [1].

Given the differing behaviour within the angular momenta of the daughters in Fermi and Gamow-Teller transitions, it is perhaps not surprising that that the *linear* momenta of the outgoing particles should also follow a different set of distributions in these two cases. At the level of the Weak coupling, Fermi- and Gamow-Teller transitions are governed by different operators, with the Fermi interaction mediated by a so-called “vector” ( $V$ ) coupling, and the Gamow-Teller interaction mediated by an “axial-vector” ( $A$ ) coupling.

## 1.2 A Generalized Description of the Weak Interaction

According to the predictions of the Standard Model (SM), the Weak force involves only vector ( $V$ ) and axial-vector ( $A$ ) couplings, where a relative sign within the quark-lepton Lagrangian produces the left-handed “( $V - A$ )” form of the interaction in maximal violation of parity. In terms of physical behaviour, one consequence of this model is that “regular matter” leptons emerge from a Weak interaction with left-handed chirality, while antimatter leptons emerge with right-handed chirality. Any deviation from this behavior would be indicative of “new” or “exotic” (i.e., not previously discovered) physics.

There exists an extensive body of experimental evidence to demonstrate that the above model is overall a very good description of the beta decay process [4]. Despite the success of the ( $V - A$ ) model, there are still certain lingering questions that must be addressed by precision measurements. Any deviation from maximal parity violation (i.e., a “( $V + A$ )” contribution to the Weak force) would be of great interest to the community, as would the presence of certain other exotic couplings, such as the so-called Scalar ( $S$ ) and Tensor ( $T$ ) interactions. Any such behaviour beyond the Standard Model (BSM) would represent a non-dominant contribution to the interaction, however the possibility cannot be entirely ruled out.

The generalized nucleon-level Lagrangian to describe the Weak interaction including BSM behaviour is given by:

$$\begin{aligned} \mathcal{L} = & -\bar{p}\gamma^\mu n \left( C_V^+ \bar{e} \gamma_\mu \nu_L + C_V^- \bar{e} \gamma_\mu \nu_R \right) - \bar{p}\gamma^\mu \gamma_5 n \left( C_A^+ \bar{e} \gamma_\mu \nu_L - C_A^- \bar{e} \gamma_\mu \nu_R \right) \\ & - \bar{p}n \left( C_S^+ \bar{e} \nu_L + C_S^- \bar{e} \nu_R \right) - \frac{1}{2} \bar{p}\sigma^{\mu\nu} n \left( C_T^+ \bar{e} \sigma_{\mu\nu} \nu_L + C_T^- \bar{e} \sigma_{\mu\nu} \nu_R \right) \\ & + \bar{p}\gamma_5 n \left( C_P^+ \bar{e} \nu_L - C_P^- \bar{e} \nu_R \right) + \text{H.C.}, \end{aligned} \quad (1.4)$$

where the coupling constants  $C_X^\pm$  (with  $X = \{V, A, S, T, P\}$ ) are written in such a way as to separate out the left-handed ( $C_X^+$ ) and right-handed ( $C_X^-$ ) components from one another, and the neutrino fields  $\nu_{L,R}$  are given a similar treatment. A simple variable transform relates Eq. 1.4 to expressions that are potentially more familiar from the older literature, much of which was written before it had been determined that the

Weak force is primarily or entirely left-handed:

$$\nu_L = \frac{1}{2}\nu(1 + \gamma_5) \quad (1.5)$$

$$\nu_R = \frac{1}{2}\nu(1 - \gamma_5) \quad (1.6)$$

$$C_X = \frac{1}{2}(C_X^+ + C_X^-) \quad (1.7)$$

$$C'_X = \frac{1}{2}(C_X^+ - C_X^-) \quad (1.8)$$

It can be seen from the form of the Lagrangian that the  $V, A, S, T, P$  couplings within are described as such because they *behave* as vectors, axial-vectors, scalars, tensors, and pseudoscalars (respectively) under a Lorentz transform, where the Lagrangian itself must be a scalar both before and after a Lorentz transform [5] [6] [7].

### 1.3 Mathematical Formalism

In a beta decay event, conservation of energy and momentum are of course required, but those conditions alone cannot provide a full description of the kinematics of emitted particles. The distribution of energy and momenta is probabilistic rather than deterministic with three bodies involved, and the full probability distribution for the momenta of outgoing particles cannot be written in closed form.

Because the nucleus is significantly more massive than either of the other two outgoing particles, the great majority of the released kinetic energy is distributed between the leptons, while the nucleus receives only a tiny fraction of the total. This feature lends itself to an approximation in which the energy of the recoiling nucleus (the ‘recoil’) is neglected entirely, and the decay may be described only in terms of the momenta of the outgoing positron(electron) and neutrino(anti-neutrino), as in the description from Jackson, Treiman, and Wylde (JTW) [8] [9]. The terms that have been neglected in this treatment are sometimes called ‘recoil-order corrections’.

In order to proceed with a measurement, we must find an equation to describe the probability of beta decay events with any given distribution of energy and momenta among the daughter particles, as a function of the strength of the specific couplings of interest to us. To do this, two sets of formalisms are combined – the older formalism of JTW, which describes the effects of all types of Standard Model and exotic cou-

plings of interest to us here, but which truncates its expression at first order in the (small) parameter of transferred nuclear recoil energy, and a newer formalism from Holstein [10], which includes terms up to several orders higher in recoil energy, but which does not include any description of the exotic couplings of particular interest to us. We note that because any exotic couplings present in nature have already been determined to be either small or nonexistent, it is sufficient to describe these parameters with expressions truncated at first order, despite the fact that it is still necessary to describe the larger Standard Model couplings with higher-order terms.

The procedure for combining the two formalisms is described in detail in Appendix B. Integrating the JTW expression over neutrino direction, we find:

$$\begin{aligned} d^3\Gamma dE_\beta d^3\hat{\Omega}_\beta &= \frac{2}{(2\pi)^4} F_{\mp}(Z, E_\beta) p_\beta E_\beta (E_0 - E_\beta)^2 dE_\beta d^3\hat{\Omega}_\beta \xi \\ &\times \left[ 1 + b_{\text{Fierz}} \frac{m_e c^2}{E_\beta} + A_\beta \left( \frac{\vec{J}}{J} \cdot \frac{\vec{p}_\beta}{E_\beta} \right) \right], \end{aligned} \quad (1.9)$$

where a comparison with Holstein's treatment yields the relation,

$$\xi = G_v^2 \cos \theta_C f_1(E). \quad (1.10)$$

## 1.4 Our Decay

Here, we will focus on the decay,



which is extremely well suited to the type of experiment to be discussed in this thesis. The parent,  $^{37}\text{K}$ , is an isotope of potassium—an alkali. Though this fact may initially seem unremarkable, it is their ‘hydrogen-like’ single valence electron which allows alkalis to be readily trapped within a magneto-optical trap, a critical component of our experimental design (see Chapter 2).

A potential concern in any experiment concerned with the angular correlations resulting from one particular decay branch is the background from competing decay branches. As can be seen in Fig. 1.1, the decay of  $^{37}\text{K}$  is dominated by a single branch which contributes nearly 98% of  $^{37}\text{K}$  decay events, and the remaining events nearly

all arise from a single branch contributing around 2% of the decay events. The other branches combined account for only around 0.04% of decays. Taken all together, this means that the background events which must be accounted for are both infrequent and well understood.

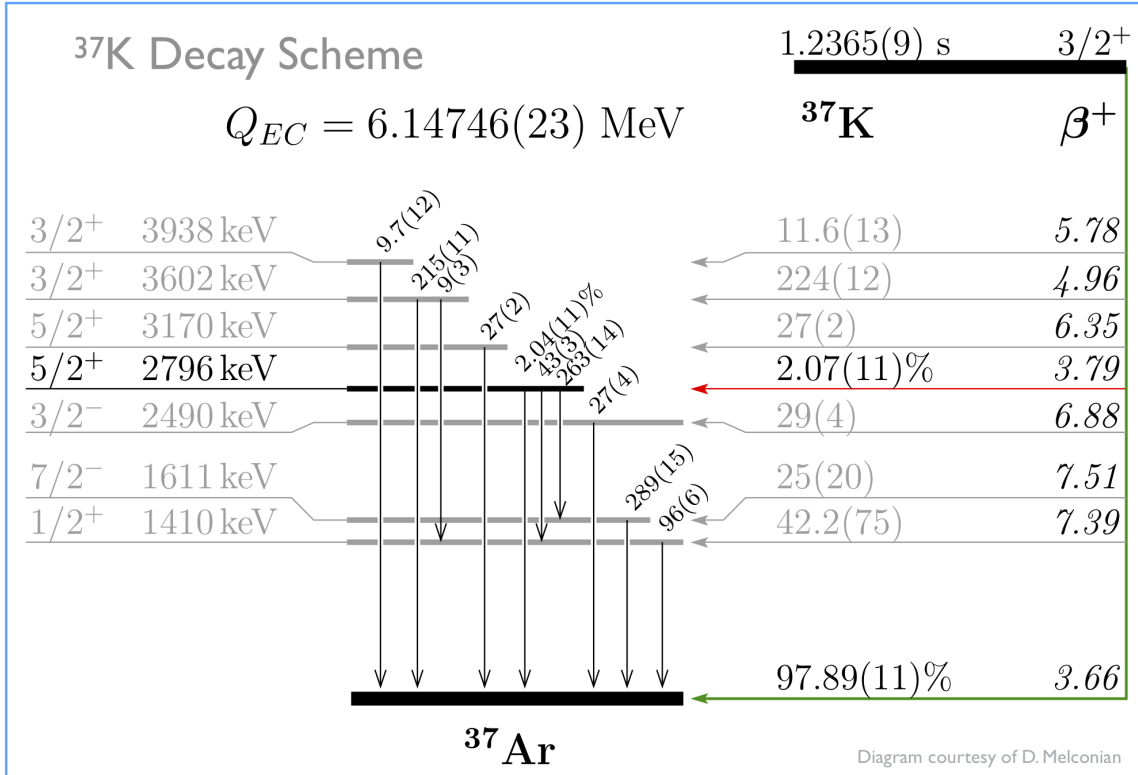


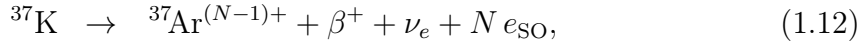
Figure 1.1: A level diagram for the decay of  $^{37}\text{K}$ .

As in any decay, the angular correlations between the emerging daughter particles provide a rich source of information about the type of interaction that produced the decay. This particular decay involves a set of ‘mirror’ nuclei, meaning that the nuclear wavefunctions of the parent and daughter are identical up to their isospin quantum number and corresponding electrical charge. Because the two wavefunctions are so similar, effects to the decay from nuclear structure corrections can be kept to a minimum, and it is therefore possible to place especially strong constraints on the size of the theoretical uncertainties associated with the decay.

## 1.5 The Shake-off Electron Spectrum

Although the beta decay process is primarily concerned with the emission of beta particles (electrons or positrons) from a Weak interaction that occurs within the nucleus, it is common for one or more *orbital* electrons to also be lost in the process. Although beta particles are emitted over a continuous energy spectrum, they commonly carry several MeV of kinetic energy. By contrast, an atomic electron that becomes unbound in this process is likely to only carry a few eV of kinetic energy, and we say that they are ‘shaken’ off.

We will amend Eq. 1.11 to reflect the presence of  $N$  such ‘shake-off electrons’ (SOEs) within each decay event, as



where it is clear that, since the parent  ${}^{37}\text{K}$  atom was electrically neutral before its decay by  $\beta^+$  emission, the daughter  ${}^{37}\text{Ar}$  will initially have an ‘extra’ orbital electron (and therefore a negative net charge) if no electrons are shaken off. We also note that it is common for multiple SOEs to be created in a given decay event.

A further consideration is that the outer electron in an  ${}^{37}\text{Ar}^-$  ion is *not bound*, and in an electric field such as is present within our experimental chamber, this outer electron is removed immediately to be accelerated through the field, leaving behind a neutral  ${}^{37}\text{Ar}$  atom. Although this is in principle a different physical loss mechanism, we will refer to unbound electrons resulting from either process as SOEs.

It is useful to consider the energy spectrum of these shake-off electrons. The most straightforward component of the SOE energy spectrum arises from the electrons that are lost immediately following decay, and we take these to initially have 0eV in kinetic energy.

For the shake-off electrons arising from the Weak process itself, the initial energy spectra for SOEs originating in a particular orbital shell can be estimated according to the procedure outlined by Levinger [11]. The strategy is to assume that the sudden approximation holds, and simply calculate the overlap in electron wavefunctions between the initial and final states, where the final state may be either an outgoing electron or one bound within the atom. Analytic expressions can be obtained if the atom is treated as being hydrogenic – an excellent approximation here, as  ${}^{37}\text{K}$  is an

alkali.

Unfortunately, this treatment cannot determine the fractional contribution of each orbital to the total, nor can it determine the *number* of electrons likely to be removed in a single decay event. The implications of the SOE energy spectrum to the present experiment are discussed further in Section 4.5.

## 1.6 Fierz Interference – The Physical Signature

The physical effects resulting from the presence of scalar or tensor couplings include a small perturbation to the energy spectrum of betas produced by radioactive decay, labeled  $b_{\text{Fierz}}$  in Eq. B.3. Within the Standard Model, the parameter  $b_{\text{Fierz}}$  is identically zero, and a departure from that would be indicative of (BSM) scalar or tensor couplings.

The measured value of  $b_{\text{Fierz}}$  can be evaluated by using a simple beta energy spectrum, as in the top plot of Fig. 1.2, but by constructing a so-called “superratio asymmetry” instead (bottom plot in Fig. 1.2), these small changes to the overall spectrum are amplified, and many systematic effects cancel out entirely. This result comes at the cost of an increased statistical uncertainty.

The superratio and superratio asymmetry are discussed in detail in Appendix D. The discussion includes details on which sort of systematic errors will cancel out entirely, or to leading order, with this treatment – however it must be noted that for this project, higher-order corrections are included in all simulations, and the effects are propagated through to the end of the analysis. Therefore, measured values of  $A_\beta$  (and  $b_{\text{Fierz}}$ , though that is trivial) may be directly compared to theoretical predictions.

The data can be combined into a superratio asymmetry. This has the benefit of causing many systematics to cancel themselves out at leading order. It also will increase the fractional size of the effects we’re looking for. This can be shown by using math.

Not all systematics effects are eliminated. We’ll want to be careful to propagate through any effects that are relevant. Using the superratio asymmetry as our physical observable makes this process a bit messier for the things that don’t cancel out, but it’s all just math. Some other groups have performed similar measurements using the supersum as the physical observable. There are pros and cons to both methods. I

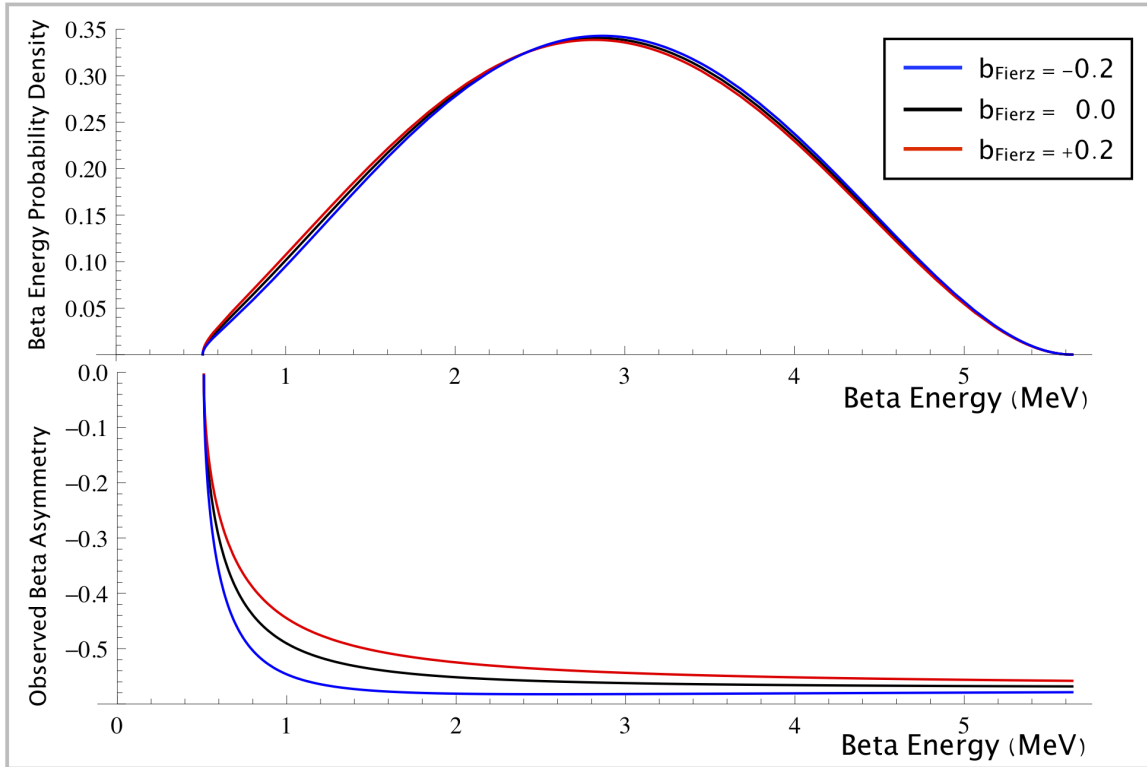


Figure 1.2: A naive beta energy spectrum (top) and superratio asymmetry (bottom) are constructed to measure  $b_{\text{Fierz}}$ .

can show, using a back-of-the-envelope calculation, that for this particular dataset, the superratio asymmetry method produces a better result.

# Chapter 2

## Considerations and Implementation of Atomic Techniques

### 2.1 An Overview of Magneto-Optical Traps

Since its initial description by Raab et. al. in 1987 [12], the magneto-optical trap (MOT) has become a widely used technique in many atomic physics laboratories. The MOT produces confined samples of cold, electrically neutral and isotopically pure atoms confined within a small spatial region. It is these properties that make the MOT a valuable tool not only in atomic physics, but for precision measurements in nuclear physics as well, and the TRIUMF Neutral Atom Trap (TRINAT) collaboration has adopted the technique wholeheartedly.

The technique is used predominantly with alkalis due to their simple orbital electron structure, and once set up it is quite robust. The MOT's trapping force is specific to the isotope for which the trap has been tuned. This feature makes it ideal for use in precision radioactive decay experiments, since the daughters are unaffected by the trapping forces keeping the parent confined.

A typical MOT can be created from relatively simple components: a quadrupole-shaped magnetic field, typically generated by two current-carrying coils of wire, and a circularly polarized laser tuned to match one or more atomic transitions in the isotope of interest. Because a MOT is easily disrupted by interactions with untrapped atoms, the trap must be created within a vacuum system. Finally, a source of atoms to be trapped is required. See Fig. 2.1.

In order to understand the mechanism by which a MOT is able to confine atoms, we must first introduce the Zeeman effect (Section 2.1.1) and a description of an optical molasses (Section 2.1.2). A functional MOT combines the forces resulting from these two physical effects to trap and cool atoms.

### 2.1.1 Zeeman Splitting

In the presence of an external magnetic field  $\vec{B}$ , the Hamiltonian associated with an atom's orbital electrons will acquire an additional "Zeeman Shift" term, given by [13]

$$H_{\text{Zeeman}} = -\vec{\mu} \cdot \vec{B}, \quad (2.1)$$

where  $\vec{\mu}$  is the magnetic moment associated with the orbital under consideration. In the limit where the magnetic field is too weak to significantly disrupt the coupling between the electron's spin- and orbital angular momenta,  $\vec{\mu}$  may be treated as being fixed with respect to changes in the magnetic field. It is this weak field regime which will be primarily of interest to us in work with magneto-optical traps.

With  $\vec{\mu}$  fixed, it is clear that the magnitude of the energy shift must scale linearly with the strength of the magnetic field. In considering the perturbation to the energy of a particular *transition*, the perturbations to the initial and final states must of course be subtracted:

$$\Delta E_{\text{transition}} = -(\vec{\mu}_f - \vec{\mu}_i) \cdot \vec{B}. \quad (2.2)$$

### 2.1.2 Doppler Cooling

We consider a setup in which a cloud of two-level atoms lies along the path of two counter-propagating laser beams, both tuned to resonance. For simplicity, we treat this cloud as being one dimensional along the axis of laser propagation. With two counter-propagating laser beams of equal intensity and detuning, the "push" from interaction with one beam is, on average within the lab frame, perfectly counteracted by the push from the opposite-propagating beam, so there is no net velocity transfer to a cloud initially at rest. These pushes, however, are applied on the level of the individual atom, and are the result of individual photons being absorbed and emitted.

Because this process is probabilistic rather than deterministic, each individual atom will undergo a random walk.

We now consider the effect of detuning on this process. We will suppose that both lasers are equally detuned slightly to the red of resonance. This will obviously decrease absorption by atoms at rest within the lasers' path – however the atoms within the cloud are not at rest, but rather are undergoing thermal motion. As such, within the rest frame of each individual atom, the two laser beams will appear to be Doppler shifted in opposite directions, with the sign dependent on atomic motion. In particular, atoms moving against a laser's direction of propagation will see that laser beam as being blueshifted within their own rest frame. Since the laser was redshifted relative to resonance within the lab frame, adding an additional blueshift will serve to bring the photons' energy back towards resonance, making them more likely to be absorbed. For this same atom, the laser propagating in the same (lab frame) direction as the atom itself will appear further redshifted, and its photons are less likely to be absorbed.

The result of many such atom-photon interactions is that an individual atom, no matter which way it's moving at any given time, will absorb more photons from the direction where the momentum transfer slows them down, and fewer from the direction where the momentum transfer speeds them up. In short, each individual atom is *greatly* slowed down. At the macroscopic level, this translates to a decrease in the *temperature* of the atom cloud. Such a setup is sometimes referred to as a (one-dimensional) “optical molasses” due to the viscous drag force induced on atomic motion, and it is straightforward to extend this model to three dimensions.

Although this setup will decrease atomic velocity, it does not create a confining force, so (eg, in three dimensions) the atoms are still free to move out of the lasers' path, albeit at a decreased speed.

### 2.1.3 Atom Trapping with a MOT

A Magneto-optical trap (MOT) combines the slowing features of an optical molasses (Sec. 2.1.2) with the Zeeman splitting (Sec. 2.1.1) arising from a quadrupolar magnetic field, to produce a robust and isotope-specific trapping force in all three dimensions. The quadrupolar magnetic field is typically generated using a Helmholtz coil surrounding the space in which the trap is formed. The quadrupole shape of the

field implies that it must be zero at some central point between the two coils, and in the space nearby, the magnitude of the magnetic field increases linearly in every direction as one moves away from the centre.

The retroreflecting lasers are red-detuned and circularly polarized in a direction selected to couple to the Zeeman shifted energy level which will push a given atom towards the centre. This provides a restoring force in all three dimensions to atoms that have moved too far from the centre. See Fig. 2.1.

## 2.2 Optical Pumping

The optical pumping process is described in detail within our collaboration’s Ref. [15]. The primary detail described here is that the optical pumping is disturbed by any component of magnetic field not along the quantization axis. (Ours is the vertical axis, defined by the direction of the optical pumping light, and along which the detectors are placed.) This required sophistication with an AC-MOT described in Section 2.4 below.

## 2.3 An Overview of the Double MOT System and Duty Cycle

The experimental subject matter of this thesis was conducted at TRIUMF using the apparatus of the TRIUMF Neutral Atom Trap (TRINAT) collaboration. The TRINAT laboratory offers an experimental set-up which is uniquely suited to precision tests of Standard Model beta decay physics, by virtue of its ability to produce highly localized samples of cold, isotopically pure atoms within an open detector geometry. Although the discussion in this chapter will focus on the methodologies used to collect one particular dataset, taken over approximately 7 days of beamtime in June 2014, the full apparatus and the techniques used are fairly versatile, and can be (and have been) applied to several related experiments using other isotopes.

The TRINAT lab accepts radioactive ions delivered by the ISAC beamline at TRIUMF. These ions are collected on the surface of a hot zirconium foil where they are electrically neutralized, and subsequently escape from the foil into the first of two experimental chambers (the “collection chamber”). Further details on the neutral-

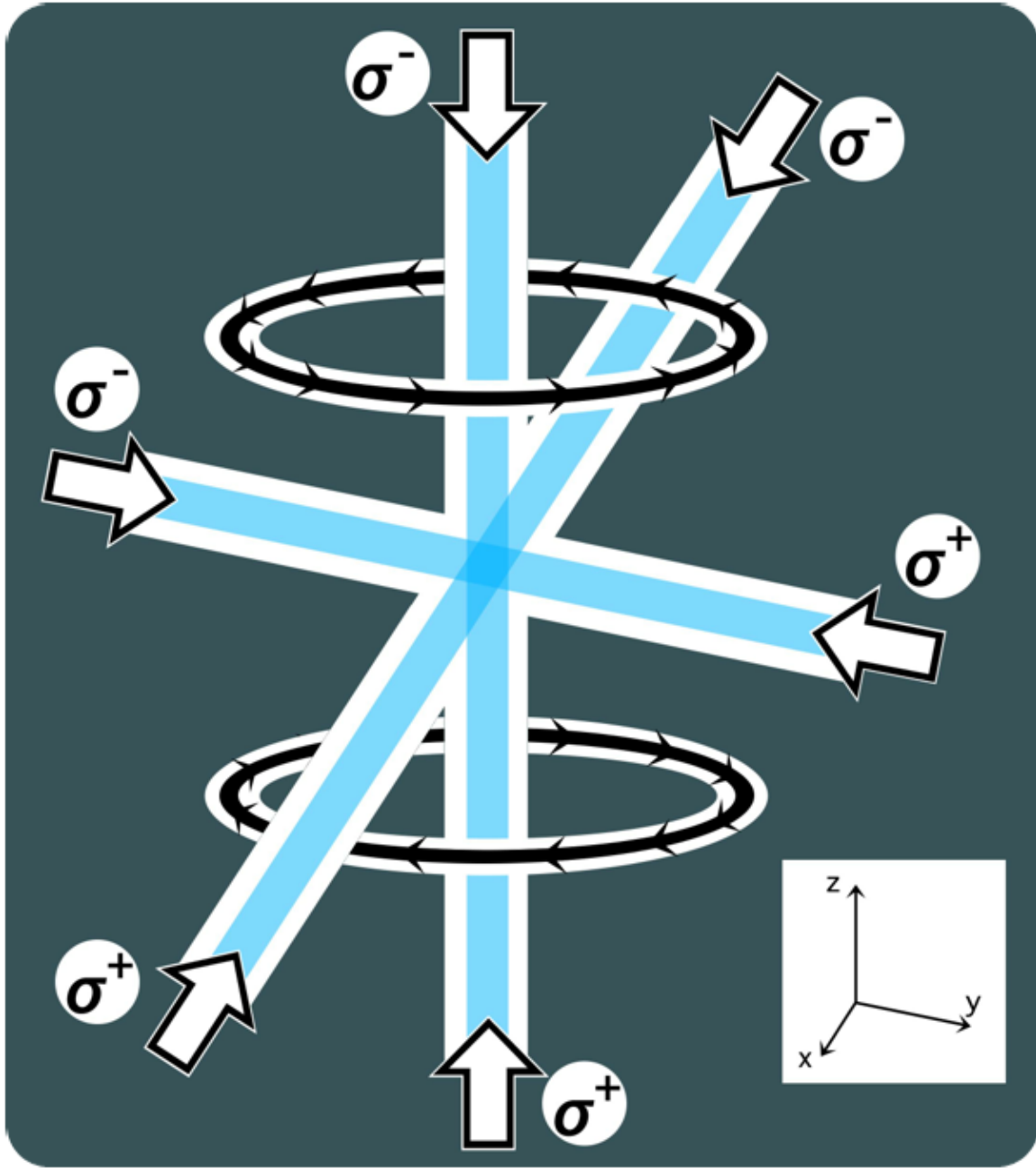


Figure 2.1: Components of a magneto-optical trap, including current-carrying magnetic field coils and counterpropagating circularly polarized laser beams. Diagram taken from [14]

ization process are presented in a previous publication [16]. Within the collection chamber, atoms of one specific isotope – for the purposes of this thesis,  $^{37}\text{K}$  – are

## TRINAT DOUBLE MOT TRAPPING SYSTEM

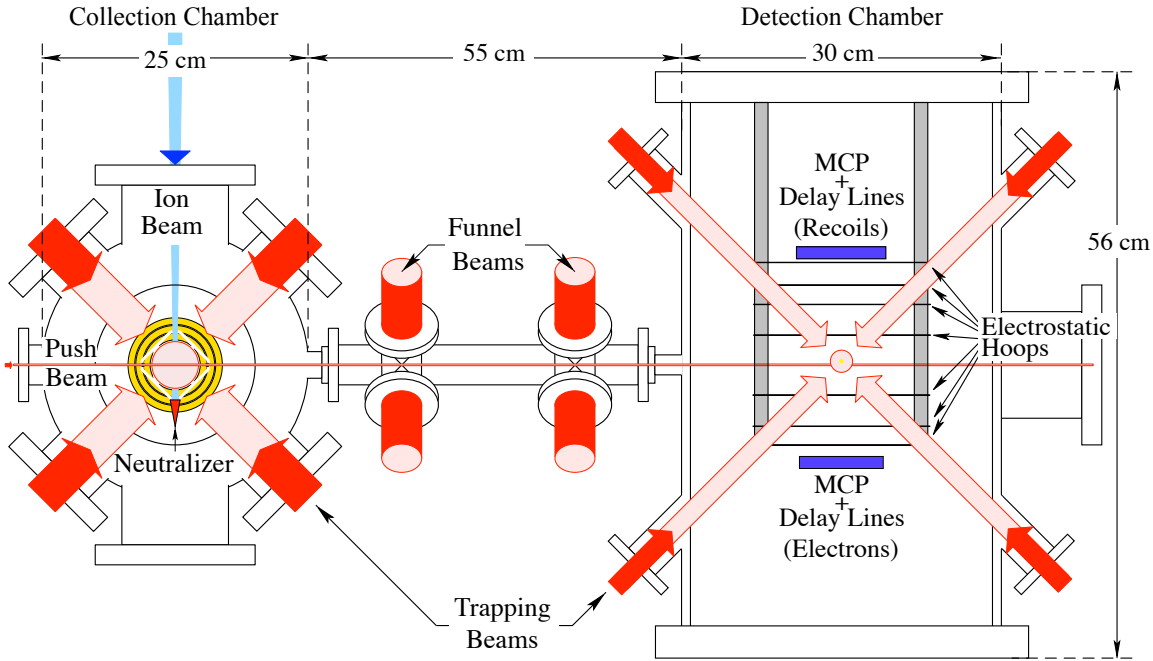


Figure 2.2: The TRINAT experimental set-up, viewed from above. The two MOT system reduces background in the detection chamber. Funnel beams along the atom transfer path keep the atoms focused.

continuously collected into a magneto-optical trap from the tail end of the thermal distribution. Although this procedure preferentially traps only the slowest atoms, once trapped, atoms will be cooled further as a side-effect of the MOT's trapping mechanism. The result is a small ( $\sim 1$  mm diameter), cold ( $\sim 1$  mK) cloud of atoms of a particular isotope.

These properties of the atomic cloud allow for a relatively clean transfer of linear momentum from an appropriately tuned laser beam to the atoms within the cloud, and we use this mechanism to “push” the atoms out of the collection MOT and into the “detection chamber”, where they are loaded into a second MOT (see Fig. 2.2). During regular operation, atoms are transferred approximately once per second.

There is no need to release previously trapped atoms in the second MOT when a new group of atoms is loaded. Although the trap loses atoms over time as a result of a variety of physical processes, during typical operation the majority of atoms loaded in a given transfer will still be trapped at the time the next set of atoms is loaded, and after several transfer cycles, something like a steady state is obtained.

Because the transfer and trapping mechanisms rely on tuning laser frequencies to specific atomic resonances, these mechanisms act on only a single isotope, and all others remain unaffected. The result is a significant reduction of background contaminants within the detection chamber relative to initial beamline output. The transfer methodology is discussed in some detail within another publication [17].

We now turn our attention to what happens to the atom cloud in the detection chamber between loading phases (see Fig. 2.3). One of the goals for the 2014  $^{37}\text{K}$  beamtime required that the atom cloud must be spin-polarized, as well as being cold and spatially confined. Although the MOT makes it straightforward to produce a cold and well confined cloud of atoms, it is fundamentally incompatible with techniques to polarize these atoms. The physical reasons behind this are discussed in Section 2.4.

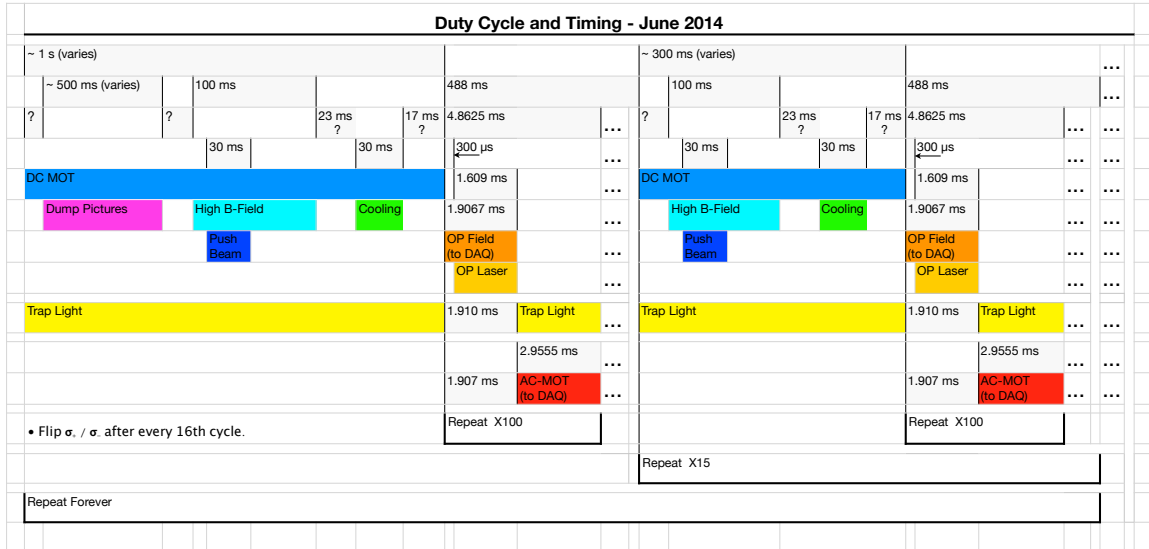


Figure 2.3: The duty cycle used for transferring, cooling, trapping, and optically pumping  $^{37}\text{K}$  during the June 2014 experiment. Not drawn to scale. Question marks indicate timings that varied either as a result of electronic jitter or as a result of variable times to execute the control code. Atoms are transferred during operation of the DC-MOT. Though the push beam laser itself is only on for 30 ms, the bulk of the DC-MOT's operation time afterwards is needed to collect and cool the transferred atoms. After 100 on/off cycles of optical pumping and the AC-MOT, the DC-MOT resumes and the next group of atoms is transferred in. After 16 atom transfers, the polarization of the optical pumping laser is flipped to spin-polarize the atoms in the opposite direction, in order to minimize systematic errors.

Once the newly transferred set of  $^{37}\text{K}$  atoms has been collected into the cloud, the

entire MOT apparatus cycles 100 times between a state where it is ‘on’ and actively confining atoms, and a state where it is ‘off’ and instead the atoms are spin-polarized by optical pumping while the atom cloud expands ballistically before being re-trapped. These 100 on/off cycles take a combined total of 488 ms. The laser components of the trap are straightforward to cycle on and off on these timescales, but the magnetic field is much more challenging to cycle in this manner.

Immediately following each set of 100 optical pumping cycles, another set of atoms is transferred in from the collection chamber to the detection chamber, joining the atoms that remain in the trap (see Fig. 2.3). The details of the trapping and optical pumping cycles are described further in Section 2.4, and the optical pumping technique and its results for this beamtime are the subject of a recent publication [15].

## 2.4 The AC-MOT and Polarization Setup

The AC-MOT was first described by Harvey and Murray [18], but the TRINAT collaboration has adopted its use because it enables the polarization-destroying magnetic field to be eliminated quickly after the MOT is shut off. [14]. A diagram of showing the operation phases of several key components in our AC-MOT/optical pumping duty cycle is shown in Fig. 2.4.

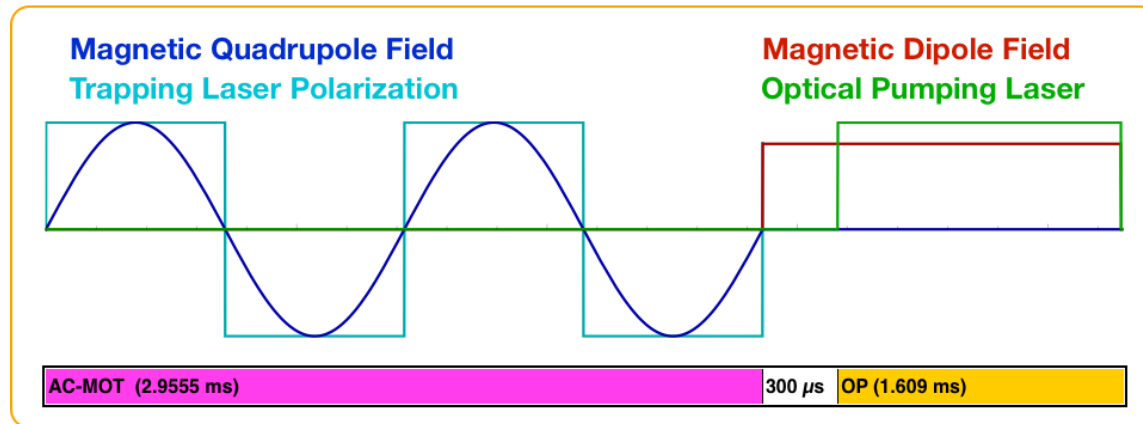


Figure 2.4: One cycle of trapping with the AC-MOT, followed by optical pumping to spin-polarize the atoms. After atoms are transferred into the science chamber, this cycle is repeated 100 times before the next transfer. The magnetic dipole field is created by running parallel (rather than anti-parallel as is needed for the MOT) currents through the two coils.

A standard DC-MOT operates continuously, and in the presence of electrically conductive materials especially, the magnetic field can take a (comparatively) long time to dissipate. This is problematic for an experiment such as this one, because the atoms do not remain confined while the magnetic field dissipates due to potential anomalies in the magnetic field shape arising from induced eddy currents, and for similar reasons, they cannot be successfully optically pumped during this time period either. Therefore, it is important to waste as little time as possible switching between the MOT and the optical pumping phases in the duty cycle. For optical pumping, a weak, dipole-shaped magnetic field is preferred, and this is not possible while the quadrupole field has not dissipated.

The principle behind the AC-MOT is to simply run a sinusoidal current through one's anti-Helmholtz coils while flipping the laser polarization to remain in sync.

As alluded to in the previous section (2.3), the measurements in question required a spin-polarized sample of atoms, and a precise knowledge of what that polarization was. This is needed in order to make best use of the superratio asymmetry for both  $A_\beta$  and  $b_{\text{Fierz}}$  measurements. [19][15].

A MOT requires a quadrupolar magnetic field, and we generate ours with two current-carrying anti-Helmholtz coils located within the vacuum chamber itself. Since these coils are expected to run an alternating current, heat is produced and cannot be dissipated in the vacuum. Therefore the coils themselves are hollow copper tubes, and they are continuously cooled by pumping temperature-controlled water through them.

We spin-polarize  $^{37}\text{K}$  atoms within the trapping region by optical pumping [15]. A circularly polarized laser is tuned to match the relevant atomic resonances, and is directed through the trapping region along the vertical axis in both directions. When a photon is absorbed by an atom, the atom transitions to an excited state and its total angular momentum (electron spin + orbital + nuclear spin) along the vertical axis is incremented by one unit. When the atom is de-excited a photon is emitted isotropically, so it follows that if there are available states of higher and lower angular momentum, the *average* change in the angular momentum projection is zero. If the atom is not yet spin-polarized, it can absorb and re-emit another photon, following a biased random walk towards complete polarization.

In order to optimally polarize a sample of atoms by this method, it is necessary to have precise control over the magnetic field. This is because absent other forces, a

spin will undergo Larmor precession about the magnetic field lines. In particular, the magnetic field must be aligned along the polarization axis (otherwise the tendency will be to actually depolarize the atoms), and it must be uniform in magnitude over the region of interest (otherwise its divergencelessness will result in the field also having a non-uniform direction, which results in a spatially-dependent depolarization mechanism). Note that this type of magnetic field is not compatible with the MOT, which requires a linear magnetic field gradient in all directions (characteristic of a quadrupolar field shape), and has necessitated our use of the AC-MOT.

## 2.5 Measurement Geometry and Detectors

The TRINAT detection chamber operates at ultra-high vacuum (UHV) and provides not only the apparatus necessary to intermittently confine and then spin-polarize atoms, but also the variety of detectors and implements required to quantify their position, temperature, and polarization. The detection chamber further boasts an array of electrostatic hoops to collect both positively and negatively charged low energy particles into two opposing microchannel plate (MCP) detectors, each backed by a set of delay lines to measure hit position, and a further set of two beta detectors positioned across from each other along the polarization axis, each of which consists of a 40x40 pixel double-sided silicon strip detector (DSSD) and a scintillator coupled to a photomultiplier tube (PMT) (see Fig. 2.5). The chamber also includes 6 viewports specifically designed to be used for the trapping and optical pumping lasers (see Fig. 2.6.).

### 2.5.1 Microchannel Plates and Electrostatic Hoops

Two stacks of microchannel plates (MCPs) have been placed on opposing sides of the chamber, and perpendicular to the axis of polarization. Each stack of MCPs is a relatively large detector backed by a series of delay lines for position sensitivity. These two MCP detectors are designed to operate in conjunction with a series of seven electrostatic ‘hoops’ positioned within the chamber and connected to a series of high voltage power supplies. The hoops are designed in such a way as to maintain a constant and (roughly) uniform electric field across the space between the two MCP detectors, without blocking either the path of particles originating from the central

cloud, or necessary laser beams. The resulting electric field acts to pull positively charged ions towards one MCP detector and negatively charged electrons towards the other (see Figs. 2.5 and 2.6).

The detector intended to collect the negatively charged electrons (the “eMCP”) has an active area of 75.0 mm, and is positioned 100.0 mm from the chamber centre. It features a Z-stack configuration of three plates, and it is backed by a set of three separate delay lines in a “hexagonal” arrangement for redundant position sensitivity (the “HEX75”). The detector used to collect positively charged ions (the “iMCP,” or equivalently the “rMCP” since many of the ions collected are recoils from decay) is 80.0 mm in diameter and positioned 101.4 mm from the chamber centre. It features only two plates arranged in a chevron configuration, and it is backed by a set of two separate delay lines (the “DLD80”) for position sensitivity. In the context of the present work, the rMCP data is used primarily in conjunction with the photoionization laser to characterize the atom cloud (Section 2.5.3), while the eMCP data is used, together with the beta detectors, as a ‘tag’ for decay events originating from the cloud.

Due to an unfortunate interaction between the two MCP detectors, during the 2014 beamtime it was not possible to run both the eMCP and the rMCP simultaneously without producing a large background on at least one detector (there seemed to be no consistency as to which detector was most affected at a given time). As a result, data was instead collected with only one MCP detector biased at a time, and the active detector was alternated every few hours to spend approximately equal time collecting data with the eMCP and rMCP. Online scientific data has been collected with the eMCP at electric field strengths of 66.7 V/cm and 150. V/cm, while rMCP data has been collected at 395. V/cm, 415. V/cm, and 535. V/cm. Note that these field strengths are all too low to significantly perturb any but the least energetic of the (positively charged) betas originating from decay, and those betas already lack the energy that would be needed to travel through the SiC mirror and Be foil vacuum seal into a beta detector.

### 2.5.2 Beta Detectors

The beta detectors, located above and below the atom cloud along the axis of polarization (Fig. 2.5), are each the combination of a plastic scintillator and a set of

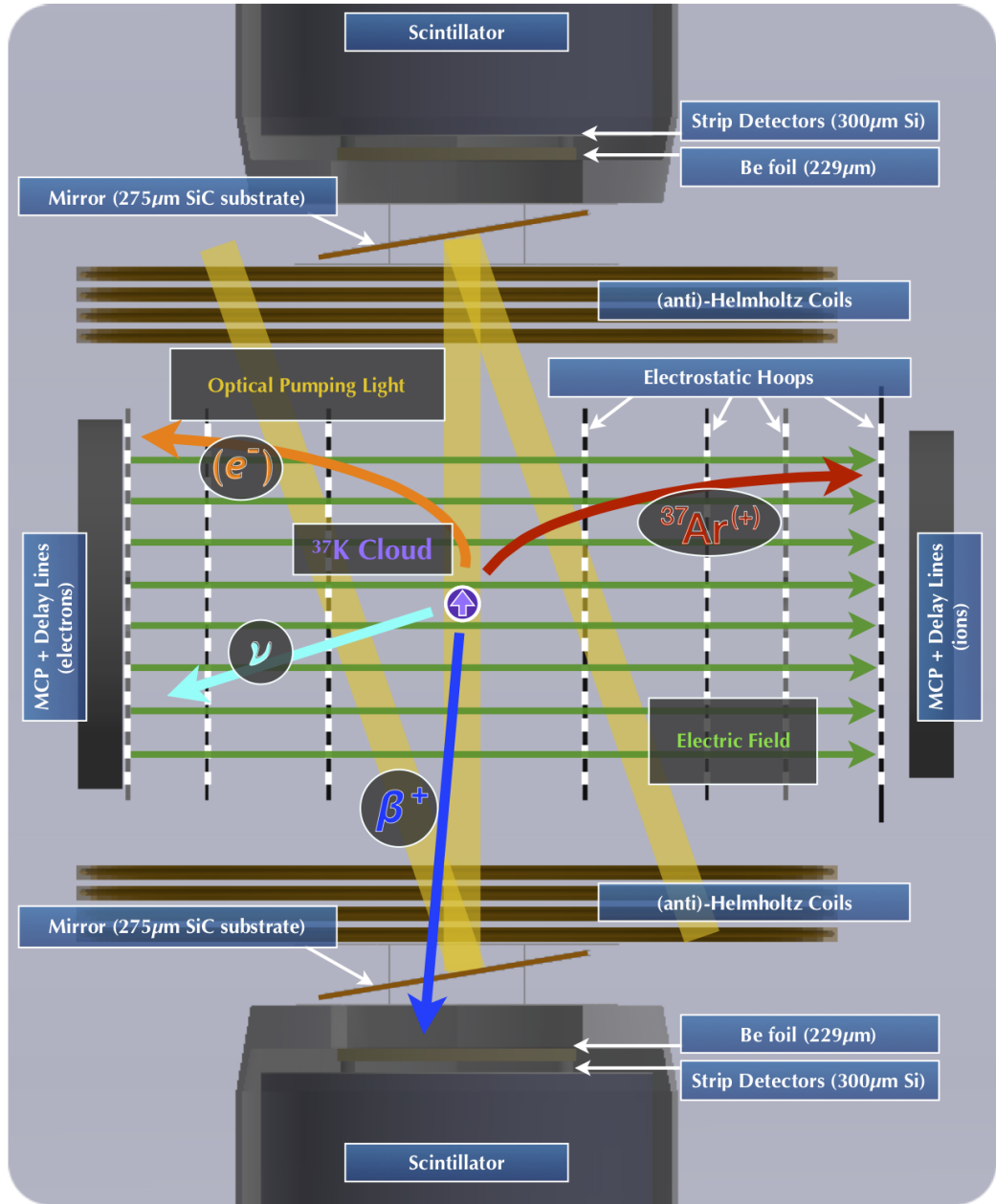


Figure 2.5: A scale diagram of the interior of the TRINAT detection chamber, shown edge-on with a decay event. After a decay, the daughter will be unaffected by forces from the MOT. Positively charged recoils and negatively charged shake-off electrons are pulled towards detectors in opposite directions. Although the  $\beta^+$  is charged, it is also highly relativistic and escapes the electric field with minimal perturbation.

silicon strip detectors. Using all of the available information, these detectors are able to reconstruct the energy of an incident beta, as well as its hit position, and provide a

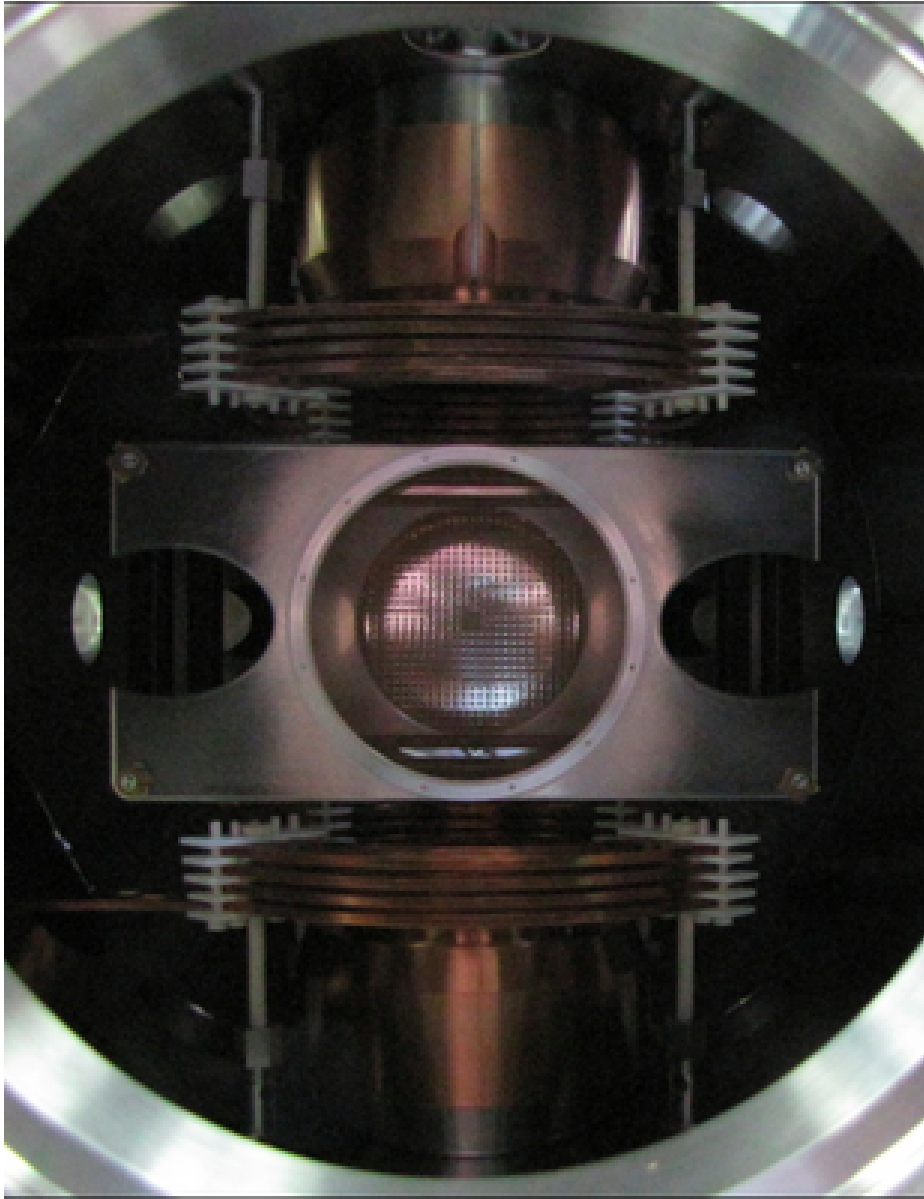


Figure 2.6: Inside the TRINAT detection chamber. This photo is taken from the vantage point of one of the microchannel plates, looking into the chamber towards the second microchannel plate. The current-carrying copper Helmholtz coils and two beta telescopes are visible at the top and bottom. The metallic piece in the foreground is one of the electrostatic hoops used to generate an electric field within the chamber. The hoop's central circular hole allows access to the microchannel plate, and the two elongated holes on the sides allow the MOT's trapping lasers to pass unimpeded at an angle of 45 degrees 'out of the page'.

timestamp for the hit’s arrival. Together the upper and lower beta detectors subtend approximately 1.4% of the total solid angle as measured with respect to the cloud position.

The two sets of beta detectors were positioned directly along the axis of polarization. Each beta detector consists of a plastic scintillator and photo-multiplier tube (PMT) placed directly behind a  $40 \times 40$ -pixel double-sided silicon strip detector (DSSD). The scintillator is used to measure the overall energy of the incoming particles, as well as to assign a timestamp to these events, while the DSSD is used both to localize the hit position to one (or in some cases, two) individual pixel(s), and also to discriminate between different types of incoming particles. In particular, though the scintillator will measure the energy of an incoming beta or an incoming gamma with similar efficiency, the beta will lose a portion of its kinetic energy as it passes through the DSSD into the scintillator. By contrast, an incident gamma will deposit only a very small amount of energy in the DSSD layer, making it possible to reject events with insufficient energy deposited in the DSSD as likely gamma ray events. Given that the decay of interest to us emits positrons, we expect a persistent background 511 keV gamma rays that are not of interest to us, so it is extremely important that we are able to clean these background events from our spectrum.

It must be noted that the path between the cloud of trapped atoms and either beta detector is blocked by two objects: a  $275\text{ }\mu\text{m}$  silicon carbide mirror (necessary for both trapping and optical pumping), and a  $229\text{ }\mu\text{m}$  beryllium foil (separating the UHV vacuum within the chamber from the outside world). In order to minimize beta scattering and energy attenuation, these objects have had their materials selected to use the lightest nuclei with the desired material properties, and have been manufactured to be as thin as possible without compromising the experiment. As the  ${}^{37}\text{K} \rightarrow {}^{37}\text{Ar} + \beta^+ + \nu_e$  decay process releases  $Q = 5.125\text{ MeV}$  of kinetic energy [20], the great majority of betas are energetic enough to punch through both obstacles without significant energy loss before being collected by the beta detectors.

### 2.5.3 The Photoionization Laser

In order to measure properties of the trapped  ${}^{37}\text{K}$  cloud, a 10 kHz pulsed laser at 355 nm is directed towards the cloud. These photons have sufficient energy to photoionize neutral  ${}^{37}\text{K}$  from its excited atomic state, which is populated by the

trapping laser when the MOT is active, releasing 0.77 eV of kinetic energy, but do not interact with ground state  $^{37}\text{K}$  atoms. The laser is of sufficiently low intensity that only  $\sim 1\%$  of excited state atoms are photoionized, so the technique is only very minimally destructive.

Because an electric field has been applied within this region (Section 2.5.1) the  $^{37}\text{K}^+$  ions are immediately pulled into the detector on one side of the chamber, while the freed  $e^-$  is pulled towards the detector on the opposite side of the chamber. Because  $^{37}\text{K}^+$  is quite heavy relative to its initial energy, it can be treated as moving in a straight line directly to the detector, where its hit position on the microchannel plate is taken as a 2D projection of its position within the cloud. Similarly, given a sufficient understanding of the electric field, the time difference between the laser pulse and the microchannel plate hit allows for a calculation of the ion's initial position along the third axis.

With this procedure, it is possible to produce a precise map of the cloud's position and size, both of which are necessary for the precision measurements of angular correlation parameters that are of interest to us here. However, it also allows us to extract a third measurement: the cloud's polarization.

The key to the polarization measurement is that only atoms in the excited atomic state can be photoionized via the 355 nm laser. While the MOT runs, atoms are constantly being pushed around and excited by the trapping lasers, so this period of time provides a lot of information for characterizing the trap size and position. When the MOT is shut off, the atoms quickly return to their ground states and are no longer photoionized until the optical pumping laser is turned on. As described in Section 2.2, and in greater detail in [15], the optical pumping process involves repeatedly exciting atoms from their ground states until the atoms finally cannot absorb any further angular momentum and remain in their fully-polarized (ground) state until they are perturbed. Therefore, there is a sharp spike in excited-state atoms (and therefore photoions) when the optical pumping begins, and none if the cloud has been fully polarized. The number of photoion events that occur once the sample has been maximally polarized, in comparison with the size and shape of the initial spike of photoions, provides a very precise characterization of the cloud's final polarization [15].

# Chapter 3

## Calibrations and Data Selection

In a precision measurement, the bulk of the research is in determining the systematic uncertainties through self-consistent analysis and simulation. Each detector in this experiment is critical and has independent calibrations and cuts, which are described in detail in this chapter. Because this analysis was not blinded, there is an increased importance that the choice of cuts should be clearly justified. The main goal of blinding was nevertheless achieved — to make sure all analysis is done completely with full redundancy of checks wherever possible — so the discipline entailed must be described in full detail.

### 3.1 An Overview of Available Data

Although the detection chamber was designed to feature two MCP detectors on opposing sides of an applied electric field intended for simultaneous use (see Section 2.5.1), in practice the two detectors produced quite a bit of feedback when operated at the same time. In order to salvage usable data from the beamtime, it was necessary to run only one detector at a time, but switched which detector was in use every few hours, collecting approximately the same amount of data with each detector (see Tables 3.1 and 3.2). Thus, the runs are sorted into ‘electron’ and ‘recoil’ runs, depending on what the detector in use was intended to detect. The data is further split up into several runsets based on when certain settings were adjusted, and the individual runsets have been treated separately for nearly all parts of the analysis.

While the beta asymmetry and Fierz interference are best evaluated using the

## Electron Runs

---

	OP Delay	Events	Electric Field	Runs
Runset EA	$300\ \mu s$	0	66.67 V/cm	314, 362, 363, 383-386, 393.
Runset EB	$300\ \mu s$	173,640	150.0 V/cm	428-437, 440-445.
Runset EC	$700\ \mu s$	18,129	150.0 V/cm	476, 477.
Runset ED	$400\ \mu s$	207,596	150.0 V/cm	478-489, 502-505, 510, 513.

Table 3.1: A list of 2014 online electron runs with potentially usable data. The “Events” column includes only the number of events that passed all cuts.

## Recoil Runs

---

	OP Delay	Electric Field	Runs
Runset RA	$300\ \mu s$	395.0 V/cm	303, 308-313, 318, 326, 327, 328, 340, 342, 343, 376, 377, 378, 394, 395, 396, 398-402.
Runset RB	$300\ \mu s$	535.0 V/cm	409-419, 421-426, 446, 447, 449.
Runset RC	$700\ \mu s$	395.0 V/cm	450, 454, 455.
Runset RD	$700\ \mu s$	415.0 V/cm	460-466, 473, 474.
Runset RE	$400\ \mu s$	415.0 V/cm	491, 497, 498, 499, 509.

Table 3.2: A list of 2014 online recoil runs and associated parameters. A count of good events that pass all cuts is not included because different cuts must be used for polarization and trap position data.

electron runs, the polarization (a dominant uncertainty in the beta asymmetry measurement) and cloud position are best evaluated with recoil runs. The polarization measurement is the subject of a recent publication (see [15]), and the evaluation of cloud position is discussed in Section 3.4. The recoil runs may also be analyzed in the future as part of a search for right-handed Weak interactions (described further in Chapter 6.2).

In considering Tables 3.1 and 3.2, we note that Runsets EA and RA were neglected completely during analysis after it was determined that one scintillator had an improperly set hardware threshold such that lower energy betas weren’t being detected at all. Additionally, there was a QDC module failure before Run 450, resulting in an abrupt change in calibration for the two scintillators. The electric field is larger during recoil runs in an attempt to maximize the fraction of nuclear recoils collected,

as well as the separation in TOF between different charge states. For electron runs, although not all SOEs were collected, the lower electric fields were preferred in order to decrease background events and the sparking incidents. Although the final analysis uses only the eMCP runs directly, the result could not have been obtained with the same degree of precision had the rMCP data not been present.

## 3.2 Preliminary Data Selection with the rMCP

As described in Chapter 2.5.3, the primary function of the rMCP within the context of this experiment is as a probe of the atom cloud, and it provided a critical check of the cloud’s position, size, and polarization state over the course of the beamtime. The process of cleaning, calibrating, and analyzing this data is described here.

The two delay lines located just behind the rMCP provide information about hit position. The principle behind a delay line’s operation is relatively straightforward. The delay line itself is made from a thin wire wound into a flattened coil that covers the area of the microchannel plate. The second delay line is oriented perpendicular to the first and immediately behind it, but also covers the full area of the microchannel plate. When a charged particle is incident on the stack of microchannel plates, an electron shower is initiated. The shower gains strength as it propagates through the MCPs’ microchannels, and emerges on the back side of the stack after having been greatly amplified.

After emerging from the back of the MCP stack, the electron shower is then incident on a delay line, generating an electrical pulse that propagates from the hit point towards both ends of the wire. Although the wire is conductive, the propagation speed is finite, and this fact is key to extracting the hit position. The time of arrival for the electrical pulse is recorded at each end of the delay line wire, and it is the difference between the two times that tells where along the wire the original hit occurred. In general, a single delay line is only precise enough to determine the hit position as projected along the direction perpendicular to its coil’s wires. The electron shower continues past the first delay line to hit the delay line immediately behind, which again creates an electrical pulse that propagates towards the ends of that wire, and a similar procedure can be used to evaluate the hit position in the perpendicular direction. Therefore, for an event in which the rMCP is hit and an

electron shower is triggered, we expect to have five timestamps associated with that hit – one associated with the MCP stack itself, and two from each delay line.

This understanding of how delay lines work informs the initial stages of data processing for rMCP events. To obtain the cleanest possible rMCP data, the first step is to simply throw out every event which doesn't have a complete set of five timestamps associated with it – even though it would still be possible to make good use of many events which have only partial data. Even though many “real” rMCP hit events came in under threshold in one or more channels, detector noise was plentiful, and that noise varied in both quality and quantity over the course of the beamtime. Therefore, it was decided to be more important for the rMCP data to be as clean as possible, despite the fact that its statistical power would be reduced. (Note that this step is *not* done on the eMCP side – more on that in Section 3.8)

The next stage of rMCP data cleaning is to discard events with an aberrant set of timestamps. A delay line is essentially just a long wire, and the time it takes to propagate a signal from one end of the wire to the other is fixed. This means that no matter where along the delay line a pulse is generated, if one adds rather than subtracts the timestamps at which the pulse arrives at each of the two ends, that sum should be constant after accounting for the time of the original hit – which we can determine from the timestamp associated with the MCP. To that end, we construct delay line sums for the “x” and “z” delay lines,

$$\text{DLA\_XSUM} = (\text{TDC\_DL\_X1}) + (\text{TDC\_DL\_X2}) - 2(\text{TDC\_ION\_MCP}) \quad (3.1)$$

$$\text{DLA\_ZSUM} = (\text{TDC\_DL\_Z1}) + (\text{TDC\_DL\_Z2}) - 2(\text{TDC\_ION\_MCP}). \quad (3.2)$$

For a perfectly operating detector, one would expect for a collection of many measurements of DLA\_XSUM and DLA\_ZSUM should each look like an isolated delta spike. In practice however, our distributions had a more complex set of features. The shapes, widths, and even positions of these distributions changed from run to run, and not all of these changes could be attributed to a known cause (e.g. a change in detector settings). Distributions from a single run are shown in Fig. 3.1.

Because the characteristics of these timing sum distributions varied from run to run, it didn't make sense to aggregate all the data before taking cuts, so any cuts had to be chosen on a run-by-run basis. Because of the asymmetry and occasional bimodality of the distributions, it also didn't make sense to try to fit the distributions to a function such as a gaussian and then cut away some number of sigma from the

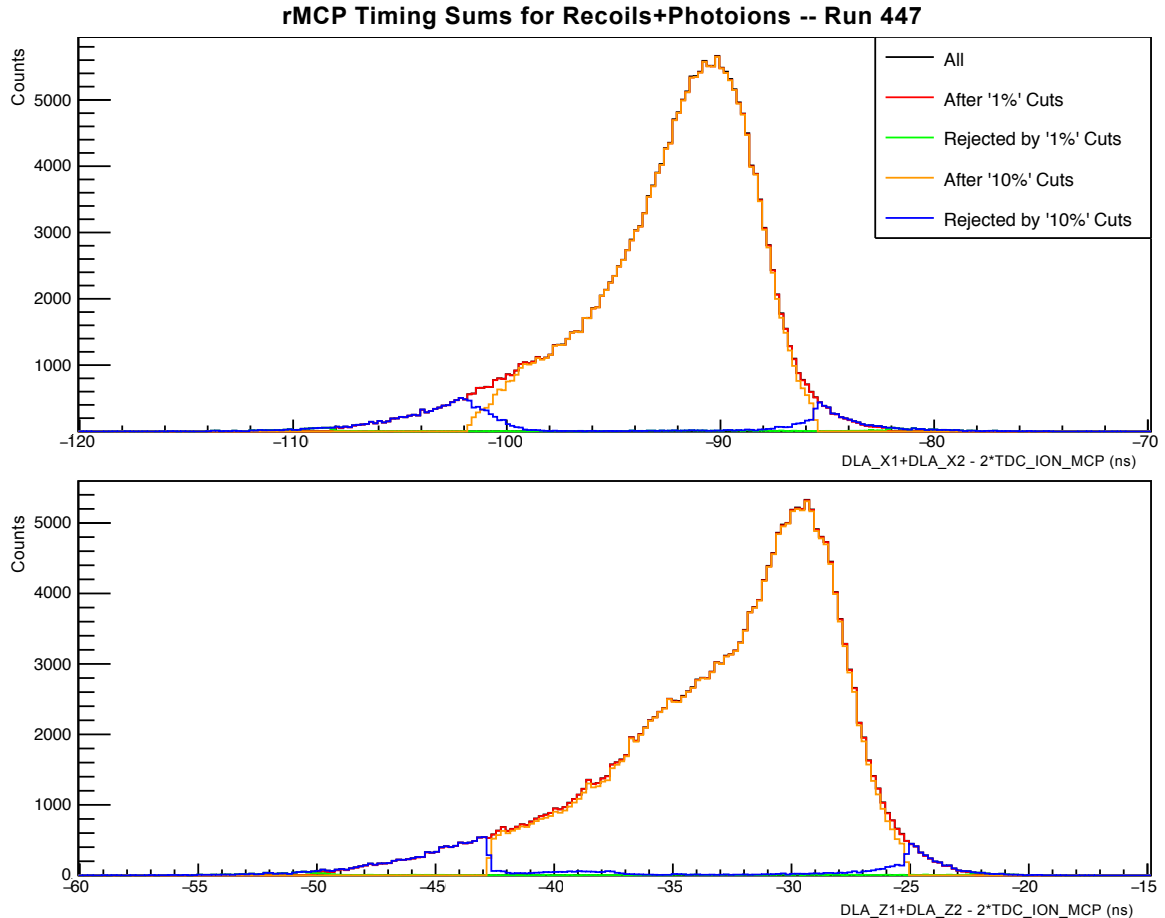


Figure 3.1: Timing sums and associated cuts for the rMCP detector, run 447. The ‘10%’ cuts shown simply eliminate events in which the distribution’s height at that value is less than ‘10%’ of that distribution’s maximum, and the ‘1%’ cuts are performed in a similar manner. Note that this is *not* the equivalent of eliminating 10% (1%) of events. The above distributions each show the results within their own distribution after cuts are taken on the *other* distribution. Only a single run is shown here to avoid washing out features – because the characteristics of these spectra varied significantly over the course of the beamtime, and not all of the changes can be attributed to a change in settings.

fit function. The algorithm that was used in the end was to determine the peak’s maximum, then discard events from the portion of the distribution in which the distribution’s height is less than 10% of the maximum. Fig. 3.2 shows the effect of these cuts on the measured cloud position within a single run.

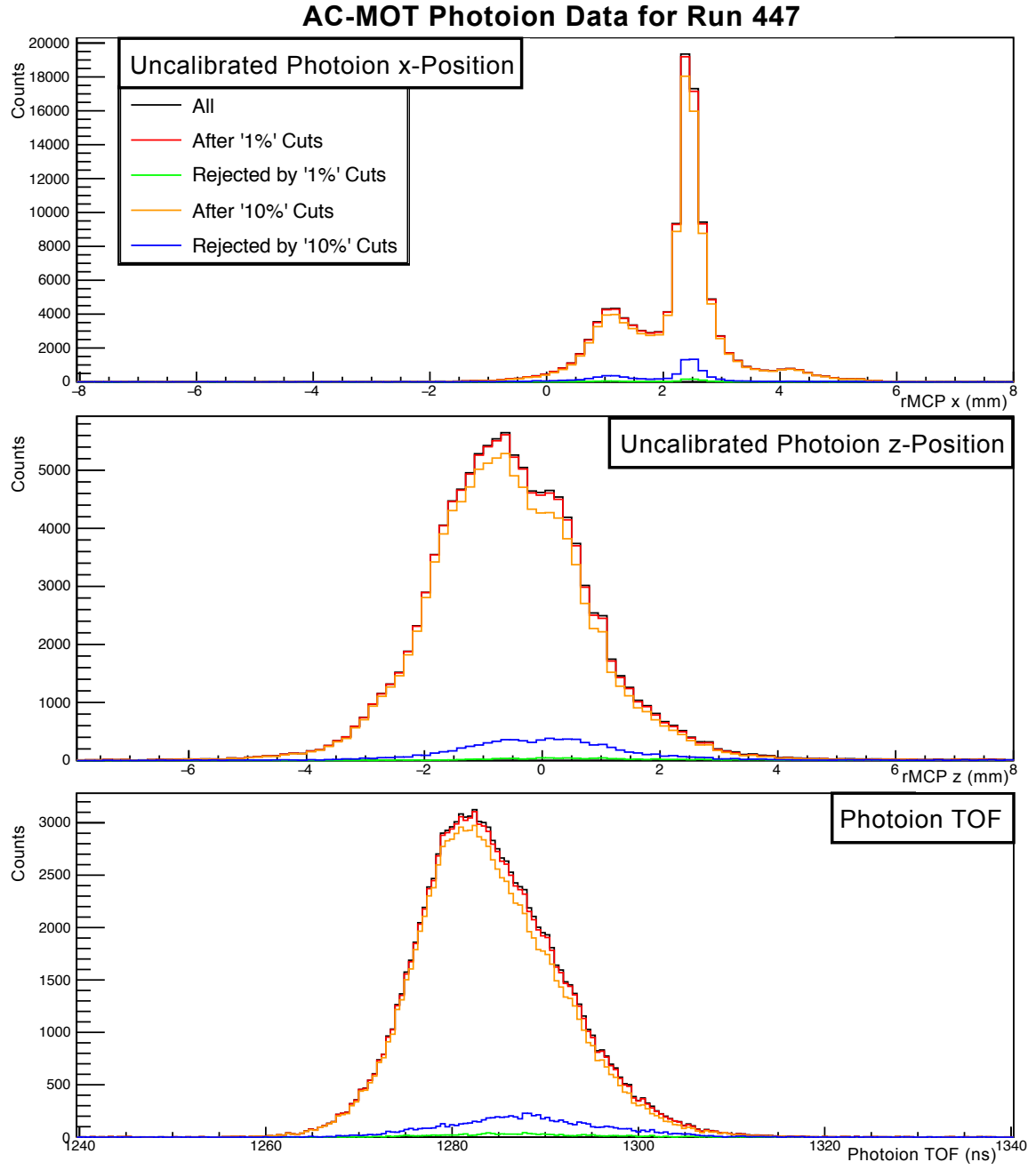


Figure 3.2: Cloud Position for run 447 for rMCP timing sum cuts as shown in Fig. 3.1.

### 3.3 Calibrations with the rMCP

A calibration mask was created for the rMCP, to eliminate any nonlinearities in the images produced. Several months before the  $^{37}\text{K}$  beamtime was to occur, the

mask was attached in front of the rMCP, and a test of the delay lines' ability to produce an image was performed using an alpha source to illuminate the full surface of the detector. The mask was later removed in advance of the beamtime, in order to preserve the highest possible surface area, and calibrations were performed using the older mask data and subsequently applied to the online  $^{37}\text{K}$  data.

The calibration to the offline data with a visible mask was performed over a number of steps. The data was given a preliminary rough calibration, performed on each delay line separately, which simply involved taking the difference in pulse arrival times between each end of the delay line, scaling the result by a factor chosen to get the image to be the approximate correct size, and then subtracting an offset to center the image.

With the preliminary calibration providing a visible image to work with, the '10%' cuts as described in Section 3.2 were applied, significantly sharpening the visual mask lines and overall image border. Next, a small rotation was applied, followed by a more precise centering algorithm. Following this, a linear stretching algorithm was applied to adjust the height and width of each row and column individually, while aligning the grid lines to their known position on the detector. Finally, an additional radial stretch was applied to only the outer areas of the image. This last adjustment can be justified by noting that it's expected for the outer parts of the detector to produce a more distorted image, and that appeared to be the case here. See Fig. 3.3.

When the online rMCP data was eventually collected, it was found that the rMCP image appeared offset by several centimeters relative to the previous calibration, which necessarily affected the location of the timing sum peaks (similar to those shown in Fig. 3.1). The most likely cause for this is a change in cable lengths between the readout and data acquisition in the months between the calibration and online data collection, but it meant a new set of '10%' cuts needed to be established for the online data, and also cast some doubt on the validity of the established calibrations. In the end, these cuts were established on a run-by-run basis due to the varying shape of the timing sum peaks.

Our ability to confidently accurately apply the old offline calibration to the new online data depended on our ability to center the image correctly, as different parts of the image are stretched and squeezed differently. The appearance of the plate edge—the only remaining indicator of the quality of the centering or overall calibration—changed shape slightly from run to run. Despite this, images from the online data

were all summed together after applying run-by-run cuts, and the resulting image was centered by eye.

The centering was performed iteratively, because the subsequent steps in the calibration will distort the image differently depending on how accurately it was centered beforehand. These subsequent steps in which the image is stretched and squished will also change the apparent centering of the overall image. Calibrated and uncalibrated images are shown in Fig. 3.3 for both offline and online data.

The lower plots in Fig. 3.3 show an unfortunate pattern of vertical stripes across the full surface of the rMCP. These stripes persisted over many (but not all) of the online runs. They can still be clearly seen in Fig. 3.4, which is a sum of all Runset RB's photoion events. The cause for these stripes could not be determined, and they could not be removed in post-processing analysis.

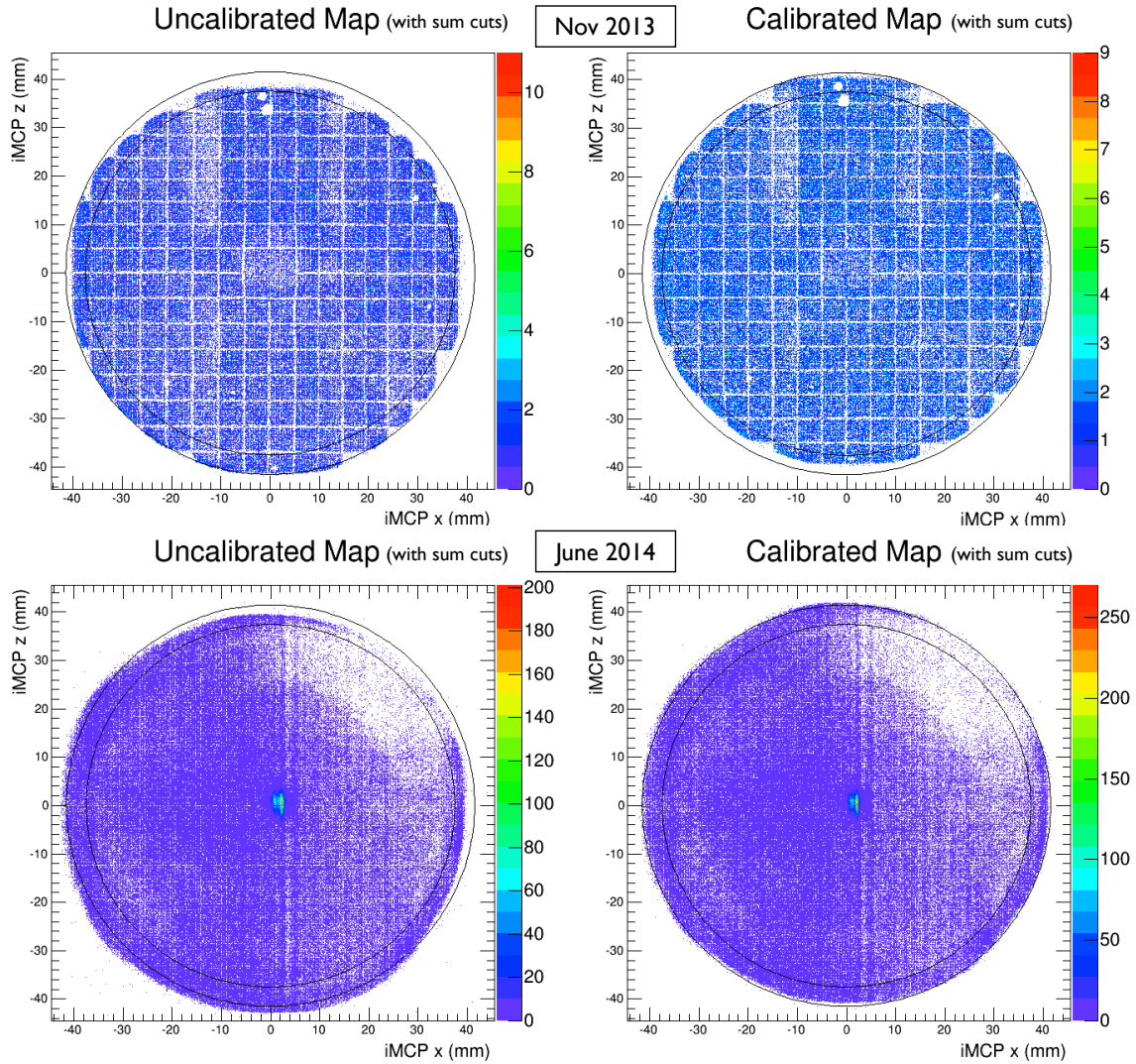


Figure 3.3: rMCP Calibration. The left images show the rMCP hit map with only a basic preliminary calibration; the images on the right are filled with the same hit data, but after the calibration has been performed. The upper two images are from data collected offline in advance of the 2014 beamtime using an alpha source; the shadow from a calibration mask is clearly visible. The lower images show rMCP data taken from a single online run, and includes both photoion and nuclear recoil data, collected over both the polarized and AC-MOT times. The photoion image of the atom cloud visible in the centre of the lower plots.

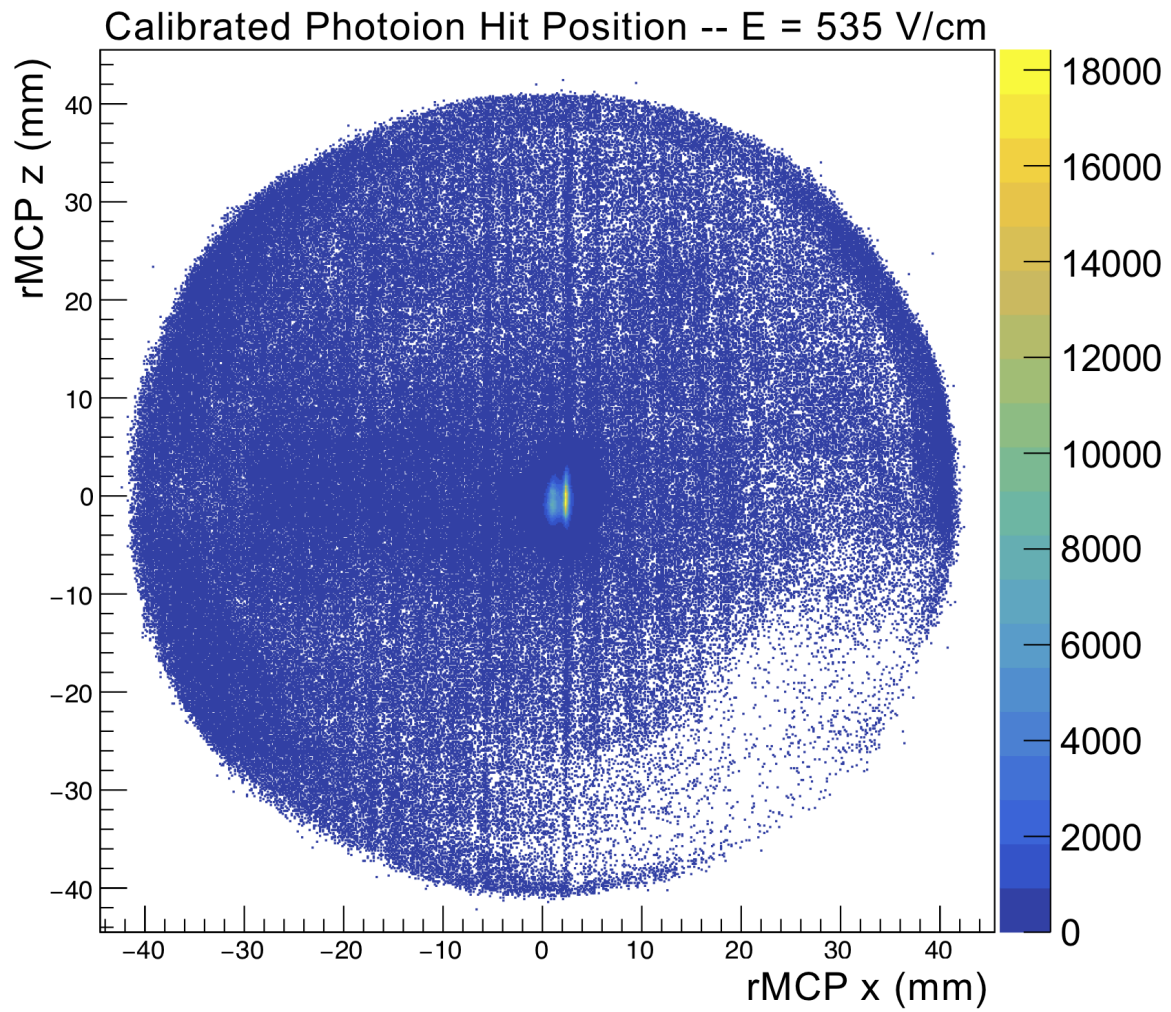


Figure 3.4: Photoion Hit Positions in 2D. This is the entirety of the good photoion data taken at 535 V/cm. The central bright spot is an image of the atom cloud arising from photoionization events of unpolarized atoms; the rest is background. Vertical stripes of indeterminate cause can be seen across the face of the image – it has not been possible to eliminate them in analysis.

### 3.4 Measurements of the Atom Cloud

With the rMCP detector calibrated (Section 3.3), several types of data may be extracted. It is possible to extract the hit positions and times-of-flight for the incident nuclear recoils, and an analysis of such data could be used to perform a test of right-handed currents within the nuclear weak force, as discussed in Chapter 6.2. However, we will focus here on what may be learned about the *atom cloud* from rMCP events in coincidence with the photoionization laser.

This class of data (events with both an rMCP hit and a photoionization laser hit in coincidence) can be used to measure cloud polarization, and the methodology and results of that process as it applies to this particular experiment are discussed in a recent publication [15]. We are also interested in the cloud’s position and size during the periods of time where decay data is collected, since this represents a potential systematic effect that must be accounted for within our models. The latter will be the primary focus of this section.

The first step in such a measurement is to try to eliminate as much background as possible. We have already required that every event considered here must include both an rMCP hit and a photoionization laser pulse. As we are interested in measurements of trap position, it makes sense to also require a *complete* set of position data recorded on the rMCP’s delay lines. This is further trimmed by a ‘10% cut’ on the timing sums, as described in Sec. 3.2. Any event including a scintillator hit is rejected, as these events have an increased likelihood for a recoiling ion to be detected on the rMCP instead of- or in addition to the photoion we expect (It is at this stage of the process that Fig. 3.4 is created.). Finally, some fairly loose cuts are applied about the central x- and z-positions, as well as the ion’s time of flight (measured with respect to the arrival of a photoionization laser pulse).

With these basic cuts performed, the cloud position and size must be measured. We are particularly interested in measurements of the cloud during the time when it is considered to be *polarized* — however the great majority of photoionization events occur when the cloud is *not polarized* (see Fig. 3.5). This is because the photoionization laser acts only on excited atomic states, which are readily available during the operation of the MOT. When the MOT is shut off, the atoms quickly de-excite. At the start of optical pumping 300  $\mu\text{s}$  later (in the case of the 535 V/cm data), there is a short burst of photoions due to the atoms being temporarily placed

into an excited state as part of the optical pumping process. The photoion burst falls away rapidly as atoms are optically pumped into the stretched state and can no longer be excited by the optical pumping laser.

A projection of the cloud's position on the x- and z-axes, and its TOF (indicative of position along the y-axis) is plotted over the course of the repeating AC-MOT/OP cycle in Fig. 3.5. The mysterious vertical stripes seen Fig. 3.4 are clearly evident in the top plot of Fig. 3.5, and their positions do not change over the AC-MOT cycle, even though cloud motion is clearly visible.

To extract the size and position of the atom cloud as projected onto all three axes, time slices of several hundred  $\mu\text{s}$  are taken from the beginning of the AC-MOT cycle, and from the part of the AC-MOT cycle immediately before the MOT is turned off. A gaussian is fitted to the cloud projection, with its parameters describing the trap's size and position during these parts of the cycle. A linear interpolation applied to describe the cloud's 3D size and position during polarized times, as functions of time since the AC-MOT cycle started. Results are shown in Table 3.3.

Runsets		Initial Position	Final Position	Initial Size	Final Size
EB $\leftarrow$ RB	x	1.77 $\pm$ 0.03	2.06 $\pm$ 0.08	0.601 $\pm$ 0.013	1.504 $\pm$ 0.047
	y	-3.51 $\pm$ 0.04	-3.33 $\pm$ 0.05	1.009 $\pm$ 0.013	1.551 $\pm$ 0.018
	z	-0.661 $\pm$ 0.005	-0.551 $\pm$ 0.021	0.891 $\pm$ 0.004	1.707 $\pm$ 0.015
EC $\leftarrow$ RD	x	2.22 $\pm$ 0.05	2.33 $\pm$ 0.11	1.18 $\pm$ 0.04	1.538 $\pm$ 0.087
	y	-3.68 $\pm$ 0.04	-3.31 $\pm$ 0.06	0.965 $\pm$ 0.012	1.460 $\pm$ 0.030
	z	-0.437 $\pm$ 0.09	-0.346 $\pm$ 0.037	0.927 $\pm$ 0.007	1.797 $\pm$ 0.026
ED $\leftarrow$ RE	x	2.274 $\pm$ 0.012	2.46 $\pm$ 0.06	0.386 $\pm$ 0.016	1.382 $\pm$ 0.046
	y	-4.54 $\pm$ 0.04	-4.28 $\pm$ 0.04	0.986 $\pm$ 0.08	1.502 $\pm$ 0.013
	z	-0.587 $\pm$ 0.04	-0.481 $\pm$ 0.018	0.969 $\pm$ 0.003	1.861 $\pm$ 0.013

Table 3.3: Cloud Positions and Sizes – Measured immediately before and immediately following the optical pumping phase of the trapping cycle. Measurements are evaluated using rMCP runs, and are taken to describe the cloud during associated eMCP runs as well. All entries are expressed in units of millimetres, and the size parameters describe the gaussian width.

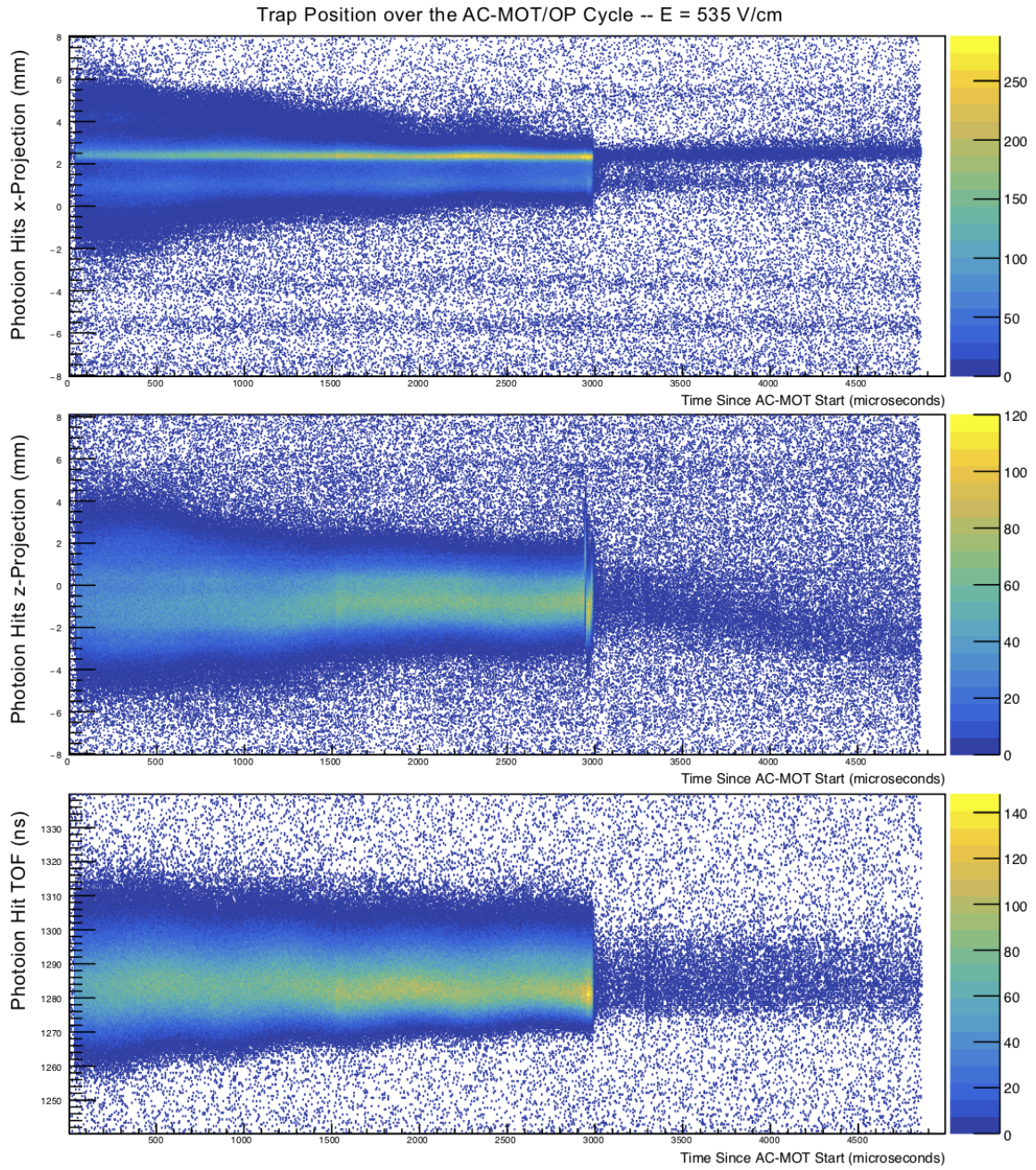


Figure 3.5: Projections of photoion hit positions and TOF at 535 V/cm, as a function of time since the start of the last AC-MOT cycle. The trap's periodic motion can be seen in sync with the AC-MOT's cycles, and it is clear that the cloud is also being compressed during this time, before being allowed to expand ballistically when the MOT is shut off. The photoion burst at the start of optical pumping 300  $\mu$ s after the AC-MOT is shut off can be seen on the lower two plots.

## 3.5 Electron Run Data Selection and Preliminary Cuts

Before proceeding further, several basic cuts are performed on the data. For the Electron Runs which are to be processed directly into a physical measurement, we consider only events in which there was a recorded hit *both* on the eMCP *and* on exactly one of the scintillators. The required scintillator hit, of course, is potentially a beta, and so it is obvious why this must be present. Events in which both scintillators record a hit are discarded, as they fall into two categories: an accidental coincidence, where we are seeing two different decays that, by chance, both occurred within the time window allocated to a single event (a few  $\mu\text{s}$  before and after the first recorded scintillator hit), a backscatter event in which a beta was incident on one scintillator before being scattered out into the opposite scintillator. Although it would be possible to process the former event type into usable information if we could be certain that it was truly an accidental coincidence, contamination from the latter event type would serve to increase the systematic uncertainty arising from beta scattering—already a dominant source of error.

The eMCP is used primarily to record incident shake-off electrons. As described in Section 1.5, every beta decay event will produce one or more SOEs. Most (but not all) SOEs originating from the atom cloud will be incident on the eMCP, however not all incident SOEs on the eMCP will produce a recorded hit. The electric field is such that SOEs originating elsewhere within the chamber may or may not be incident on the eMCP. Therefore, while imposing an eMCP hit requirement will eliminate some ‘good’ events originating from the cloud, it also eliminates a much larger fraction of background events originating from other surfaces within the chamber. This ability to ‘tag’ good events originating in the cloud is absolutely essential to any analysis involving angular correlations within this geometry.

In later sections, we will consider how to evaluate a further cut to be imposed on the time difference between scintillator and eMCP hits (Section 3.8), and some subtleties within analysis relating to this choice (Sections 4.4 and 4.5).

It is also necessary to remove from direct consideration any event which is coincident with a pulse from the photoionization laser. When photoionization occurs within the atom cloud, an orbital electron is removed from the atom and will be accelerated

by the electric field into the eMCP, just as a shake-off electron from a decay would be. If, by chance, this photoelectron arrives in coincidence with a scintillator hit, it would be interpreted as a decay event from the trap – unless we preemptively discard it.

Over the course of the runtime, there were several instances where we noted an apparent electrical discharge within the experimental chamber, producing enormous backgrounds for a short time. The detectors typically recovered quickly afterward, so it was neither necessary nor useful to stop an entire run to wait for the system to recover. Instead, the time when the discharge occurred was recorded, and events within approximately one minute of the spark time were discarded.

We use only the “fully polarized” events for which we have a detailed understanding of the nuclear polarization (described in more detail in [15]). This means we must use *only* events from the “optical pumping” portion of the duty cycle (see Fig. 2.3), and discard events when the DC- or AC-MOT is active. After the AC-MOT is shut off, there is a short delay before optical pumping begins (see Tables 3.1 and 3.2) to allow the magnetic field to decay, and it is only after  $100\,\mu s$  of optical pumping that we consider the atoms to be fully polarized. Furthermore, because the magnetic field from the DC-MOT is slow to decay (relative to the field from the AC-MOT), all events from the first five AC/OP cycles after every atom transfer are discarded. A further benefit of our insistence on considering only polarized data is that the scintillators’ gains are more stable in the presence of only the (small, stable) magnetic field used for optical pumping than they are in the presence of a larger oscillating magnetic field used for trapping [21].

Finally, because this analysis depends heavily on energy measurements from the two scintillators as a proxy for beta energy, it is necessary to remove events in which the pulser LED fired. Although the pulser LED is useful for evaluating the stability of the scintillators, in the case where an LED pulse occurs together with a true beta hit in the scintillator, it may change the measured energy. Therefore, we discard all events that include an LED pulse.

## 3.6 Further Cuts Using the DSSD

The DSSDs are critical to our ability to veto background events in which the particle incident on the detector is a gamma ray rather than a beta — e.g., from annihilation radiation — however, they must be properly calibrated in order to be useful. The calibration was performed by other members of the collaboration, and the methodology is described in detail in [21]. It is summarized here for clarity.

Although it was not possible to use the DSSD in real-time analysis or event triggering, the DSSDs may be used, after the data has been collected, to distinguish between different types of particles incident on the detector, as more energy will be deposited by heavier particles. When a scintillator hit is triggered by a particle originating within the experimental chamber, that particle will typically have passed through the DSSD before arriving at the scintillator.

In the present experiment, the two primary particles that will concern us are  $\beta^+$  particles originating from the decay of  $^{37}\text{K}$ , and  $\gamma$  rays, which may be produced through a variety of processes, e.g. directly from the 2% decay branch, through annihilation of  $\beta^+$  particles upon their interaction with regular-matter electrons, or bremsstrahlung radiation from emitted  $\beta$ s.

We would like to look specifically at events involving  $\beta^+$  particles arriving direct from a decay within the atom cloud, and the DSSD may be used to eliminate events in which the scintillator is triggered by a  $\gamma$ . An incident  $\beta$  will typically deposit some portion of its energy in the DSSD as it passes through, however an incident  $\gamma$  will deposit significantly less energy; for this setup the energy deposited by a  $\gamma$  is generally indistinguishable from background on the DSSDs. Therefore, we require that a ‘good’ event must include a ‘good’ hit to the DSSD as well as a hit to the associated scintillator.

In order to proceed at this point, and because the DSSD readout records so much information, it is necessary to develop some criteria to determine whether or not we will accept any given DSSD readout as a  $\beta$  hit.

We read out the full waveform for every strip at each event with a scintillator hit, but in post-processing take *only* the ‘time’ and ‘energy’ from the waveform’s peak. Each strip will have its own noise spectrum, energy calibration, and energy resolution. To classify an event as a good DSSD hit, we first require a good scintillator hit (as determined by the associated TDC readout) with energy above a nominal 10 keV to

eliminate pedestal events, and no pulser LED.

We further require at least one ‘x’ strip and one ‘y’ strip within that same detector record an energy above the ‘noise threshold’, which is determined individually for each strip, and is defined according to the signal-to-noise (SNR) ratio. In other words, for each individual strip, the energy at which a certain fraction of events are ‘real’ events (as opposed to electronic noise) defines a particular ‘noise threshold’. Values are tabulated for each strip at SNRs of 0.25, 0.5, 0.75, 1.0, and 2.0. As a default, the strip-by-strip SNR of 0.25 is used.

We require that the x strip and the y strip agree (to within some number of standard deviations — this is a parameter that can be varied) in amount of energy deposited, and in the time at which that hit occurred. In order to avoid problems resulting from the strips’ non-uniform noise thresholds, we further require that the energy deposited be greater than some lower-end cutoff which is selected so as to be higher than every individual strip’s noise threshold. In this case, the DSSDs’ lower energy uniform threshold was set at 50 keV, a departure from the choice of 60 keV in an earlier analysis [19] [21].

We also elect to use only events where a beta hit the DSSD within a 15.5 mm radius of the center of the detector, as a large fraction of the DSSD hits at larger radii are from betas that have scattered from the collimator walls. Furthermore, events with more than *one* DSSD hit are rejected, as these events are likely either accidental coincidences of two beta decays, or else the result of betas scattering out of a scintillator before their energy can be fully absorbed.

### 3.7 Further Cuts Using the Scintillators

After all other cuts have been performed, a further cut is made on scintillator energy. It is important that this cut must be performed *after* event vetoes from more than one scintillator being hit are applied, and after the DSSD event vetoes have also been applied, in order to avoid unexpected behaviour in which we fail to reject certain classes of events that we had intended to reject.

For both scintillators, only events where the absorbed energy is between 400 and 4800 keV are accepted. The high energy cutoff is selected so far below the beta cutoff energy ( $Q = 5.125 \text{ MeV}$ ) because the low counting statistics at higher energies

result in our observable, the superratio asymmetry, being poorly defined and poorly behaved. In later evaluating the systematic error associated with that cut, spectra with lower cutoffs ranging from 300 to 600 keV are considered, and spectra with upper energy cutoffs between 4600 and 5100 keV are considered separately.

### 3.8 Timing Improvements with the Leading Edge and Scintillator Walk Correction

The eMCP features a set of three delay lines, intended to be used to record the position of a hit. Though only two delay lines is sufficient to determine the position within the plane of the MCP if they are both hit, the presence of a third delay line allows for some redundancy. In practice, however, a large fraction of otherwise ‘good’ events include a hit on the eMCP, but have insufficient information recorded on the delay line channels to reconstruct a position.

Because a SOE from the trap is most likely to land in the centre of the plate, while *a priori* the background from other sources not expected to have any particular spatial distribution, it might make sense to accept only events where the eMCP hit is within some radius of the central peak. This methodology was seriously considered because the remaining data after this cut is taken has a much lower fraction of background events polluting it – however even for the most generous eMCP radius cuts, this results in a loss of about half of the events. The overall measurement is limited by statistics rather than systematics, so it was decided that no cuts on eMCP hit position would be taken in the final analysis.

Several years after the data was initially collected, a problem was discovered with our low-level analyzer software, which we had been using to convert large and unwieldy MIDAS data sets into somewhat smaller and more manageable ROOT data sets. In particular, for every timestamp recorded, our raw MIDAS data actually included both a timestamp for the leading edge (LE) of the pulse, and a timestamp for the trailing edge (TE). The analyzer had—for years—been reporting the timestamp associated with the trailing edge of the pulse. Initially it was unclear if there might have been a reason behind this choice, but a closer examination of the data showed that the LE data included less timing jitter and noise, as well as a sharper peak for timing pulses across the board (as in Fig. 3.6), with some channels showing a larger effect than

others. This was corrected, and the entirety of this analysis has been performed now using the cleaner LE spectra.

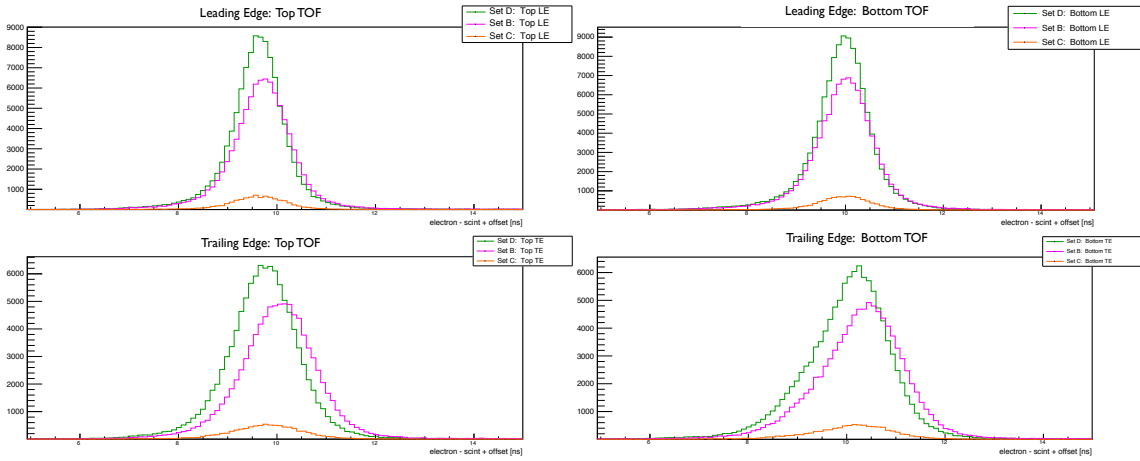


Figure 3.6: SOE TOF peaks (eMPC - Scintillator), using the leading edge (LE) and using the trailing edge (TE). Data is sorted according to runset. For each individual runset, the TE peak is broader than the LE peak. The centroid of each runset is also more variable in the TE plots.

The place where this change between the TE and LE timestamps had the biggest impact on the analysis is in the shake-off electron time-of-flight spectra, on which a cut must eventually be taken. Although this problem was not discovered in time to be used in the previous measurement of  $A_\beta$  using this same data [19], it likely would have had a negligible effect on the final result, because the SOE TOF cut that was used there was comparatively loose, and the evaluation of the background that remained was not a dominant systematic effect.

With the data reprocessed using the leading edge for timestamps, I wanted to eliminate as much background as possible from the SOE TOF spectrum. With this goal in mind, the next step was to correct the scintillator timing for its low energy ‘walk’ (see Fig. 3.7). A quartic polynomial was fit to each of the 2D timing vs energy spectra (the top and bottom detectors were treated separately), and the result was used to produce a ‘straightened’ SOE TOF spectrum with respect to measured scintillator energy, and as expected, the resulting SOE TOF spectrum was a bit more sharply peaked.

With the SOE TOF spectra cleaned up, a cut can be taken to reduce the fraction of background events. Informed by the model of background spectra described in

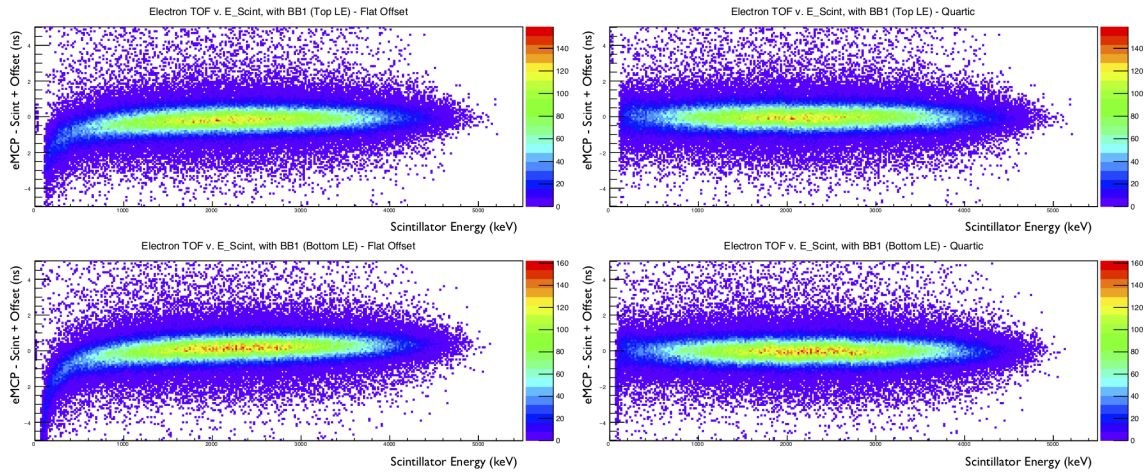


Figure 3.7: SOE TOF walk, before (left) and after (right) applying a quartic adjustment to straighten out the effective TOF.

Section 4.5, a cut was made to include only a 2.344 ns window around the primary peak in further analysis (see Fig. 4.12). With all cuts included, the four cleaned scintillator spectra corresponding to combinations of detector and polarization direction are plotted in Fig. 3.8.

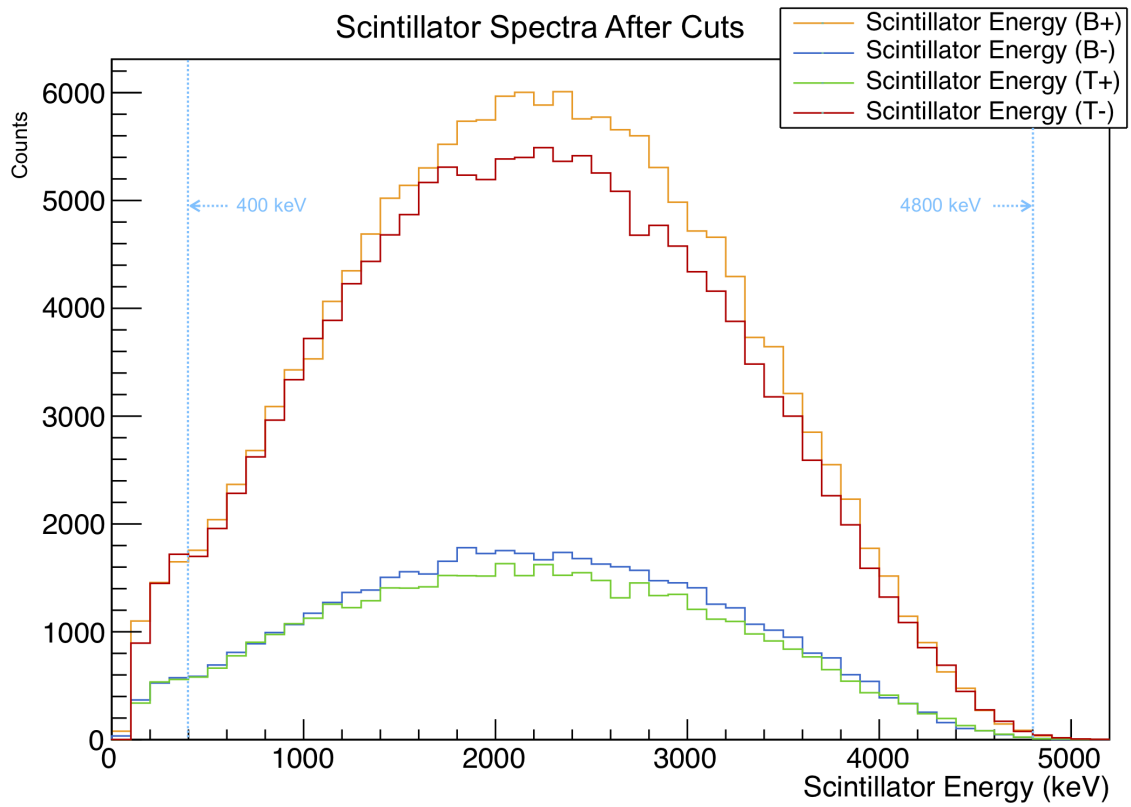


Figure 3.8: Experimental scintillator spectra, for both detectors in both polarization states. These spectra are what remain after all cuts have been taken, and all runsets are included. Binning is selected to match the convention used for the final analysis.

# Chapter 4

## Simulations

The TRINAT collaboration has created a Geant4 (G4) simulation which models the geometry and materials within the experimental chamber, and uses a monte carlo algorithm to describe generalized physical processes such as particle scattering and energy loss, within the geometry specific to the experiment. This software library has been maintained and updated over several generations of graduate students [21] [22].

### 4.1 Considerations for Software Upgrade Implementation

Prior to the simulations required for this particular experiment, two different sets of changes to the G4 code were needed – the first to enable multithreading, and the second to introduce certain BSM interactions to the decay distribution.

Enabling multithreading allows for a single instance of the Geant4 simulation to run on several processors at once, effectively speeding up the overall simulation by a factor of the number of processors used. In the years since the simulation was originally created, the Geant4 collaboration had created libraries intended specifically to support multithread usage, and since the running G4 simulations had historically been very time consuming for the TRINAT collaboration, the decision was made to implement multithreading within our own monte carlo software, on the hopes that this would enable faster progress in analysis.

Enabling multithreading support turned out to be quite time consuming, and in the end it might have been faster to have spent those months running simulations one

processor at a time. Perhaps the improvement will prove valuable for use in future TRINAT experiments.

The TRINAT G4 monte carlo package had never been used to directly model interactions beyond the standard model within the decay physics. It had previously been set up by the collaboration to use a probability density function (PDF) including most of the terms from Holstein's Eq. (51) [10], which describes both electron and neutrino momenta from polarized beta decay. This treatment is quite robust, and includes corrections at recoil-order, as well as certain other corrections of similar size.

Unfortunately, terms arising from interactions beyond the standard model are not included in Holstein's description of the decay process. To understand the kinematic results of the exotic interactions of interest to us here, we turn to the classic JTW treatment of beta decay [8] [9]. In addition to the (expected) vector and axial interactions, JTW also describes the interaction in terms of (exotic) scalar and tensor interactions, should such be present. Despite JTW's broad ability to describe beta decay under a variety of physical models, this treatment includes only the leading-order terms, and smaller terms, such as recoil-order corrections, are neglected entirely.

Because the present project is a precision measurement of the Fierz interference, a term which arises from scalar and tensor couplings, it was imperative to create an event generator for our G4 simulations that could account for these exotic interactions while also including in its PDF the higher-order effects which, in some cases, can mimic the effects of a scalar or tensor current.

While it might have been possible to directly combine JTW's result with Holstein's Eq. (51), it should be noted that JTW's expression is not compatible in general with the principle of conservation of momentum; as recoil momentum is neglected entirely, the description is only of two leptons emerging from a nucleus in directions that do not directly oppose one another. Therefore, the prospect of combining these two slightly incompatible expressions directly might be enough to give one pause. On an experimental level, the mathematical description of an emerging neutrino is only of interest to us to the extent we can reconstruct it based on detecting both a beta and the recoiling nucleus from a single decay event, and within the present experiment we do not have simultaneous access to both a beta detector and a recoil detector.

In light of the above considerations, it was decided that an entirely new event generator must be created, based instead on Holstein's Eq. (52), in which neutrino momentum has been integrated over and is therefore no longer an explicit part of the

PDF [10]. As one might guess, Holstein's Eq. (52) is greatly simplified in comparison to Holstein's Eq. (51). A similar integration over all possible neutrino momenta can also be performed on the JTW PDF, causing several terms to vanish. The result in both the Holstein and JTW cases is a PDF over only beta energy and direction as measured with respect to nuclear polarization, and the two expressions can be combined in a straightforward manner by comparing similar terms.

It is this combined Holstein+JTW expression that forms the basis of the new G4 event generator. It must be noted that although the largest effect from any present scalar or tensor interactions would likely (depending on certain phase angles) be in a non-zero value of  $b_{\text{Fierz}}$ , these interactions can also introduce a perturbation to  $A_\beta$  at a higher order. In order for any precision experimental measurement of  $b_{\text{Fierz}}$  to be generalized to limits on the parameter space of scalar and tensor currents, it is important to incorporate an accurate representation of the results of such exotic interactions on *all* available observables, and the new G4 event generator does this.

## 4.2 Simulations for the Ninety-eight Percent Branch and the Two Percent Branch

With the new event generator, our G4 simulations are able to generate  $^{37}\text{K}$  decay events mediated by Weak interactions with arbitrarily sized scalar and tensor couplings. For simplicity of analysis, and because scalar and tensor couplings produce similar effects on parameters  $A_\beta$  and  $b_{\text{Fierz}}$ , the decision was made to vary only the scaling of one particular set of BSM coupling constants within the Geant4 simulations. In particular, high-statistics simulations were performed using scalar coupling values,

$$g_S := \frac{1}{\sqrt{2}}(C_S + C'_S) = \{0, \pm 0.1\}, \quad (4.1)$$

a combination that describes left-handed scalar interactions. These sets of parameters produce values of  $b_{\text{Fierz}}$ , and perturbations to values of  $A_\beta$ , given by:

$$b_{\text{Fierz}} \approx \{0, \mp 0.148661\} \quad (4.2)$$

$$\Delta A_\beta \approx \{0, -0.004259\}, \quad (4.3)$$

where we note that the change to the value of  $A_\beta$  is small relative to  $b_{\text{Fierz}}$ , and always has the same (negative) sign no matter the sign of  $b_{\text{Fierz}}$ , because while  $b_{\text{Fierz}}$  scales linearly with  $g_T$ , the perturbation to  $A_\beta$  arises from a quadratic term.

In addition to simulations of the dominant decay branch, it is also necessary to create simulations with sufficient statistics of the subleading (“two percent”) branch. Because it is responsible only for a small fraction of the overall spectrum, we do not include corrections from BSM parameters in these simulations. These simulations are performed separately from the main branch simulations, and are evaluated using the older Geant4 event generator based on Holstein’s Eq.(51) [10]. Simulated events from both branches are combined together in the appropriate ratio before further processing is performed.

### 4.3 The Simple Monte Carlo and Response Function

Scattering (both forward scattering and backscattering) is an important effect to consider within this experiment, and it must be evaluated through extensive and time consuming monte carlo simulations – in this case, using Geant4. However, there are a number of other systematic uncertainties that must also be evaluated, and it is computationally prohibitive (even after multithreading support was implemented) to evaluate all of them via the same sort of high statistics, scattering included, full monte carlo that we use for scattering effects. Luckily, the systematic effects arising from scattering are largely decoupled from other effects, and this section describes the framework that has been implemented in order to evaluate certain other systematic effects separately.

To this end, a fast-running Simple Monte Carlo (SMC) was developed together with an empirical “response function” similar to the one described by Clifford et al [23] to describe probabilistic beta energy loss before its detection in a scintillator. In the end, the lineshape description became quite involved, and it is unclear whether, in the end, any time was saved this way.

The purpose of the SMC was to *quickly* generate initial particle kinematics probabilistically for beta decay events, and it uses the very same event generator based on Holstein’s Eq. (52) [10] that was developed for use with the more sophisticated Geant4 simulations. However, unlike in a G4 simulation, the SMC makes no attempt

to track particles through the chamber, and instead simply calculates detector hits based on initial particle momentum. This procedure obviously neglects scattering effects, which can (in differing regimes) both *increase* and *decrease* the number of beta particles incident on a detector. Furthermore, this procedure also neglects any energy absorption in materials through which the beta passes before hitting a scintillator – and the beta *must* pass through several such materials (see Fig. 2.5).

To make the best use of the SMC for evaluating systematic errors, the energy lost before a beta hits a scintillator must be accounted for somehow in order to ensure all relevant physical effects are propagated through. In particular, before hitting a scintillator, a beta must pass through a  $275\ \mu m$  thick silicon carbide mirror, a  $229\ \mu m$  thick beryllium foil, and finally a set of  $300\ \mu m$  thick double-sided silicon strip detectors (DSSDs), before finally having its remaining energy absorbed within a scintillator. Although the DSSDs are themselves detectors with the ability to record the amount of energy deposited by an incident particle, there are some known problems in achieving a uniform level of precision across the full surface of the DSSDs, so adding the DSSD energy back to the scintillator energy to produce a better estimate of the original beta energy has the potential to create some problems for the analysis. Furthermore, given the presence of the mirror, an object with a similar thickness and scattering properties to the DSSDs, re-adding the energy lost in the DSSDs would not eliminate the need to estimate probabilistic energy loss in similar materials.

In order to create a quantitative description of the effective response function, which varies with initial beta energy, an analytic function of 14 parameters has been created to model scintillator output for decays from the central cloud for each of the two polarization states in use. In other words, although the form of the model is always the same, the 14 individual parameters will take different values for each of the four detector and polarization combinations. The full response function model is given by the expression,

$$R(E_0, \text{Detector}, \text{Polarization}) = p_{\text{norm}} (f_{\text{moyal}} + f_1 + f_2 + f_3 + f_4 + f_5) + f_{511}, \quad (4.4)$$

where  $p_{\text{norm}}$  is one parameter, and the other terms within the expression are themselves functions of multiple parameters and are given by,

$$f_{\text{moyal}} = (1 - p_{\text{gfrac}}) \left( 1 + \frac{-p_\alpha - p_\beta}{|E_0|} - \frac{p_\Delta}{p_\gamma p_W} - p_\gamma p_W \right) \\ \times \left( \frac{e^{\left( \frac{x - (E_0 - \frac{1}{2}p_{\text{dE0}})}{2p_{\text{lres}}|E_0 - \frac{1}{2}p_{\text{dE0}}|} \right)} e^{\left( -\frac{1}{2}e^{\left( \frac{x - (E_0 - \frac{1}{2}p_{\text{dE0}})}{p_{\text{lres}}|E_0 - \frac{1}{2}p_{\text{dE0}}|} \right)} \right)}}{\sqrt{2\pi p_{\text{lres}}|E_0 - \frac{1}{2}p_{\text{dE0}}|}} \right), \quad (4.5)$$

$$f_1 = p_{\text{gfrac}} \left( 1 + \frac{-p_\alpha - p_\beta}{|E_0|} - \frac{p_\Delta}{p_\gamma p_W} - p_\gamma p_W \right) \left( \frac{e^{\left( -\frac{(x - (E_0 + \frac{1}{2}p_{\text{dE0}}))^2}{2p_{\text{toeres}}|E_0 + \frac{1}{2}p_{\text{dE0}}|} \right)}}{\sqrt{2\pi p_{\text{toeres}}|E_0 + \frac{1}{2}p_{\text{dE0}}|}} \right), \quad (4.6)$$

$$f_2 = \frac{p_\alpha}{|E_0|} \left( \frac{1 - \text{Erf} \left[ \frac{(x - |E_0|)}{\sqrt{2p_{\text{toeres}}|E_0|}} \right]}{2|E_0|} \right), \quad (4.7)$$

$$f_3 = \frac{p_\beta}{|E_0|} \left( \frac{e^{\frac{p_k * (x - E_0)}{|E_0|}} * e^{\frac{p_{\text{toeres}} p_k^2}{2|E_0|}}}{2(1 - e^{-p_k})} \right) \left( 1 - \text{Erf} \left[ \frac{(x - E_0 + p_{\text{toeres}} p_k)}{\sqrt{2p_{\text{toeres}}|E_0|}} \right] \right), \quad (4.8)$$

$$f_4 = \frac{p_\gamma}{2} \left( \text{Erf} \left[ \frac{x - E_0}{\sqrt{(2p_{\text{toeres}}|E_0|)}} \right] - \text{Erf} \left[ \frac{x - E_0 - p_W}{\sqrt{2p_{\text{toeres}}|E_0 + p_W|}} \right] \right), \quad (4.9)$$

$$\begin{aligned}
f_5 = & \frac{p_\Delta}{2 p_\gamma p_W^3} \left[ (x - E_0) \left( \operatorname{Erf} \left[ \frac{(x - E_0)}{\sqrt{2 p_{\text{toeres}} |E_0|}} \right] - 2 \operatorname{Erf} \left[ \frac{(x - E_0 - p_W)}{\sqrt{2 p_{\text{toeres}} |E_0 + p_W|}} \right] \right. \right. \\
& + \operatorname{Erf} \left[ \frac{(x - E_0 - 2p_W)}{\sqrt{2 p_{\text{toeres}} |E_0 + 2p_W|}} \right] \Big) + (2 p_W) \left( \operatorname{Erf} \left[ \frac{(x - E_0 - p_W)}{\sqrt{2 p_{\text{toeres}} |E_0 + p_W|}} \right] \right. \\
& \left. \left. - \operatorname{Erf} \left[ \frac{(x - E_0 - 2p_W)}{\sqrt{2 p_{\text{toeres}} |E_0 + 2p_W|}} \right] \right) + (2 p_{\text{toeres}} |E_0|) \left( \left( \frac{e^{\left( \frac{-(x-E_0)^2}{(4 p_{\text{toeres}} |E_0|)} \right)}}{\sqrt{2\pi p_{\text{toeres}} |E_0|}} \right) \right. \\
& \left. \left. + \left( \frac{-2e^{\left( \frac{-(x-E_0-p_W)^2}{(4 p_{\text{toeres}} |E_0+p_W|)} \right)}}{(\sqrt{2\pi p_{\text{toeres}} |E_0 + p_W|})} \right) + \left( \frac{e^{\left( \frac{-(x-E_0-2p_W)^2}{(4 p_{\text{toeres}} |E_0+2p_W|)} \right)}}{\sqrt{2\pi p_{\text{toeres}} |E_0 + 2p_W|}} \right) \right) \right), \quad (4.10)
\end{aligned}$$

and

$$\begin{aligned}
f_{511} = & |p_{\text{scale}}| \left[ \left( \frac{195}{17} \sqrt{\frac{2}{\pi}} e^{\left( \frac{-(x-308)^2}{578} \right)} \right) + \left( 40 + \frac{(x-210)^2}{900} \right) \left( 1 - \operatorname{Erf} \left[ \frac{x-334}{30} \right] \right) \right. \\
& \left. + \left( \frac{(x-505)^2}{1440} \right) \left( 1 - \operatorname{Erf} \left[ \frac{x-505}{30} \right] \right) \left( 1 + \operatorname{Erf} \left[ \frac{x-334}{30} \right] \right) \right], \quad (4.11)
\end{aligned}$$

where a  $p$  with any subscript is taken to be a variable parameter that must be evaluated. The expressions  $f_1$ ,  $f_2$ ,  $f_3$ ,  $f_4$ , and  $f_5$  are motivated by or taken directly from expressions of the same name within Clifford's description, and the individual parameters  $p_\alpha$ ,  $p_\beta$ ,  $p_\gamma$ ,  $p_\Delta$ ,  $p_W$ , and  $p_k$  are closely related to their counterparts of similar name [23]. The expressions  $f_{\text{moyal}}$  and  $f_{511}$  represent a departure from the published treatment, however, and arise from physical behaviours within this experiment which are not described within Clifford's treatment.

In particular,  $f_{511}$  is a rather inelegant representation of the annihilation radiation compton edge within our geometry. Although the DSSD provides an effective veto for the overwhelming majority of these events—and indeed within Clifford's treatment this veto is treated as being perfect in its discernment—it is clear both from experimental spectra and the Geant4 simulations intended to represent them that there exist a small number of such events within our scintillator spectra that cannot be vetoed in this manner. These events must be understood and adequately accounted for.

It should be noted that no attempt is made to derive the expression for  $f_{511}$  from first principles; the expression was chosen only because of its visual similarity to the spectrum's fit residuals before its inclusion. This expression's contribution to the overall function is negligible at all but the lowest initial beta energies (Eq. 4.11's  $p_{\text{scale}}$  parameter, showing the absolute normalization of  $f_{511}$ , is plotted in the top right of Fig. 4.7.), and is always negligible at scintillator energies above  $\sim 500$  keV, as can be seen in Fig. 4.5. We note that within the final analysis, all scintillator spectra will be given a low energy cutoff at 400 keV, so the only the higher energy tail of  $f_{511}$  will make any contribution.

The expression  $f_{\text{moyal}}$  arises from the beta particles' energy loss within materials (i.e. the mirror, the beryllium foil, and the DSSD itself, as in Fig. 2.6) before its eventual absorption within the scintillator. Although Clifford's treatment does include a  $\Delta E$  detector (our DSSD would be the equivalent), the energy absorbed in this detector is added back in to the total before Clifford's final spectra are modeled. Although it would be possible to do something similar with our DSSD spectra, we would still be left with the problem of accounting for the similarly-shaped energy loss within the mirror and foil.

The distribution for energy deposition within a thin material by an energetic charged particle, first described by Lev Landau in 1944 [24], is now known as a Landau distribution. This distribution has a variety of properties that make it challenging to work with – notably its mean, variance, and all higher moments are undefined, and the distribution itself cannot be written in closed form. Its primary redeeming mathematical feature, however, is the fact that the convolution of a Landau distribution with another Landau distribution is, itself, a Landau distribution, and this means that we can represent the sum total of energy absorption within three successive thin materials as a single Landau distribution.

Within the present context, an expression for energy absorption that can be evaluated and re-evaluated quickly by computer with adjusted parameters is needed, as this must be used within a fit function. To this end, we employ a so-called ‘Moyal function’, which was developed in 1955 to be used as a closed form approximation to the Landau distribution [25]. Indeed, Eq. 4.5 is little more than a Moyal function.

The values of these parameters are allowed to vary with initial beta energy, and must be determined empirically by a series of fits to simulated spectra. To effect this result, the TRINAT Geant4 simulation is used to generate a series of ‘mono-

energetic' spectra. That is, for each energy value under consideration (with discrete values selected to span the energy range of betas in our decay), events are generated in which every outgoing beta initially has the same amount of kinetic energy, and the angular distribution of these betas is physically appropriate for the polarization and beta energy under consideration. These mono-energetic betas are propagated through the experimental geometry via Geant4, and the resulting scintillator spectra are recorded. Each polarization state must be considered separately, but spectra for both detectors are generated simultaneously, as it is necessary to generate events into a full  $4\pi$  steradians in order to fully account for betas scattered into- or away from the detectors. Cuts identical to those imposed on the experimental data are applied (see Chapter 3). Several such spectra are shown for the Bottom Detector in the ‘-’ polarization state, with their best fit response functions, components thereof, and residuals of the fit, in Figs. 4.1, 4.2, 4.3, 4.4, and 4.5.

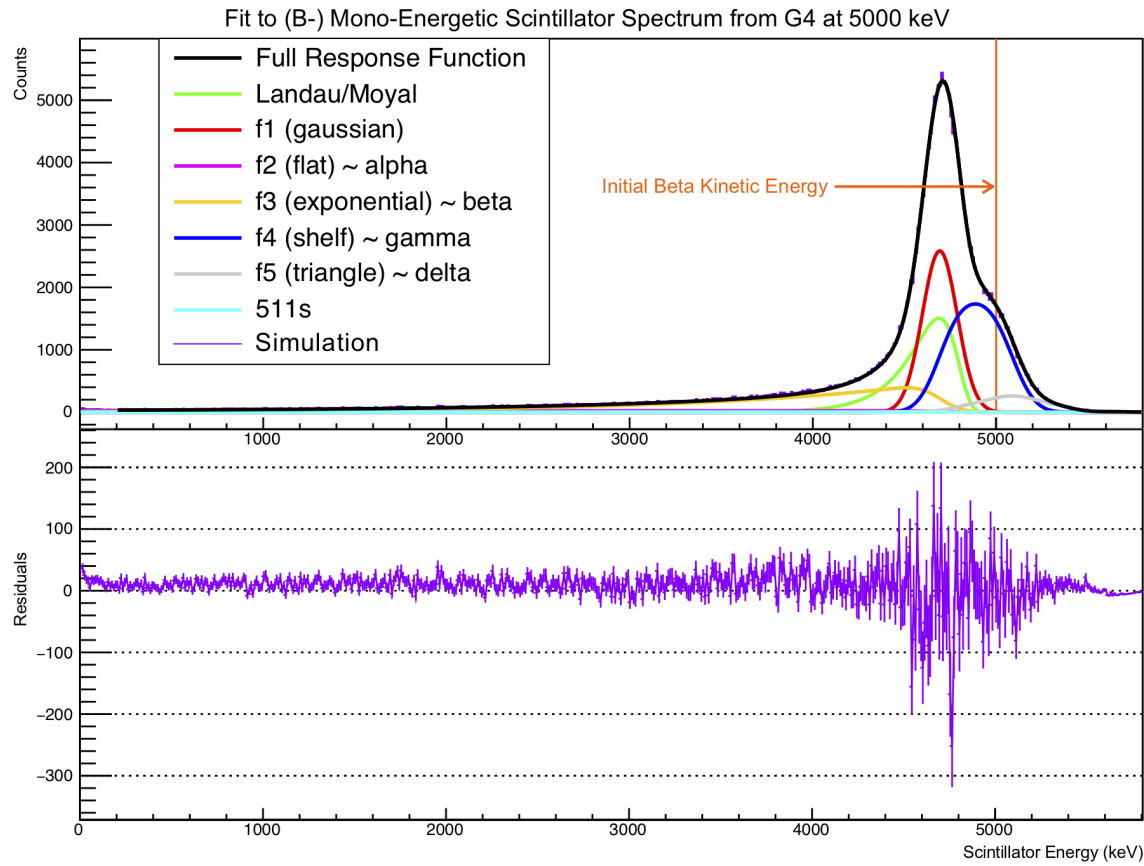


Figure 4.1: Fit to Mono-Energetic Spectrum, 5000 keV (B-)

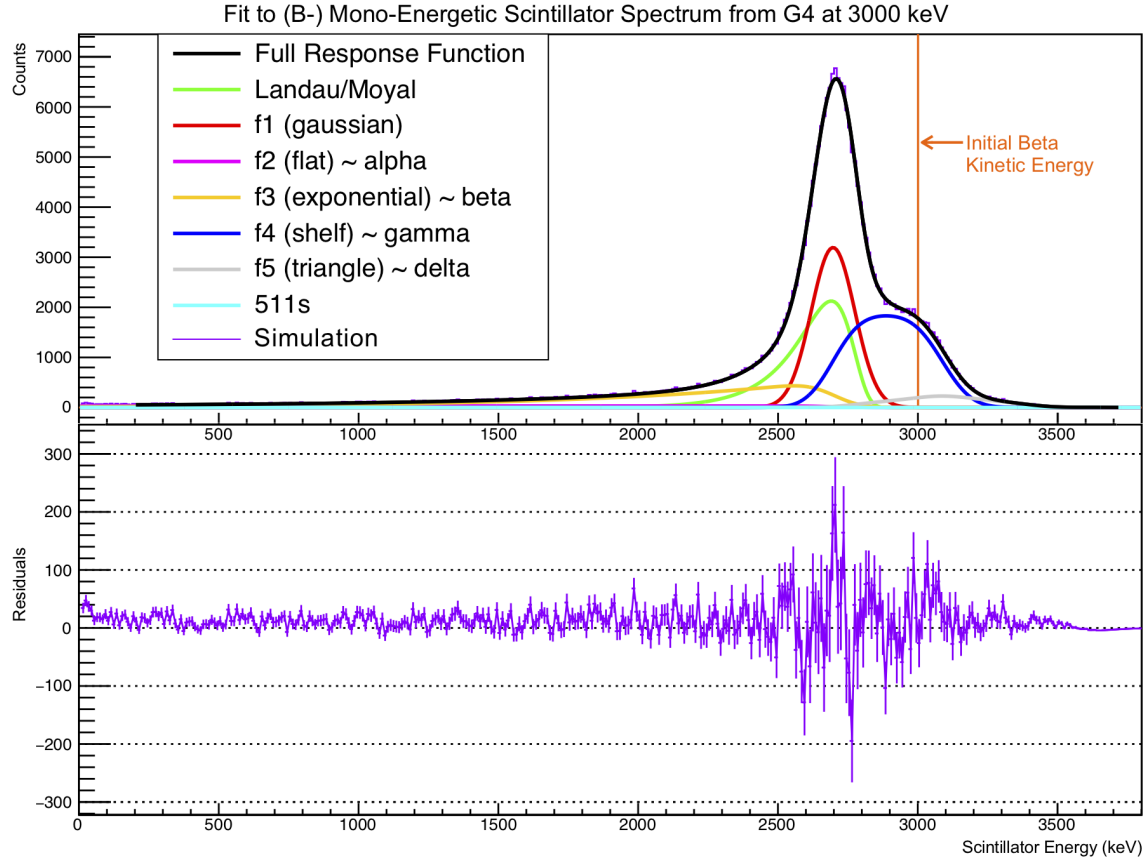


Figure 4.2: Fit to Mono-Energetic Spectrum, 3000 keV (B-)

The values of the individual parameters contributing to the fit functions in, eg, Figs. 4.1, 4.2, 4.3, 4.4, and 4.5 are allowed to vary with initial beta energy, and the energy dependence of each parameter must be modeled in order to extrapolate the shape of the response function to intermediate initial beta kinetic energy values that are not explicitly modeled. For each parameter, the energy dependence is modeled by an analytic function selected to have similar characteristics. Each of these analytic functions is itself a function of several parameters which can be adjusted to optimize its fit to the true best-fit energy dependence of the parameter it models. Because some parameters are only weakly independent, it is necessary to perform these fits iteratively on only a single parameter at a time, revisiting earlier parameter fits after fixing other parameters to updated models. The results of this process are shown in Figs. 4.6, 4.7, 4.8, and 4.9.

It is useful to consider how well this empirical response function works to model the

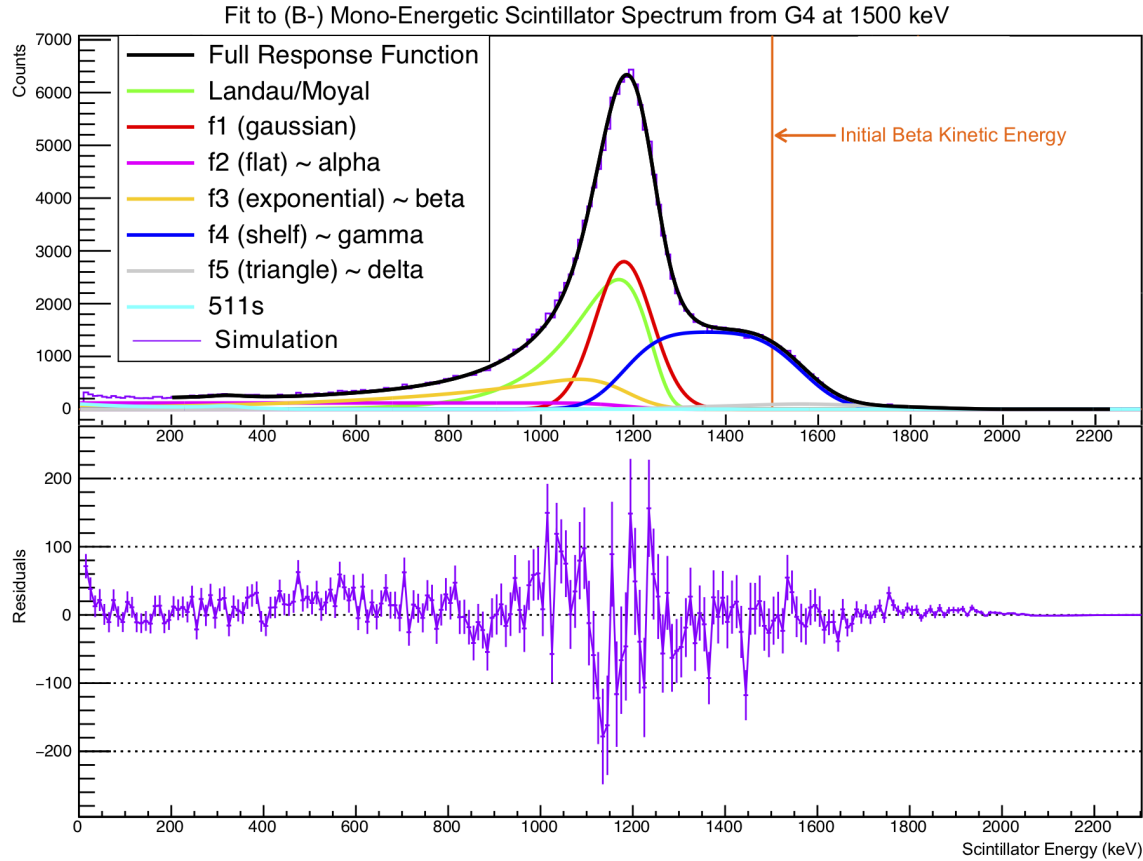


Figure 4.3: Fit to Mono-Energetic Spectrum, 1500 keV (B-)

spectra. One can see clearly from Figs. 4.1, 4.2, 4.3, 4.4, and 4.5 that the fit residuals appear noticeably *worse* at lower initial beta energies. Fig. 4.10 shows the reduced  $\chi^2$  values arising from comparing mono-energetic G4 spectra to the empirical response functions described above, for all four detector and polarization combinations.

With the energy dependence for each of the response function's parameters carefully modeled, it becomes possible to make proper use of the full response function. Given a decay event with a known beta energy from a nucleus with its initial polarization known, we can now predict a probabilistic response from *both* scintillator detectors. Obviously, for a single decay event, the full spectrum cannot be realized – however in aggregate the modeled response function agrees well with results from the full Geant4 simulation, particularly at higher beta energies.

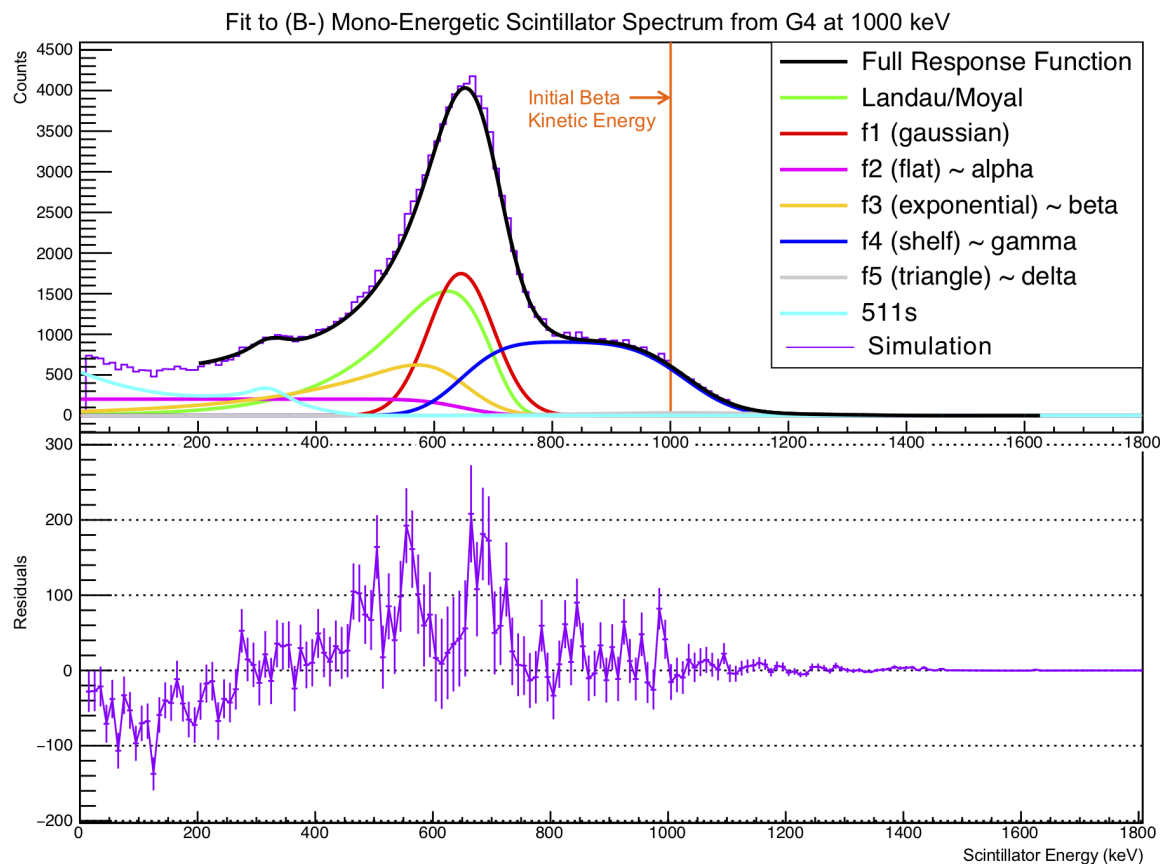


Figure 4.4: Fit to Mono-Energetic Spectrum, 1000 keV (B-)

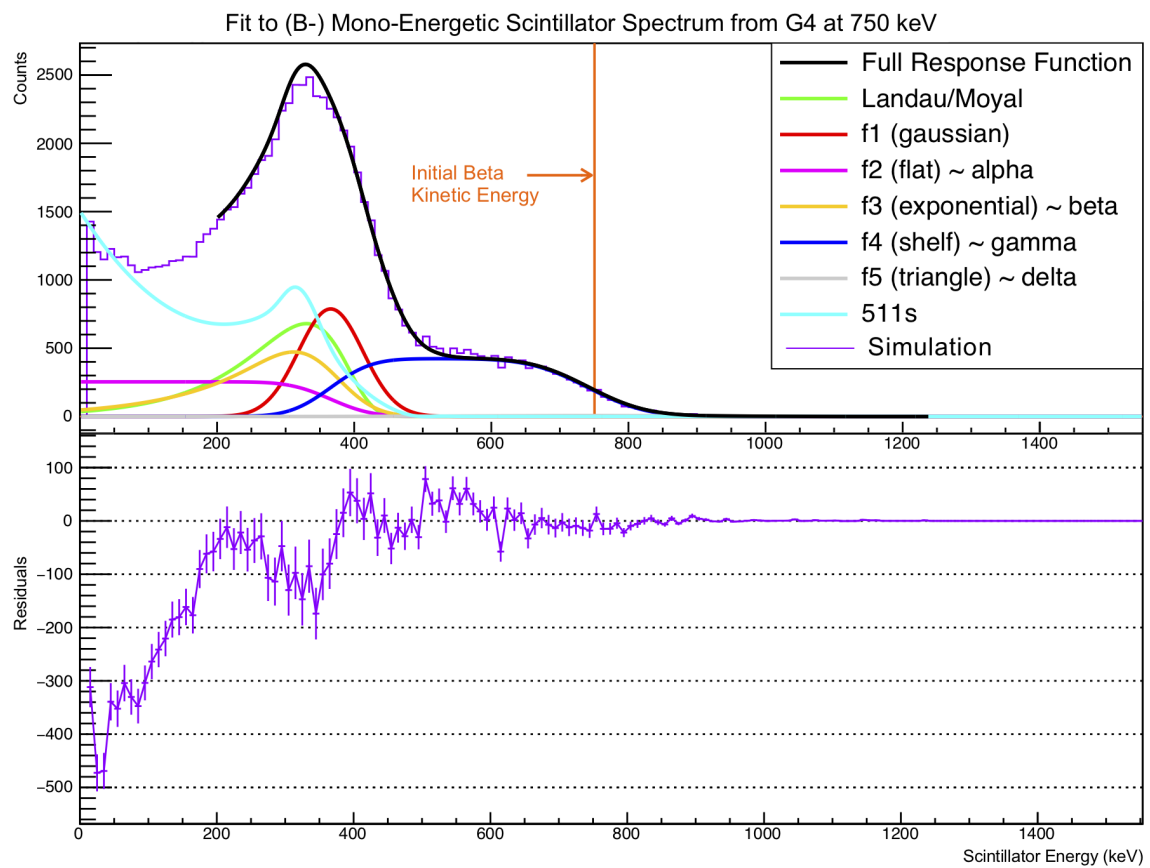


Figure 4.5: Fit to Mono-Energetic Spectrum, 750 keV (B-)

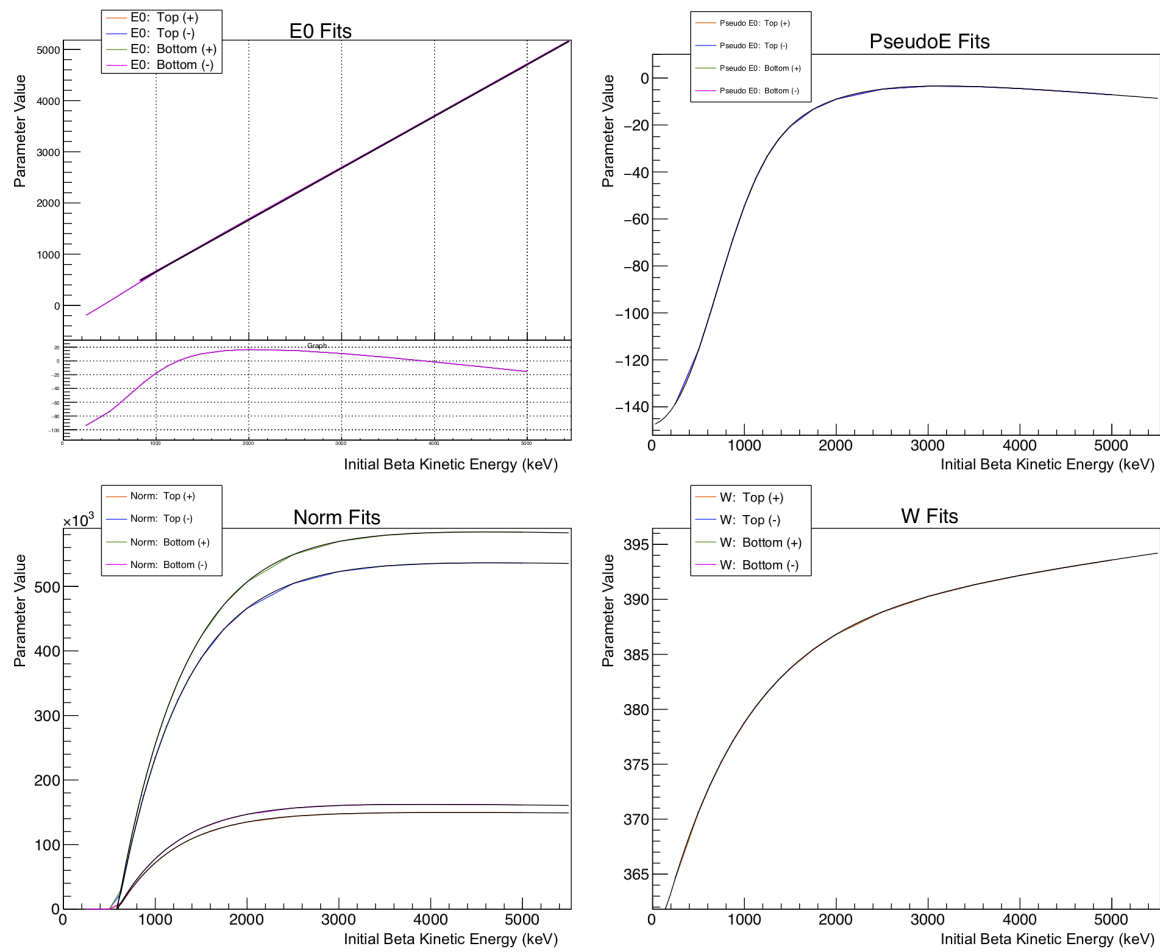


Figure 4.6: Lineshape Parameter Fits (Part 1)

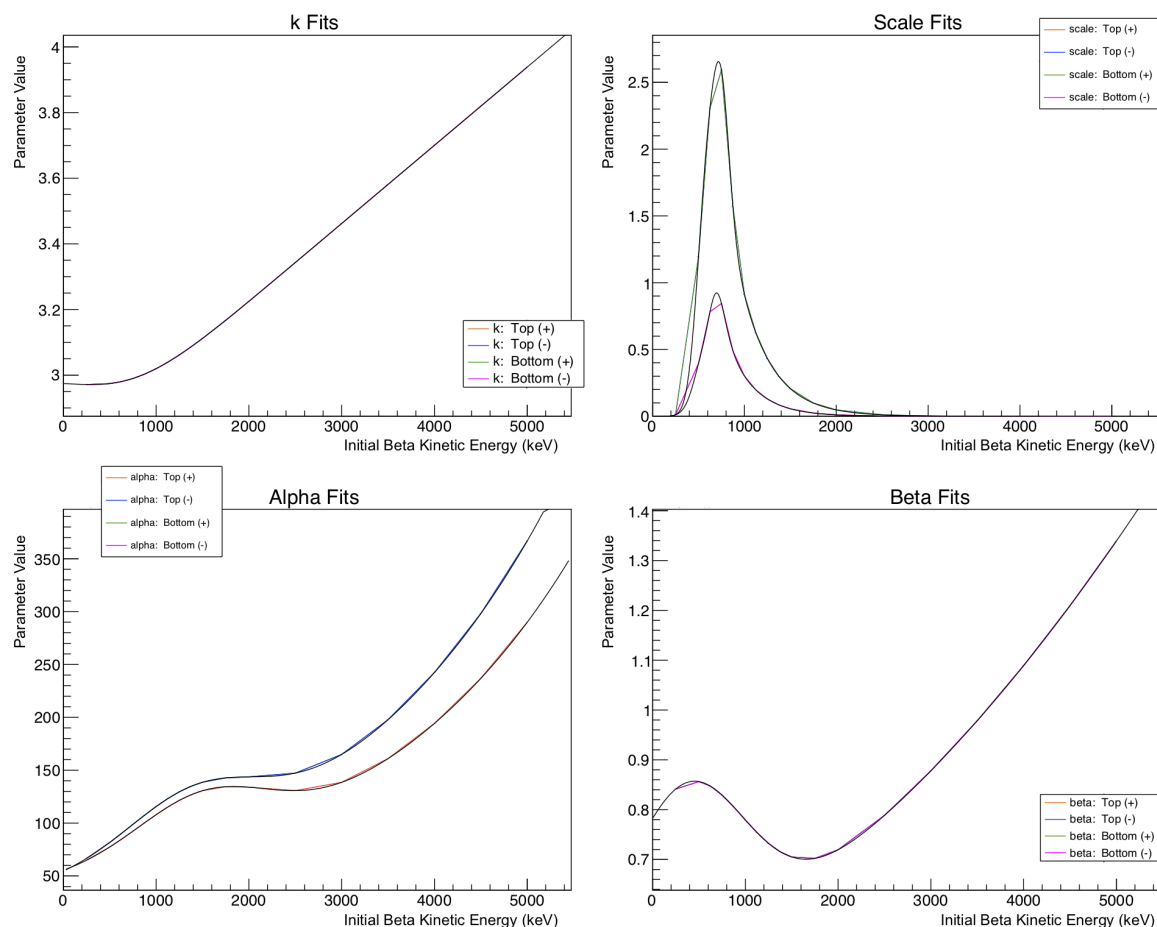


Figure 4.7: Lineshape Parameter Fits (Part 2)

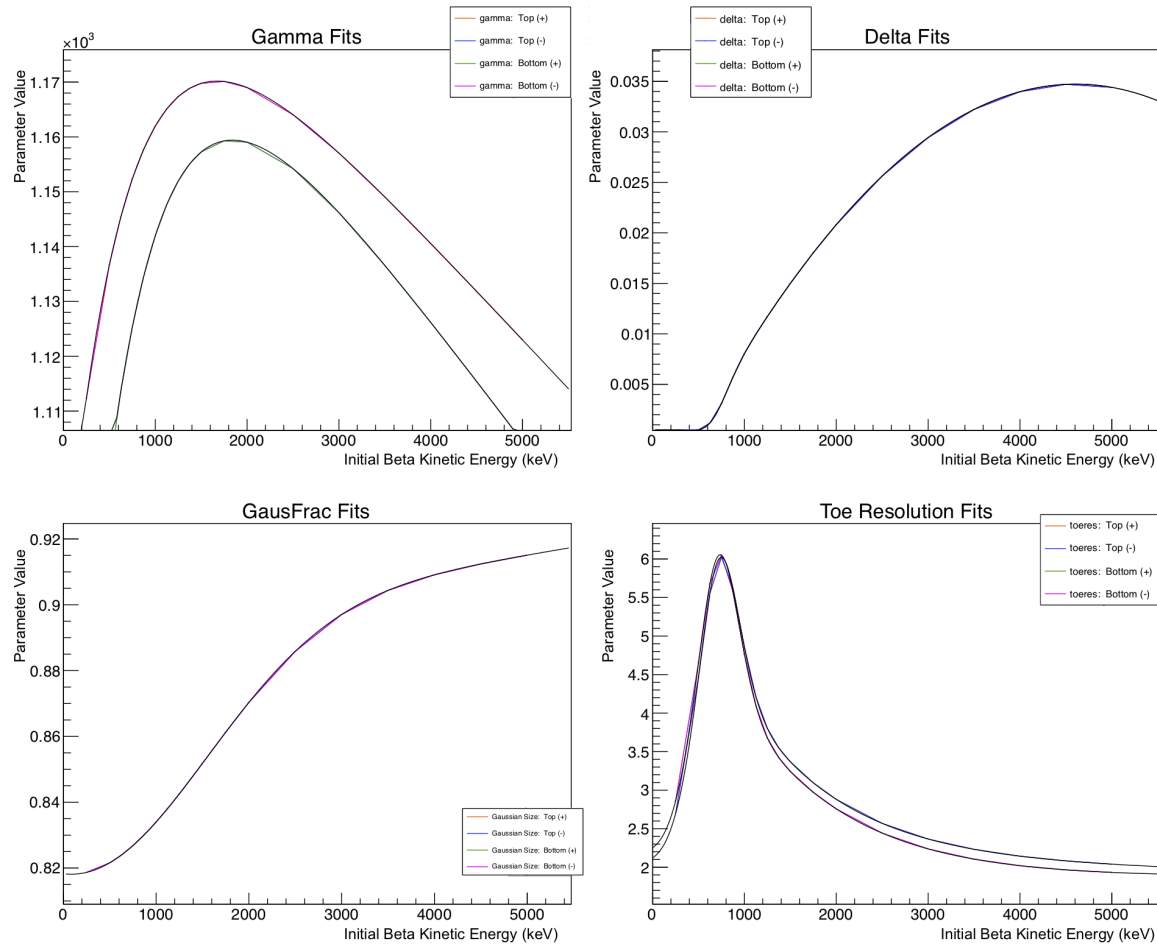


Figure 4.8: Lineshape Parameter Fits (Part 3)

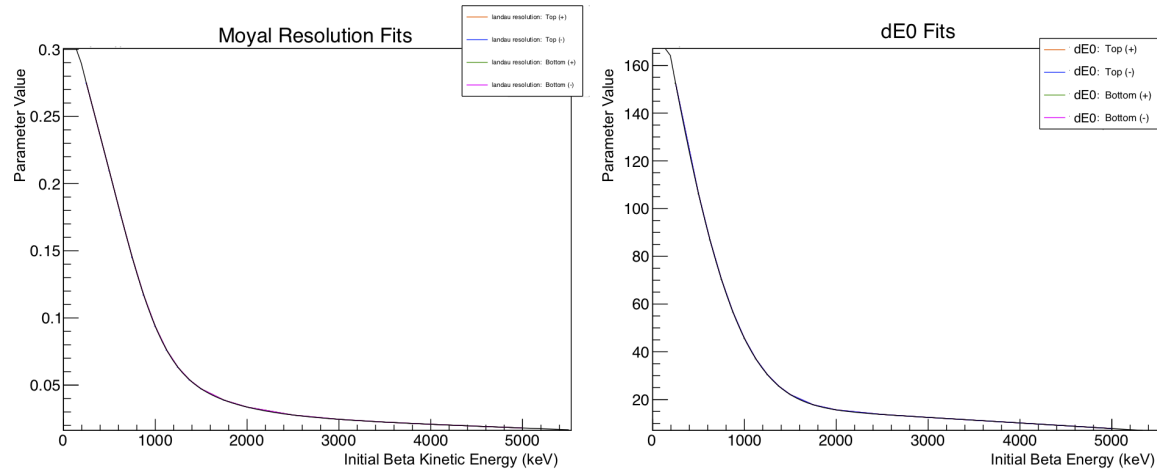


Figure 4.9: Lineshape Parameter Fits (Part 4)

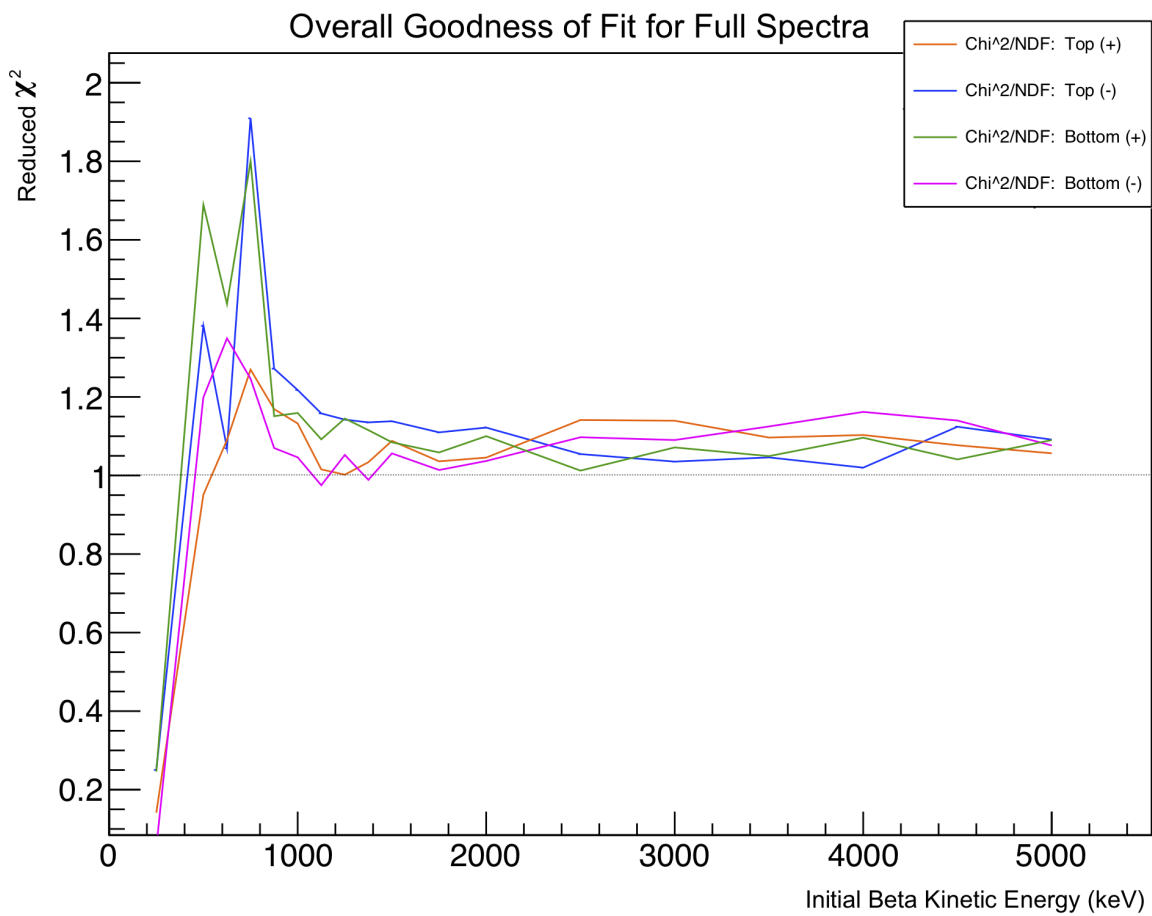


Figure 4.10: Goodness of fit for modeled response functions, for all four detector+polarization combinations. The models are clearly much better behaved at initial energies above  $\sim 1200$  keV.

## 4.4 Modeling the Scattering Effects from the Cloud

Beta scattering — in which a beta originating within the atom cloud is incident on a surface within the chamber and changes its trajectory, losing some of its energy in the process — is a significant systematic within this experiment, and it must be evaluated, quantified, and corrected for. While only a small fraction of events are affected, the process results in a change to the beta energy spectrum that can easily be misinterpreted as the exact signal we are searching for. It is therefore imperative that this be well understood.

The scattering process can result both in scenarios where a beta that was initially directed away from the detectors is scattered *into* a detector, and scenarios where a beta that was initially traveling towards a detector is scattered *away* from it. Since this is a polarized decay and the beta asymmetry is not zero, the relative likelihoods of each of these two scenarios depends on whether the nuclear polarization vector is directed toward- or away from the detector in question. In either case, it is clear that some events will be removed, and other events will be added in. As a further complication, betas that have been scattered into a detector will necessarily have a very different energy spectrum than unscattered betas, and neither are the betas that are scattered away from a detector removed uniformly from the original energy spectrum. With the four beta energy spectra comprising the essence of our observable, we must have a clear understanding of the results of this process within our data.

Despite these complications, it is clear that for events in which the beta is scattered from a surface prior to its incidence on a detector, the beta particle will take longer to travel from the position of its initial creation to the detector. Although it is not possible to fully separate scattered and non-scattered events from one another, a judicious choice of cut within the SOE-Beta TOF spectrum can still be used to lower the fraction of scattered events, improve our signal-to-noise ratio, and decrease the overall size of any systematic uncertainties associated with scattering.

It is useful to remember in the discussion that follows that a beta particle emerging from a nuclear decay is, in general, fairly energetic, with perhaps a few MeV of kinetic energy. In comparison, a shake-off-electron (“SOE” – see Chapter 1.5) typically has only a few eV of kinetic energy. As a result, within our experimental time-of-flight spectra, because it is not possible to observe the *true* time of decay, we have commonly used as a proxy the time at which a beta hit is detected. The betas are relativistic

and can be treated (for these purposes) as travelling at the speed of light – therefore if we suppose that all detected betas proceed from the position at which they were created directly into a detector, then the beta hit timestamp provides an excellent proxy for the true decay time, with only a small and easily calculable timing offset. Fig. ??, for example, is a spectrum of this sort for the shake-off-electrons’ “times of flight”.

Within this section, however, where the experimental SOE TOF spectra are examined in detail, the above assumption is insufficient, as it is necessary to consider effects from beta scattering – both to the observed beta energy spectra, and also to the observed beta time-of-flight spectra (which, of course, are only experimentally meaningful in comparison with another timed observation).

Using Geant4, a set of beta time-of-flight spectra is generated for decays originating from within the atom cloud for all four detector+polarization combinations, and it is clear that there is a small but non-negligible fraction of such events that arise from beta scattering events. Even within Geant4, where it is possible to measure the beta time of flight with respect to the initial time of decay, the scattered and unscattered spectra cannot be fully separated from one another. The strong correlation between emission angle and time-of-flight does, however, suggest that the signal-to-noise ratio could be improved by a judicious cut on the TOF spectra. In order to produce something which can be directly compared with experimental data, a TOF spectrum for SOEs must also be produced and merged with the beta TOF spectrum. Experimentally, this is done as an event-by-event subtraction, so that is also what must be done for the simulations. Unfortunately, these two time-of-flight spectra cannot easily be produced within a single type of simulation. Because scattering is an important effect within the beta time of flight spectra (and resulting beta energy spectra), Geant4 is the tool of choice for this type of particle. For shake-off electrons, which are emitted with little energy and accelerated through the electric field within the chamber, it is much more important to have an accurate model of the electric field and its effects on charged particles. The shake-off electrons’ time of flight is therefore evaluated by the TRINAT collaboration using COMSOL to track individual electrons through a model of the electric field within the experimental geometry.

The COMSOL SOEs were generated with starting positions taken from a 3D gaussian distribution near the chamber centre, with the precise position and size parameters taken from measurements using the rMCP, as in Table 3.3. They are

emitted with initial trajectories distributed isotropically. Three sets of SOE events are created: two with initial energies taken from the Levinger  $4S$  and  $3P$  spectra in the range of 0–100 eV, and the third with no initial kinetic energy. The origin of these SOE energy distributions is discussed in Section 1.5. A final simulated SOE TOF spectrum (relative to the time of decay) was produced as a linear combination of these spectra, comprised of 9% 0 eV events, 77%  $4S$  events, and 14%  $3P$  events. The relative contributions of each of these components arose from a comparison with experimental data, and the collaboration found that the distribution of hit positions on the eMCP was well modeled by Levinger’s formulae. There was only a very weak dependence on the relative number of SOEs removed from the  $4S$  and  $3P$  shells, though it turned out to be very important that the distributions not be truncated at too low an energy—a surprising result given the fact that both distributions are strongly peaked at much lower energies, and many of the higher energy SOEs are able to escape the central electric field region and therefore escape detection. The addition of the 0 eV events from  $^{37}\text{Ar}^-$  ions to the spectrum also greatly improved the fit.

With both a SOE TOF spectrum generated by COMSOL and a beta TOF spectrum generated by Geant4, the two spectra were combined event-by-event to produce a simulated “SOE – Beta” TOF spectrum to match the form of the data collected from the experiment. Note that although the simulated SOEs were generated from a model of the atom cloud, the betas generated by Geant4 were simply treated as originating from a pointlike distribution at the chamber centre. Since the betas are relativistic and the cloud is small, any changes to the beta spectrum as a result of this model would be too small to be seen given the timing resolution of our detectors ( $\sim 0.1$  ns).

This “SOE – Beta” spectrum is convoluted with a gaussian of width  $\sigma = 0.443$  ns to model the timing jitter within our detectors. The width of this gaussian is taken from a measurement of the “prompt” peak (betas incident on the eMCP before scattering into a scintillator) within the equivalent experimental spectrum. Results for Levinger SOEs and 0 eV SOEs are shown in Fig. 4.11.

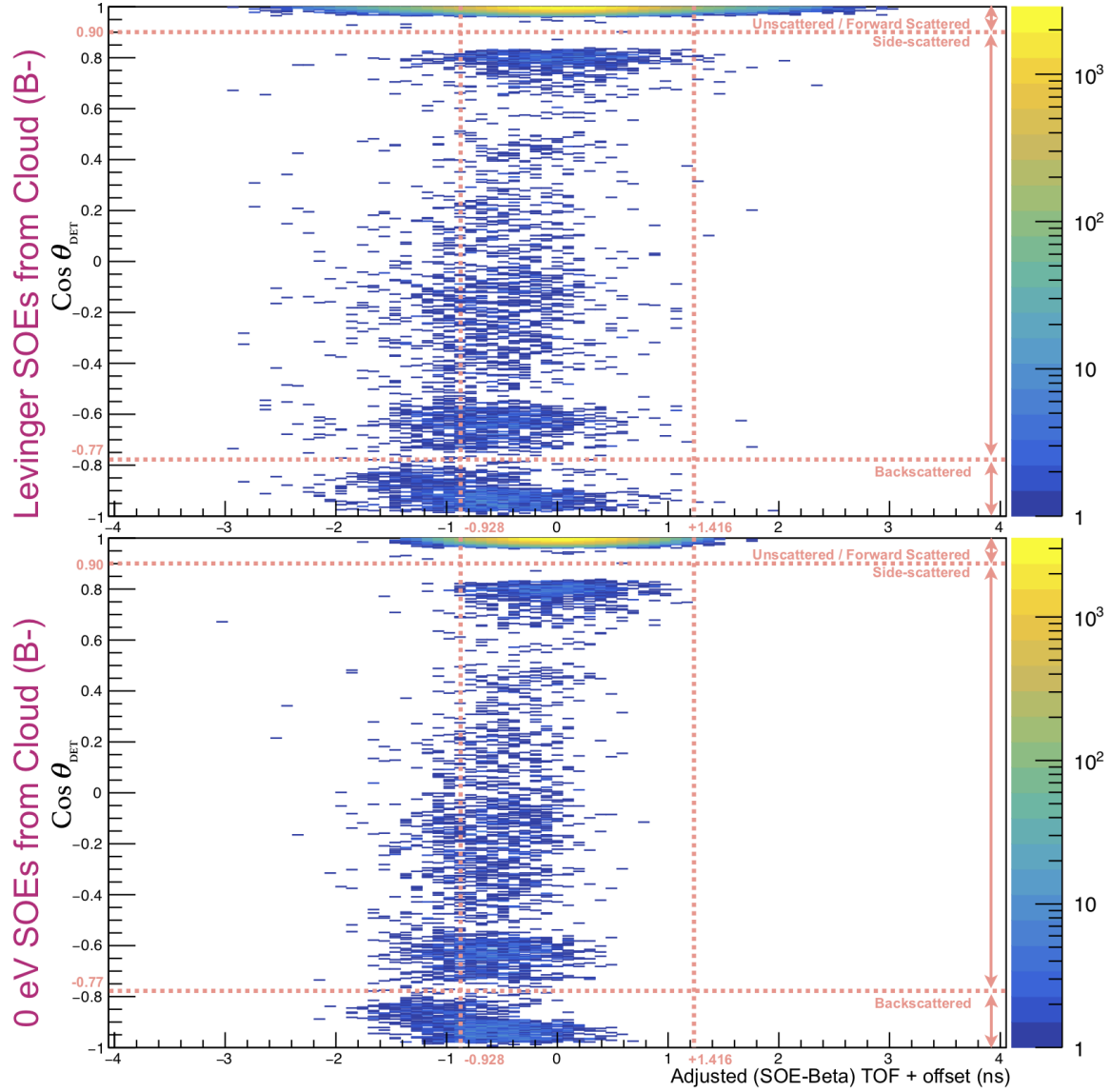


Figure 4.11: Simulated Beta emission angle with respect to the detector in which the event is eventually observed(G4), plotted versus an adjusted SOE – Beta TOF (COMSOL, G4). SOEs are simulated with initial energy distributions adapted from Levinger (top), and with no kinetic energy at all (bottom). The TOF cut that will eventually be taken is shown, and events are classified into scattering categories for later evaluation as a systematic (see Ch. 5.2.1).

## 4.5 Simulating the Background and Time of Flight

One of the largest sources of background events in this experiment is from decaying  $^{37}\text{K}$  atoms that have escaped from the trap and become stuck on the other surfaces

within the chamber. The majority of these events can be eliminated simply by taking a time-of-flight cut on the eMCP relative to a scintillator hit time (as described in Section 3.8). Unfortunately, this procedure cannot remove the entirety of the background, so what remains—both background events from chamber surfaces, and events from the atom cloud itself—must be modeled and understood.

The model used for events originating from the atom cloud is described in Section 4.4, and this section will discuss events originating from other surfaces within the chamber. The methodology used is very similar.

Spectra for both the beta time of flight and shake-off electron time of flight (calculated with respect to the time of decay) were generated, using Geant4 and COMSOL, respectively. For these background events, the SOE and beta were both generated to originate on certain surfaces within the experimental chamber. Because the surfaces from which generated SOEs had a viable path through the electric field onto the eMCP is relatively large, the SOE and beta spectrum must be generated, event-by-event, to originate at the same position. This procedure not only allows us to account for differing beta times of flight resulting from different distances to either detector, it also captures the differing energy loss from scattering for observed betas originating at different positions.

To model the distribution of atoms stuck to surfaces within the chamber, we suppose that all escaped atoms were lost from the central cloud in an isotropic manner, so that the number of atoms on an object’s (infinitesimal) surface element is given by the (infinitesimal) solid angle spanned by it. This principle is used both to normalize the relative number of decay events between different surfaces, and also to produce the distribution of events on a given surface. Then, for each surface of interest to us, a set of Geant4 beta decay events are generated from starting points on that surface, with those starting points distributed as described above. The beta particles are tracked through the geometry, and only events in which a beta is incident on a scintillator are saved.

For Geant4 events in which a scintillator hit is recorded, these events’ start positions are then fed into COMSOL and used as start positions for SOE events, generated by the collaboration with the same energy spectrum that was used for events from within the cloud, as described in Sec. 4.4. For these events, only the ones in which an SOE was incident on the eMCP were preserved. An event-by-event subtraction is then performed on the timing results of the Geant4 and COMSOL Monte Carlo

spectra, such that for every event that is preserved, the SOE in COMSOL and the beta in Geant4 will have originated from the same starting position. The results are then convoluted with a  $\sigma = 0.443\text{ ns}$  width gaussian to model timing jitter, as in the case of events originating from the cloud (Sec. 4.4).

With a simulated “SOE – Beta” TOF spectrum to compare with experimental data, it is possible to estimate how many such events remain (and what their energy distribution looks like) after a cut on the experimental spectrum is performed. The results are shown in Fig. 4.12. An upper limit for the fraction of events generated this way can be estimated by assuming that all losses from the cloud not attributable to radioactive decay must emerge isotropically and then stick to whatever object is in its path. This method overestimates the amount of background by around a factor of 2.

In order to check this model’s performance, the energy-averaged superratio asymmetry is assembled for each time-of-flight bin within both our simulated and experimental spectra, as in Fig. 4.13. The modeled background is treated as being unpolarized. Although the two plots diverge rapidly outside this TOF range, an evaluation of the  $\chi^2$  statistic within this range produces a suspiciously good result.

### SOE TOF, Both Detectors (400 - 5000 keV)

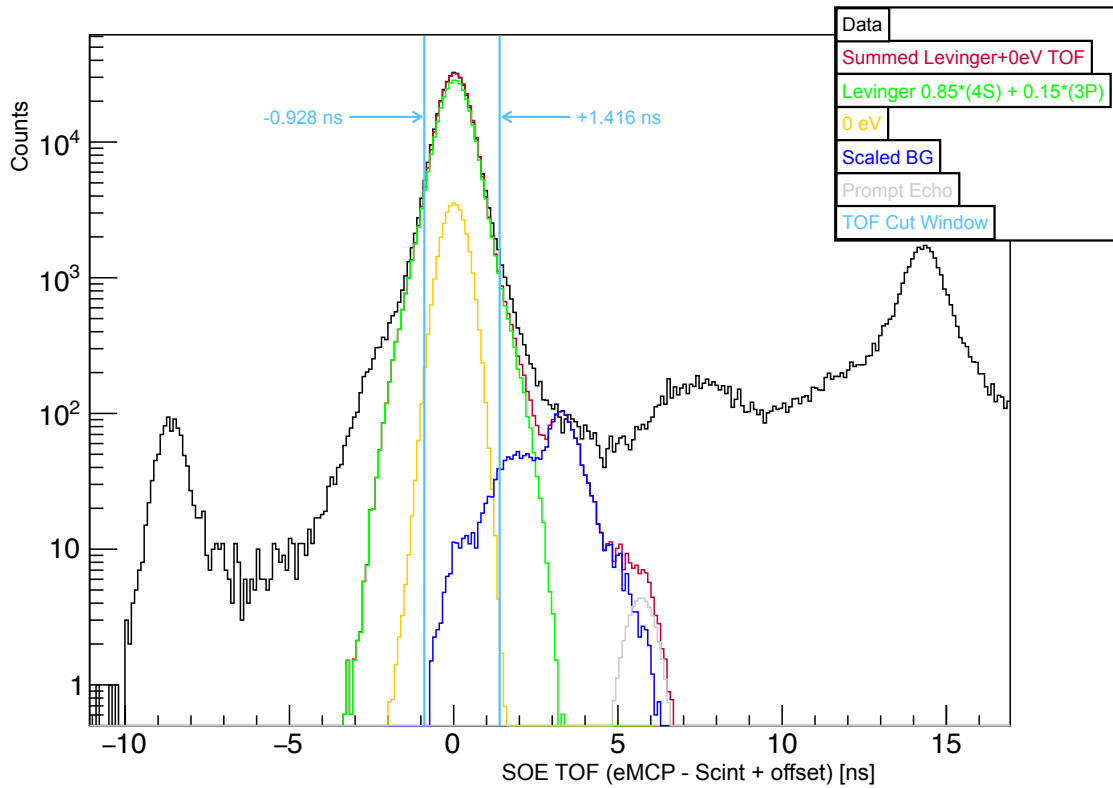


Figure 4.12: (SOE–Beta) TOF, with both model and experimental data shown. Spectra from simulations are separated according to their source, and the final TOF cut is drawn on. The background spectra have been scaled down by about a factor of 2 from their estimated maximum in order to match experimental data. Similar quality results are achieved no matter how the Levinger SOEs are distributed between 4S and 3P orbital shells, however adding the 0 eV electrons to the spectrum produces a large improvement to the agreement between the model and experiment.

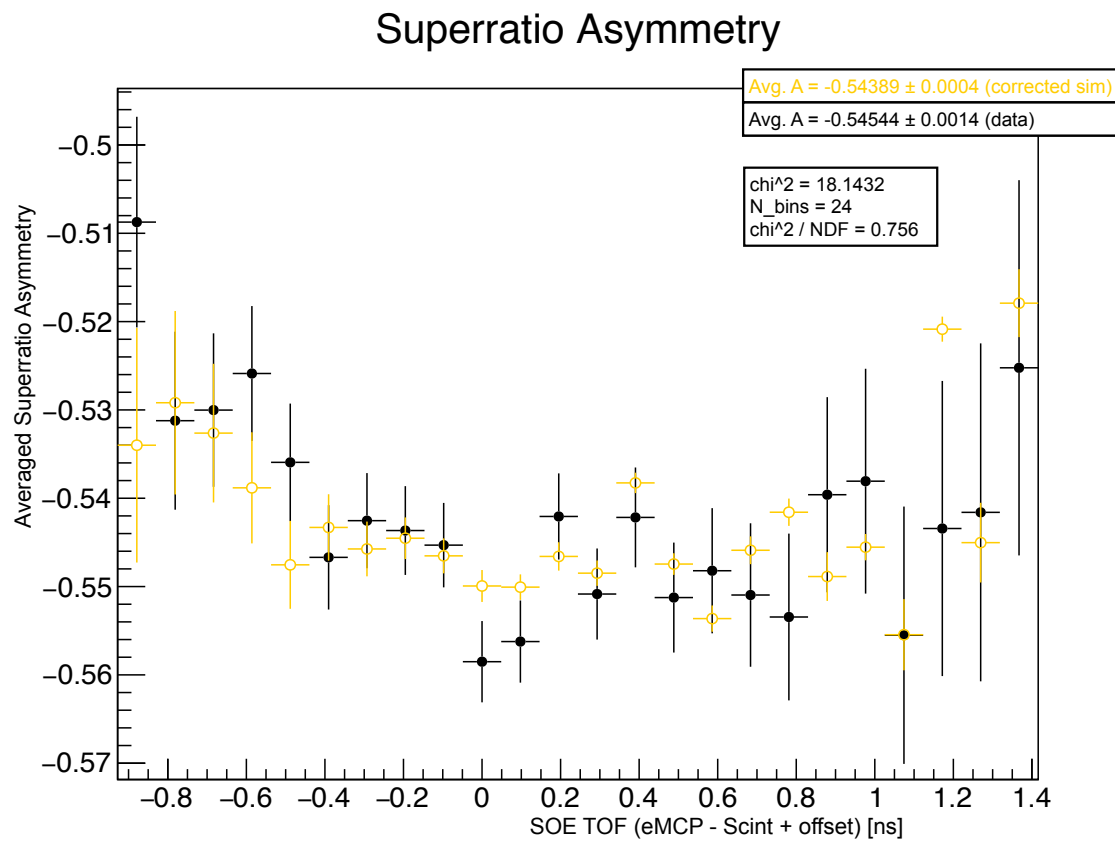


Figure 4.13: The superratio asymmetry, averaged over all scintillator energies between 400-4800 keV, is used to compare the experimental data and simulated TOF model as a proxy for the quality of the model to estimate the background. Background events are treated as being entirely unpolarized. All other cuts have been applied.

# Chapter 5

## Analysis and Estimates of Systematic Effects

The collaboration has performed an independent analysis using (mostly) the same set of data to measure  $A_\beta$ , fixing  $b_{\text{Fierz}}$  to zero. Differences with that analysis are interleaved in this section and summarized in Appendix A. Critical physics improvements concern an eMCP-beta timing walk correction which enabled an improved cut against background, also incorporating a more complete modelling of decay backgrounds from untrapped atoms. Technical corrections include a correct treatment of the polarization cycle. An arbitrary change in the DSSD radius cut is kept self-consistent.

### 5.1 Comparing Simulations to Experimental Data: The General Methodology

The primary parameter measurement strategy in this project involved comparing the experimental data to a 2D parameter space of simulations, and this is true both for evaluation of the best parameter values, and also for evaluations of the uncertainties.

As described in Section 1.6, and in more detail in Appendix D, the primary experimental observable is the superratio asymmetry, which is constructed from four experimental *rates* of beta detection:

$$A_{\text{super}}(E_\beta) = \frac{\sqrt{r_{T-} r_{B+}} - \sqrt{r_{T+} r_{B-}}}{\sqrt{r_{T-} r_{B+}} + \sqrt{r_{T+} r_{B-}}}. \quad (5.1)$$

This quantity is closely related to the two fundamental parameters we hope to extract, and in the absence of certain systematic effects, we can cleanly describe a relationship between the observable and the two physical parameters ( $A_\beta$  and  $b_{\text{Fierz}}$ ) that we might use to describe the shape of an experimentally measured  $A_{\text{super}}(E_\beta)$  curve:

$$A_{\text{super}}(E_\beta) = \frac{A_\beta \frac{v}{c} |\vec{P}| \langle |\cos \theta| \rangle}{1 + b_{\text{Fierz}} \frac{mc^2}{E_\beta}}. \quad (5.2)$$

Of course, when all systematics are properly accounted for, Eq. 5.2 is no longer an adequate description of the full relationship between the observable and physical parameters and a comparison to monte carlo must be used. A series of Geant4 simulations are performed and the results are (re-)processed with slightly different cuts and calibrations so as to match with the experimental conditions in each of the three electron datasets, and the superratio asymmetries are constructed. The degree to which the simulations and experiment match is evaluated by using a  $\chi^2$  comparison of the superratio asymmetries as the figure of merit (see Figs. 5.1,5.2,5.3). This is repeated for a range of  $A_\beta$  and  $b_{\text{Fierz}}$  values, and a  $\chi^2$  mapping of the 2D parameter space is produced.

For each superratio asymmetry constructed from simulated spectra, the scintillator spectra from which the superratio asymmetry is comprised are created as a linear combination of Geant4 beta decay events originating from the atom cloud and from surfaces within the chamber. Both components of the spectra are combined event-by-event with SOE events generated in COMSOL, as described in Sections 4.4 and 4.5, as this is necessary for the critical time-of-flight cut on the “SOE – Beta” spectra. For decays originating within the atom cloud, both the primary decay branch and the subdominant ‘two percent’ branch are allowed to contribute events, and only the dominant branch is varied as a function of BSM couplings. For background events, only the Standard Model primary branch is simulated.

A major caveat to the above description is that running a high statistics G4 simulation of our experiment is a computationally expensive process, so it was not possible to perform a separate simulation at every ‘pixel’ within the parameter space. Instead, to evaluate how well the experimental data matched to the expectation for varying values of  $A_\beta$  and  $b_{\text{Fierz}}$ , only three simulations were performed for different values of  $b_{\text{Fierz}}$ , all using the same nominal value for  $A_\beta$ . The  $A_{\text{super}}(E_\beta)$  spectra representing

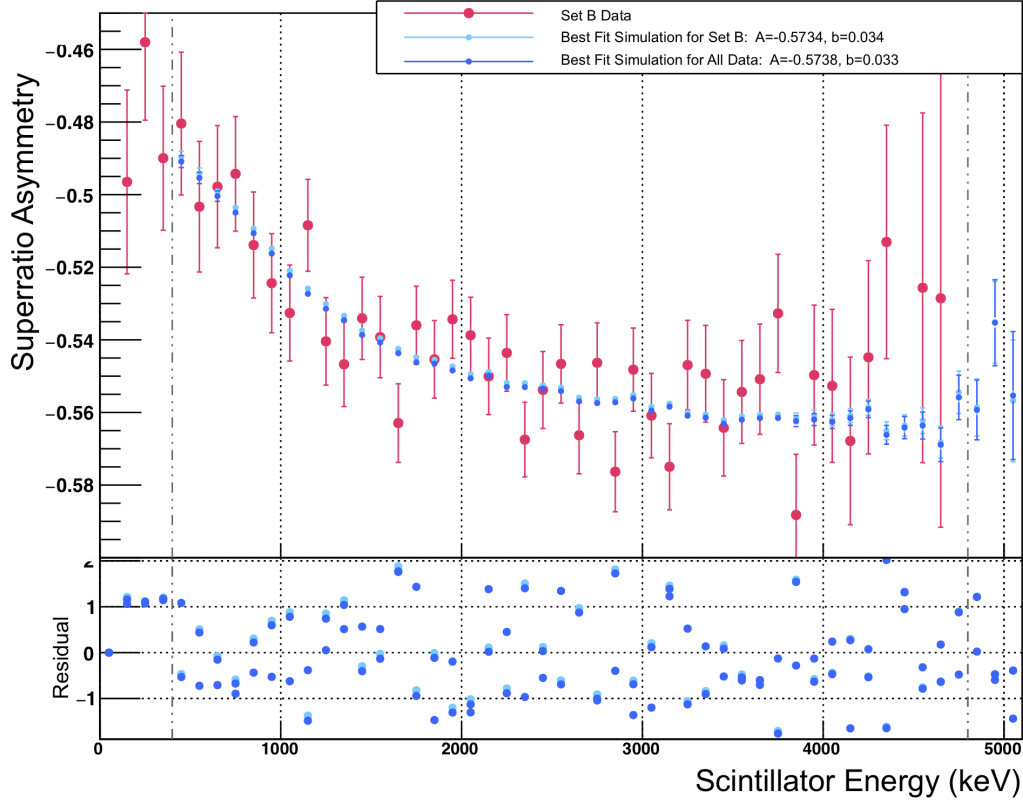


Figure 5.1: A superratio asymmetry from Dataset B, and the best fits from simulations.

intermediate  $b_{\text{Fierz}}$  values were created from a linear combination of spectra generated at the two closest values of  $b_{\text{Fierz}}$ .

To vary the effective  $A_\beta$  value, the generated  $A_{\text{super}}(E_\beta)$  spectrum was simply scaled. From Eq. 5.2 it is clear that this works well so long as  $b_{\text{Fierz}}$  is small and any systematics are evaluated separately. This method allows for an arbitrarily finely pixellated 2D  $\chi^2$  map to be created. It is done separately for each of the three experimental data sets so as to facilitate evaluation of systematic effects that changed between runsets. See Figs. 5.4, 5.5, 5.6.

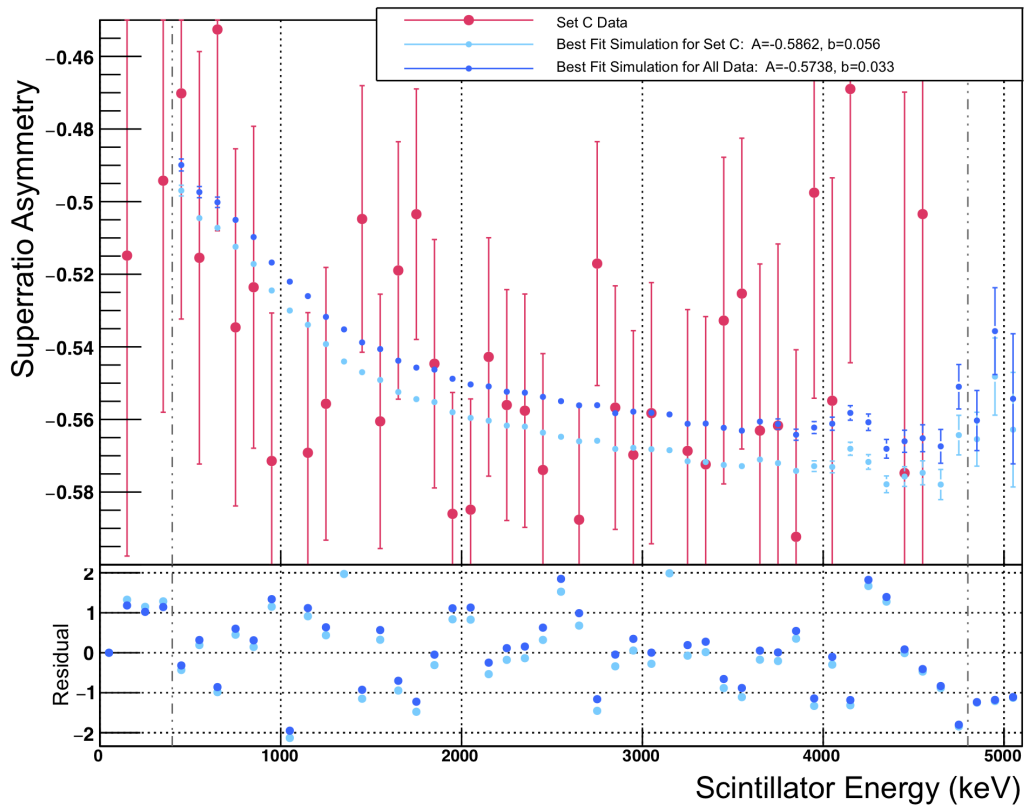


Figure 5.2: A superratio asymmetry from Dataset C, and the best fits from simulations.

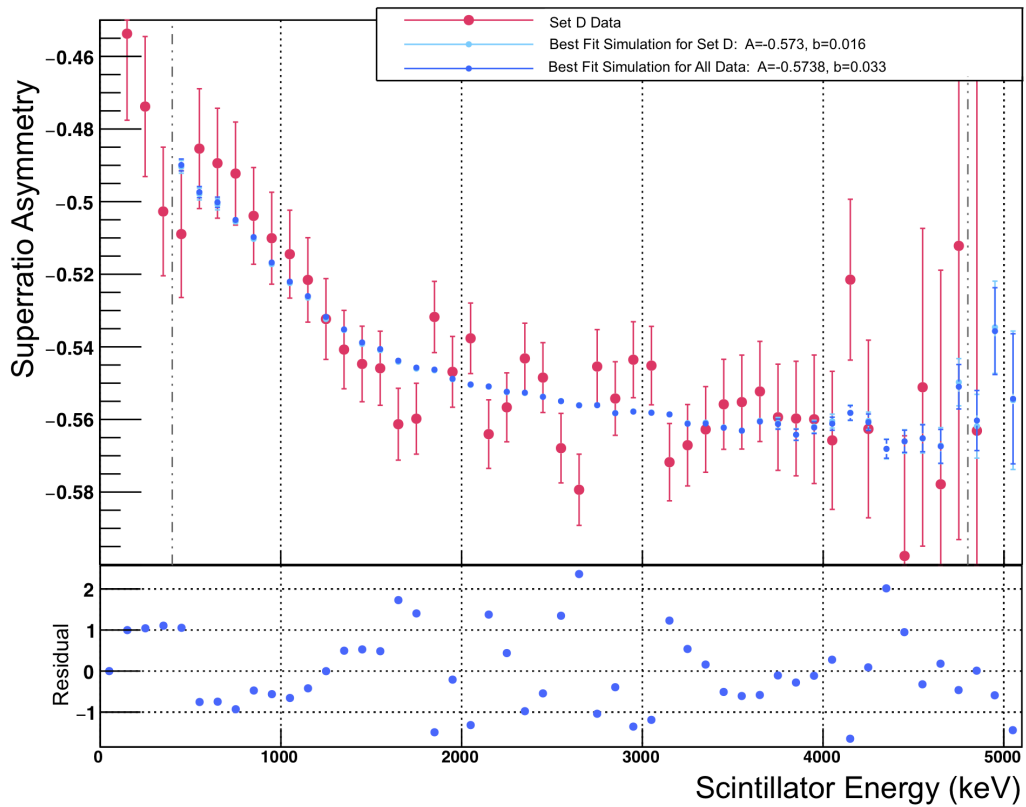


Figure 5.3: A superratio asymmetry from Dataset D, and the best fits from simulations.

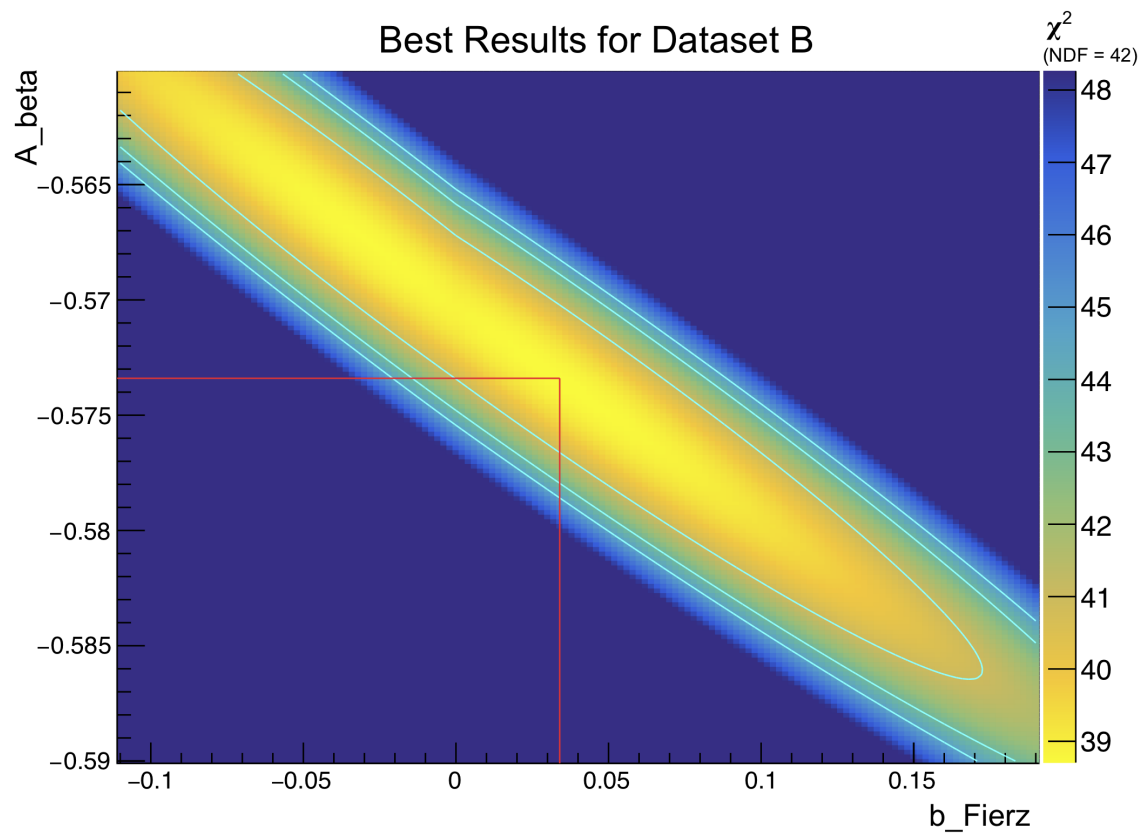


Figure 5.4: A  $\chi^2$  map to compare data from Runset B to a parameter space of  $A_\beta$  and  $b_{\text{Fierz}}$  values.

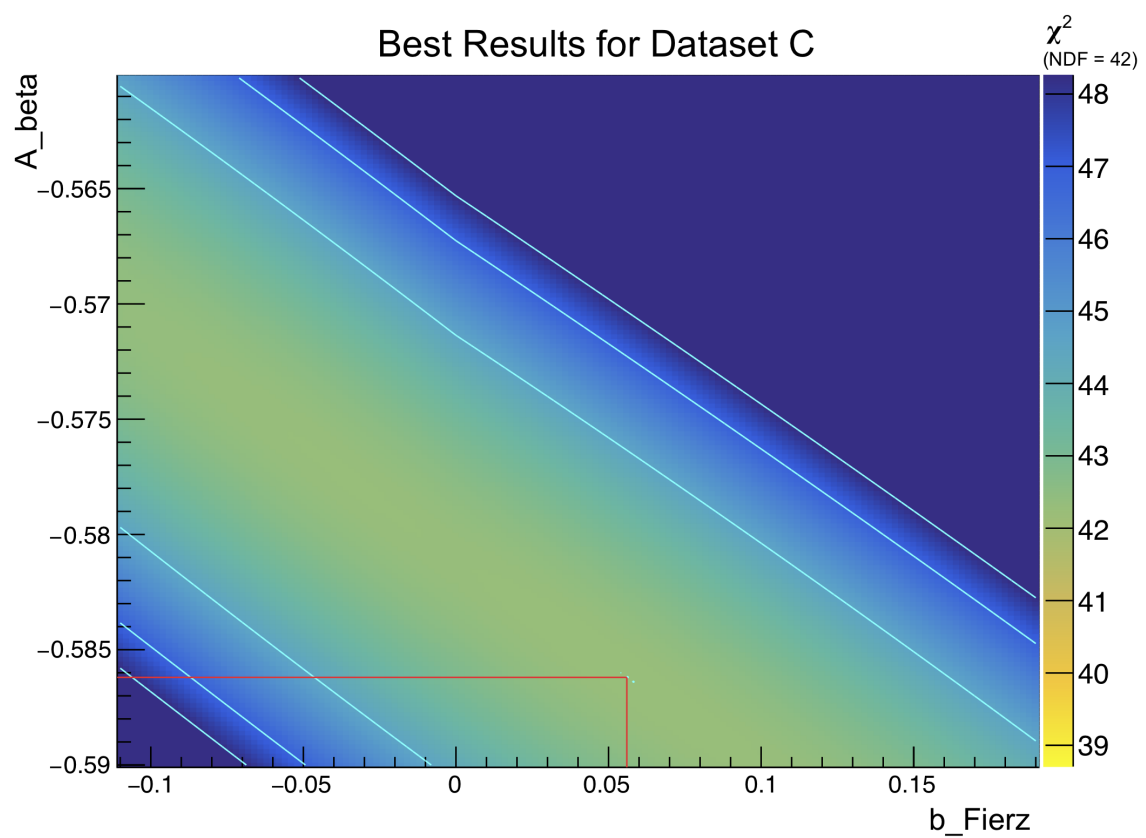


Figure 5.5: A  $\chi^2$  map to compare data from Runset C to a parameter space of  $A_\beta$  and  $b_{\text{Fierz}}$  values.

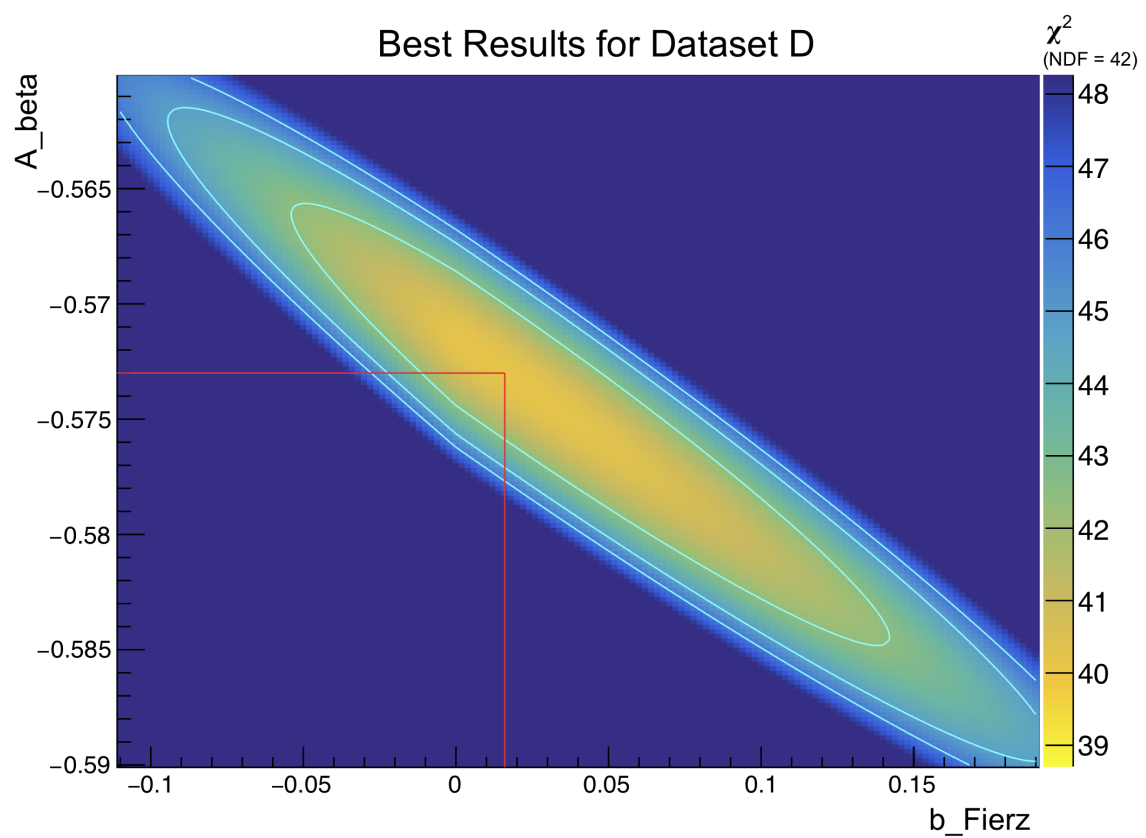


Figure 5.6: A  $\chi^2$  map to compare data from Runset D to a parameter space of  $A_\beta$  and  $b_{\text{Fierz}}$  values.

## 5.2 Evaluation of Systematic Effects

### 5.2.1 Beta Scattering

The methodology used to simulate and model scattered events is described in Section 4.4. To evaluate the systematic effect on the final measurements arising from incomplete knowledge of how much beta scattering is present (i.e., how well we can trust the simulation to correctly model the amount of scattering), two sets of  $\chi^2$  maps very much like those in Section 5.1 are created, with the amount of scattering varied by one standard deviation. This does not require a new simulation; instead, for the three high statistics G4 simulations varying the BSM scalar coupling, all events passing the cuts are categorized into ‘unscattered and forward-scattered’ events, ‘sidescattered’ events, and ‘backscattered’ events, depending on a comparison of the beta’s emission angle to the detector in which it was eventually observed, as shown in Fig. 4.11.

The contribution from unscattered and forward scattered events is not allowed to vary, but the weights attributed to sidescattered and backscattered events was varied by  $\pm 10\%$  and  $\pm 5.1\%$  (respectively) relative to their ‘best’ values. Fig. 5.7 clearly shows the change in superratio asymmetry produced by this variation in the amount of scattering. The method by which it was determined how much the scattering weights should be allowed to vary is described in the supplementary material of a recent publication by the collaboration [19]. Since errors in evaluating both side-scatter and backscatter arise from limitations on how well Geant4 is expected to perform, it is not clear how correlated these errors are, but it seems foolish to suppose they should not be correlated at all. Therefore, the conservative assumption that the two are *fully* correlated is taken, and the errors from side-scatter and backscatter are added *linearly* to one another before being combined in quadrature with the other uncertainties.

As this is the dominant systematic error, the TRINAT collaboration is working to improve the experimental design to use lower-Z materials to reduce the size of this effect.

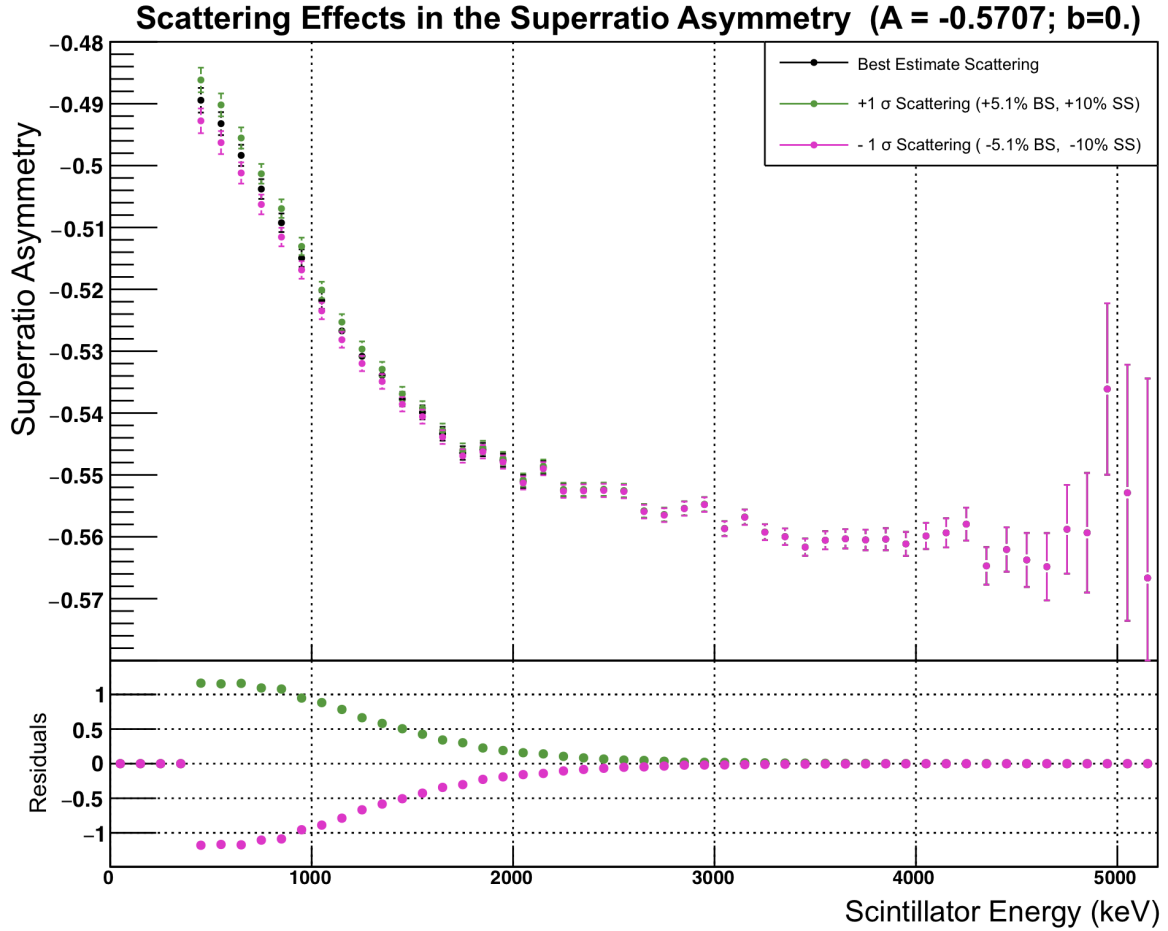


Figure 5.7: The amount of scattering is adjusted by one standard deviation in both directions, and the results to the superratio asymmetry are plotted. The bulk of the effect occurs at lower energies, where sensitivity to  $b_{\text{Fierz}}$  is at its highest.

### 5.2.2 Detector Calibrations and Thresholds

#### Scintillators

The two plastic scintillators were calibrated by the collaboration using online data, with reference points from the beta spectrum endpoint and the compton edge arising from annihilation radiation. Calibration was performed using only *polarized* data, because the final measurements use only polarized data, and the scintillator gain is more stable in the absence of the stronger oscillating magnetic fields from the AC-MOT.

A linear calibration is used, with

$$E_{\text{scint}} = \frac{1}{m}(Q_{\text{QDC}} - b), \quad (5.3)$$

and the detector resolution arising from photon counting statistics is given by

$$\sigma = \sqrt{\lambda E_{\text{scint}}}. \quad (5.4)$$

During online data collection, one QDC module failed abruptly and had to be replaced. As a result, the collected data is calibrated separately before and after the module failure, and the calibrations change slightly at this time. The methodology used is described in detail within [21], so the results will simply be stated here in Table 5.1.

Runsets		b	m	$\lambda$
EA, EB	RA, RB	Top	$110.0 \pm 0.3$	$0.3985 \pm 0.0004$
		Bottom	$142.0 \pm 0.3$	$0.4234 \pm 0.0004$
EC, ED	RC, RD, RE	Top	$110.7 \pm 0.2$	$0.3883 \pm 0.0004$
		Bottom	$143.0 \pm 0.3$	$0.4132 \pm 0.0004$

Table 5.1: Scintillator Calibrations

To evaluate the systematic effects associated with the scintillators' calibrations, the calibration for each scintillator is adjusted independently to produce energy measurements that are higher by one standard deviation, and lower by one standard deviation, and the resulting changes to the  $\chi^2$  map's  $A_\beta$  and  $b_{\text{Fierz}}$  centroids is measured. For this, the datasets corresponding to both sets of calibration numbers have their calibrations adjusted simultaneously, but each individual scintillator is treated separately. There is no reason to think the two scintillators' calibration accuracies should be correlated, so errors resulting from a changed scintillator calibration are added to one another in quadrature.

### DSSD Radius, Energy Threshold, Agreement

Several parameters relating to our choice of cuts relating to DSSD calibrations are varied within both the experimental data and the simulated data to which it is compared. The detection radius, the overall energy threshold, the strip-by-strip SNR,

and the energy and timing agreement (See Ch. 3.6) are each adjusted separately at the start of data processing, and the changes are propagated through to a final  $\chi^2$  map.

The changes to measured values of  $b_{\text{Fierz}}$  and  $A_\beta$  from these adjustments are comparatively small, and the errors are believed to be uncorrelated, so they are added in quadrature to the total systematic uncertainty.

### 5.2.3 The Atomic Cloud

Uncertainties relating to the position, size, motion, and expansion of the atomic cloud are evaluated using the response function, which is implemented as described in Ch. 4.3. To evaluate how well the simple monte carlo + response function (SMC+RF) performs in evaluating uncertainties, the relationship between how the SMC+RF and the full G4 simulation changes when a BSM parameter is adjusted is considered in Fig. 5.8.

To evaluate the propagated systematic effects arising from our knowledge of the cloud position, the simple monte carlo is used to generate events originating at points chosen randomly from the distributions produced by linear interpolation of the parameters in Table 3.3, with each parameter describing the distribution allowed to vary in accordance with its stated uncertainty, assuming gaussian-distributed errors. The results for each of the three datasets are shown in Fig. 5.9 for  $A_\beta$  and Fig. 5.10 for  $b_{\text{Fierz}}$ .

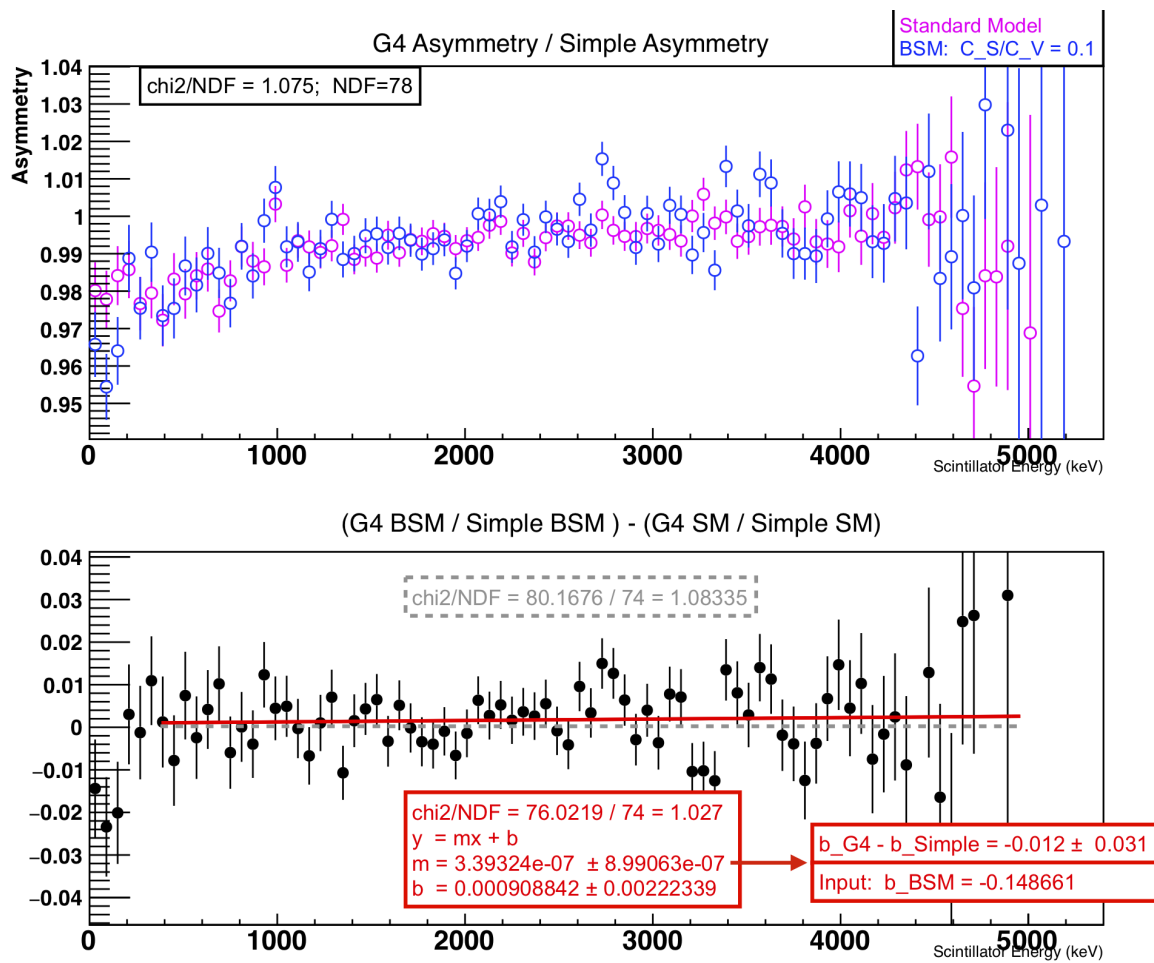


Figure 5.8: Superratio asymmetries generated by G4 and SMC+RF are compared against one another for a change in BSM parameters. The results show a consistent behaviour when the value of  $b_{\text{Fierz}}$  is adjusted, suggesting that the SMC+RF can safely be used to evaluate systematic effects such as those arising from a change in cloud position.

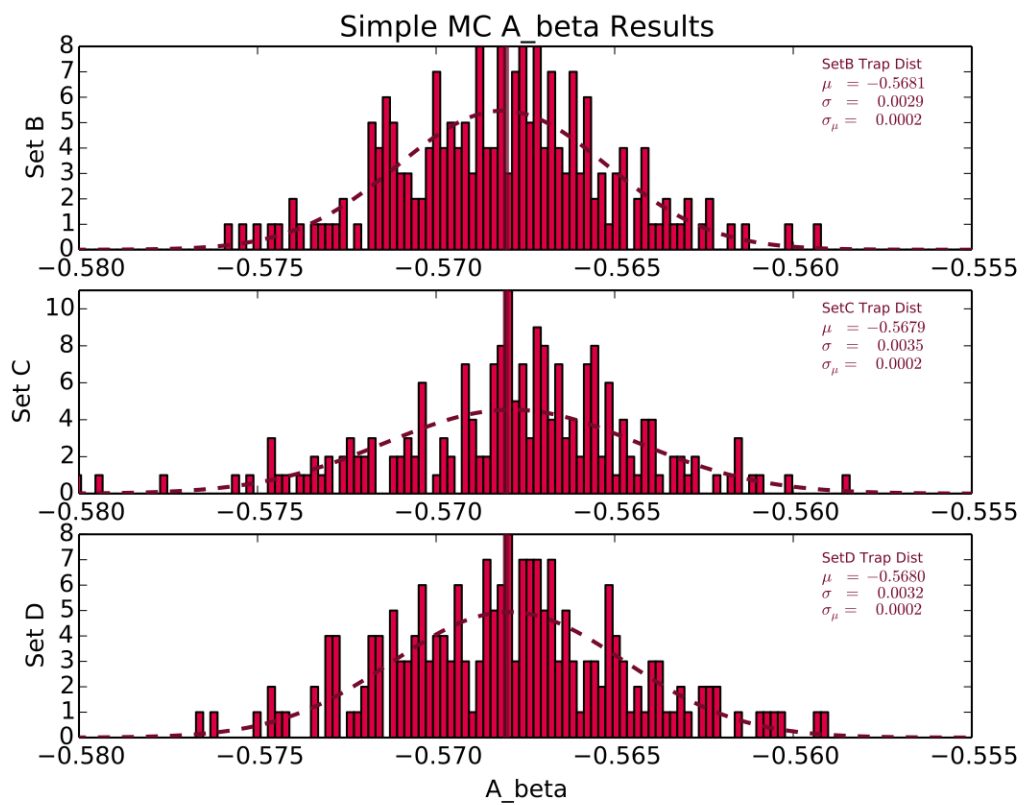


Figure 5.9: Estimated offset and uncertainty in  $A_\beta$  resulting from an imperfectly centred cloud of finite size, and the uncertainty and variation within these parameters. Evaluated by using the SMC+RF method.

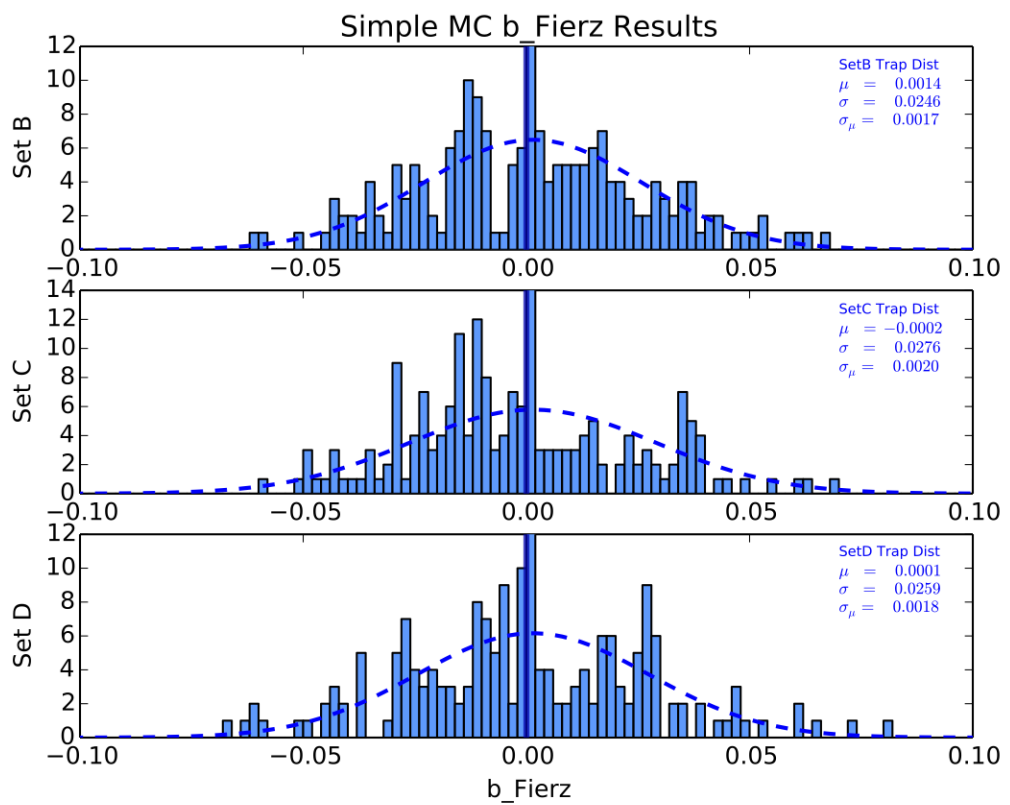


Figure 5.10: Estimated offset and uncertainty in  $b_{\text{Fierz}}$  resulting from an imperfectly centred cloud of finite size, and the uncertainty and variation within these parameters. Evaluated by using the SMC+RF method.

### 5.2.4 The Response Function’s Low Energy Tail

This subsection has the collaboration’s evaluation of the uncertainty from the scintillator detector’s lineshape tail. The energy from a monoenergetic beta is not always fully absorbed in a plastic scintillator. Although most backscattered betas are vetoed by the DSSD, some produce bremsstrahlung photons, and these frequently escape low-Z plastic scintillator— all cross-sections are known to high accuracy, but there is always uncertainty entailed in the MC implementation. This lineshape tail will then effectively move events from higher to lower measured energy, artificially altering the lower-energy asymmetries and mimicking the effects of a Fierz term.

Since this detector effect is difficult to disentangle from the other scattering effects off volumes, the collaboration adds a linear function down to zero for the tail to a Gaussian for the peak, with linewidth varying by photon statistics [23]. The convolution of this simple detector response function with v/c then scales the centroid MC, with the lineshape tail varied by  $\pm 10\%$  of its value, a generic uncertainty accepted by the community for MC electromagnetic simulations. The fit  $b_{\text{Fierz}}$  centroid changes by  $\pm 0.0076$ , summarized as the 0.008 “Low Energy Tail” in the systematics table at the start of this chapter. When compared with other uncertainties of the present data set, this is small enough that the accuracy of this estimate is adequate.

### 5.2.5 Background Events

Modeling of background events is covered comprehensively in Ch. 4.5. Because the background model doesn’t fully fit the experimental TOF spectrum, a relatively large variation in the number of background events is considered. The background spectrum is scaled from its nominal size up by a factor of 2 and down by a factor of 2.

Since the background has been reduced greatly by the improved time-of-flight analysis, this even this large variation in the number of background events makes a relatively small contribution to the final result.

### 5.2.6 Material Thicknesses

There are three distinct objects a beta emitted from the central atom cloud must pass through before arriving at a scintillator: a  $(275 \pm 6)\mu\text{m}$  silicon carbide mirror,

a  $(229 \pm 23)\mu\text{m}$  beryllium foil, and a  $(295 \pm 5)\mu\text{m}$  double-sided silicon strip detector, as shown in Fig. 2.5.

The propagated uncertainties are treated as uncorrelated (added in quadrature), and evaluated by running high-statistics Geant4 simulations with a parameter adjusted, then propagating the result through the analysis pipeline to compare against superratio asymmetries constructed to span the 2D BSM parameter space. Because of the processor time required for this, certain simplifying assumptions were used to reduce the necessary number of simulations. In particular, the top and bottom for each type of object were treated as producing the same size propagated uncertainty, though the top and bottom errors were not treated as being correlated. Simulations were run to ensure there would not be any large nonlinear effects when combining a change in thickness for one type of object.

Furthermore, since the DSSD and the mirror have a similar density of silicon, which is the dominant material in causing scattering from the mirrors, and because the two have as a similar thicknesses and thickness uncertainties, the the propagated uncertainties from the DSSDs and mirrors were assumed to produce similar size effects on the result. Thus, the uncertainties arising from uncertainties in the beryllium foil and mirror thicknesses were the only ones evaluated directly within Geant4. The propagated uncertainty arising from DSSD thickness was assumed to be the same size as the uncertainty arising from mirror thicknesses.

All uncertainties from material thicknesses are believed to be uncorrelated, and are added in quadrature to the final systematic uncertainty.

# Chapter 6

## Results and Conclusions

### 6.1 Measured Limits on $b_{\text{Fierz}}$ and $A_\beta$

After corrections have been applied and uncertainties evaluated, statistical confidence intervals for the 2D  $A_\beta$  vs  $b_{\text{Fierz}}$  parameter space are shown in Fig. 6.1 for all datasets combined. The final estimates of  $A_\beta$  and  $b_{\text{Fierz}}$  with uncertainties at the  $1\sigma$  level are given by:

$$b_{\text{Fierz}} = 0.033 \pm 0.084(\text{stat}) \pm 0.039(\text{sys}) \quad (6.1)$$

$$A_\beta = -0.5738 \pm 0.0082(\text{stat}) \pm 0.0041(\text{sys}), \quad (6.2)$$

and a list of uncertainties is provided in Table 6.1.

The uncertainty associated with this measurement of  $A_\beta$  is significantly larger than the collaboration’s previous measurement of using the same data, in which the final result was  $A_\beta = -0.5707 \pm 0.0013(\text{stat}) \pm 0.0013(\text{sys}) \pm 0.0005(\text{pol})$ . However, it must be noted that the present measurement is a two-parameter measurement rather than a one-parameter measurement, so it is expected to that the uncertainty associated with a single parameter should be larger.

To evaluate whether the two measurements are consistent, a thin vertical slice of Fig. 6.1 can be extracted at  $b_{\text{Fierz}} = 0$ , and its projection will provide the centroid (including systematic offsets) and statistical error associated with a one-parameter analysis for  $A_\beta$  – though this method cannot produce an estimate of the extent to which systematic uncertainties might be reduced. This ‘check’ gives a one-parameter

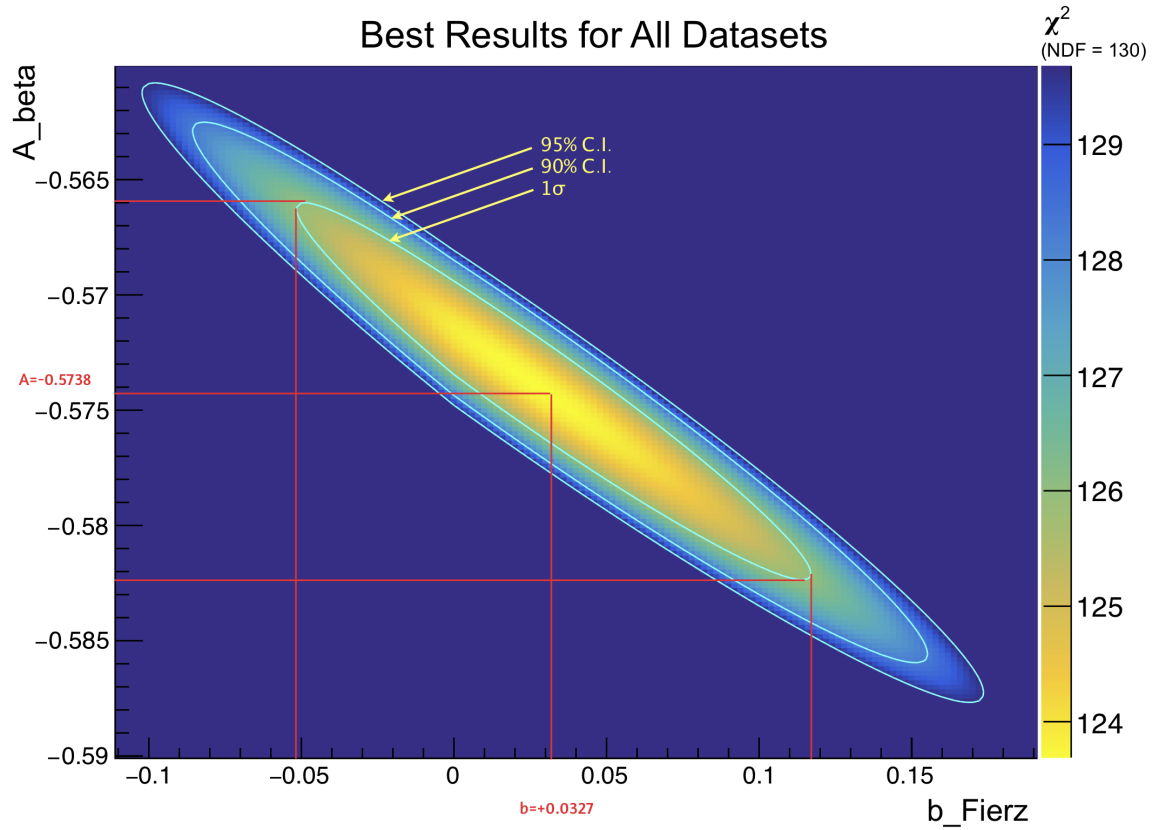


Figure 6.1: A  $\chi^2$  map to compare all data to a parameter space of  $A_\beta$  and  $b_{\text{Fierz}}$  values. All corrections have been included, however only statistical confidence intervals are shown.

measurement of  $A_\beta = -0.5714 \pm 0.0020(\text{stat})$ .

The above one-parameter result for  $A_\beta$  is consistent with the collaboration's prior result, even after one accounts for the fact that the previous result suffered from an oversight in which some partially polarized data was not removed from the final analysis for  $A_\beta$ , despite the fact that this cut *was* implemented in the associated polarization measurement. This accounts for 5% of the data used in that analysis, and is estimated to decrease the average polarization by approximately 0.3%.

An estimate of the size of the effect on the previous measurement of  $A_\beta$  suggests that the true value of  $A_\beta$  is likely to be  $\sim 0.0016$  more negative than reported. Accounting for this, a more accurate one-parameter measurement might produce the result,  $A_\beta \approx -0.5723 \pm 0.0014(\text{stat}) \pm 0.0013(\text{sys}) \pm 0.0005(\text{pol})$ .

Source	Uncertainty	
	$b_{\text{Fierz}}$	$A_\beta$
Scintillator Calibration	0.003	0.0003
Scintillator Threshold	0.004	0.0004
DSSD Individual Strip SNR	0.006	0.0007
DSSD Energy Agreement	0.005	0.0006
DSSD Detection Radius	0.006	0.0017
DSSD Energy Threshold	0.005	0.0005
Atomic Cloud	0.002	0.0002
Background	0.004	0.0003
Beta Scattering	0.031	0.0025
Low Energy Tail	0.008	0.0007
Mirror Thickness	0.013	0.0017
DSSD Thickness	0.013	0.0017
Beryllium Foil Thickness	0.004	< 0.0001
Total Systematics	0.039	0.0041
Statistics	0.084	0.0082

Table 6.1: Error budget for the two-parameter analysis, with all data included. Uncertainties are believed to be uncorrelated, and are added in quadrature. Final results:  $b_{\text{Fierz}} = 0.033 \pm 0.084(\text{stat}) \pm 0.039(\text{syst})$  and  $A_\beta = -0.5738 \pm 0.0082(\text{stat}) \pm 0.0041(\text{syst})$

## 6.2 Other Possible Future Work for the Collaboration: $R_{\text{slow}}$

The nuclear weak force is known to be a predominantly left-handed vector and axial-vector (V-A) interaction. An experiment is proposed to further test that observation, constraining the strength of right-handed (V+A) currents by exploiting the principle of conservation of angular momentum within a spin-polarized beta decay process. Here, we focus on the decay  ${}^{37}\text{K} \rightarrow {}^{37}\text{Ar} + \beta^+ + \nu_e$ . The angular correlations between the emerging daughter particles provide a rich source of information about the type of interaction that produced the decay.

### 6.2.1 Motivation

The nuclear weak force has long been known to be a predominantly left-handed chiral interaction, meaning that immediately following an interaction (such as a beta decay) with a weak force carrying boson ( $W^+$ ,  $W^-$ ,  $Z$ ), normal-matter leptons (such as the electron and electron neutrino) emerge with left-handed chirality while the anti-leptons (e.g. the positron and electron anti-neutrino) emerge with right-handed chirality. In the limit of massless particles, the particle's chirality is the same as its helicity. Thus, in a left-handed model, the direction of an (ultrarelativistic) normal lepton's spin is antiparallel direction of its motion, and the direction of spin for an anti-lepton is parallel to its direction of motion. For a non-relativistic particle the property of chirality is fairly abstract, and describes the appropriate group representation and projection operators to be used in calculations. It should be noted that a fully chiral model is also one which is maximally parity violating.

This odd quirk of the nuclear weak force is not only *predominantly* true, but it is, to the best of our current scientific knowledge, *always* true – that is, attempts to measure any right-handed chiral components of the weak force have produced results consistent with zero [1][26]. This project proposes a further measurement to constrain the strength of the right-handed component of the weak interaction.

### 6.2.2 The Decay Process

The kinematics of nuclear  $\beta^+$  decay are described by the following probability density function:

$$\begin{aligned}
W(\langle I \rangle | E_\beta \hat{\Omega}_\beta \hat{\Omega}_\nu) = & \left( \frac{1}{2\pi} \right)^5 F(-Z, E_\beta) p_\beta E_\beta (E_0 - E_\beta)^2 dE_\beta d\hat{\Omega}_\beta d\hat{\Omega}_\nu \xi \\
& \times \left[ 1 + a_{\beta\nu} \frac{\vec{p}_\beta \cdot \vec{p}_\nu}{E_\beta E_\nu} + b_{\text{Fierz}} \frac{m_e}{E_\beta} \right. \\
& + c_{\text{align}} \left( \frac{\frac{1}{3} \vec{p}_\beta \cdot \vec{p}_\nu - (\vec{p}_\beta \cdot \hat{j})(\vec{p}_\nu \cdot \hat{j})}{E_\beta E_\nu} \right) \left( \frac{I(I+1) - 3\langle (\vec{I} \cdot \hat{i})^2 \rangle}{I(2I-1)} \right) \\
& \left. + \frac{\langle \vec{I} \rangle}{I} \left( A_\beta \frac{\vec{p}_\beta}{E_\beta} + B_\nu \frac{\vec{p}_\nu}{E_\nu} + D_{\text{TR}} \frac{\vec{p}_\beta \times \vec{p}_\nu}{E_\beta E_\nu} \right) \right], \quad (6.3)
\end{aligned}$$

where  $\vec{I}$  is the nuclear spin-polarization,  $F(-Z, E_\beta)$  is the Fermi function, and parameters  $\xi$ ,  $a_{\beta\nu}$ ,  $b_{\text{Fierz}}$ ,  $c_{\text{align}}$ ,  $A_\beta$ ,  $B_\nu$ , and  $D_{\text{TR}}$  are functions that vary with the strengths of the vector, axial, scalar, and tensor couplings (constant throughout nature), as well as the Fermi and Gamow-Teller nuclear matrix elements (specific to the individual decay) [8][9].

The decay may be treated as a three-body problem in which the available kinetic energy is divided up between the beta, the neutrino, and the recoiling  $^{37}\text{Ar}$  nucleus, and (of course) the total linear and angular momentum are conserved. While the neutrino cannot be detected directly, its kinematics may be reconstructed from observations of the beta and the recoiling daughter nucleus. By placing detectors above and below the decaying atom along the axis of its polarization, we are able to obtain information about the outgoing beta's energy and momentum, in the cases of interest to us, where it is emitted along (or close to) the axis of polarization.

The recoiling  $^{37}\text{Ar}$  nucleus is a bit trickier to work with, but the task is not impossible. One useful feature of the  $^{37}\text{K} \rightarrow {}^{37}\text{Ar}$  transition is that, in addition to the  $\beta^+$  emitted in the decay itself, one or more *orbital* electrons from the parent atom are typically lost. In the majority of decay events only one orbital electron is ‘shaken off’ and so the daughter  $^{37}\text{Ar}$  atom is electrically neutral [16][27]. In the remaining cases, two or more orbital electrons are lost this way, and the daughter atom is positively charged. If we apply an electric field perpendicular to the direction of polarization,

these positively charged  $^{37}\text{Ar}^{(+n)}$  ions may be collected into a detector, from which hit position and time of flight information may be extracted. These shake-off electrons are emitted with an average energy of only  $\sim 2\text{ eV}$  so to a very good approximation the other decay products are not perturbed by the presence of shake-off electrons.

It should be noted that for the class of decays of greatest interest, where the beta and the neutrino emerge back-to-back along the polarization axis, the recoiling daughter nucleus will have zero momentum along the directions perpendicular to this axis, and on average less total energy than if the beta and neutrino were emitted in a parallel direction. Henceforth, daughter nuclei from a back-to-back decay as shown in Figure ?? will be described as ‘slow’ recoils. In terms of observables, this means that if the electric field is configured to point along one of the axes perpendicular to the polarization direction, then when the recoiling ion is swept away into a detector, the slow recoil’s hit position should be exactly along the projection of the polarization axis. Furthermore, the slow recoil’s time of flight should be in the middle of the time of flight spectrum, since other recoils will be emitted with momentum towards or away from the detector.

### 6.2.3 Status of the $R_{\text{slow}}$ Measurement

In June 2014, after several years of preparatory work beforehand (the author has been continuously involved with this project since 2010), approximately 7 days of beam time at TRIUMF was dedicated to the TRINAT  $^{37}\text{K}$  beta decay experiment. Approximately half of this data is suitable for use in this project. During this period, approximately 10,000 atoms were held within the trap at any given time. The cleaned spectra show around 50,000 polarized beta-recoil coincidence events in total, divided among measurements at three different electric field strengths (535 V/cm, 415 V/cm, 395 V/cm).

A fit to simulation has shown that the data that has already been collected has sufficient statistical power to measure the *fractional* contribution of any polarized ‘new physics’ beta decay parameter (ie right-handed, scalar, and tensor currents within the weak interaction) to a sensitivity of  $\sim 2\%$  of its true value. Systematic limitations are still being assessed.

## 6.3 Conclusions

This two-parameter analysis to measure  $A_\beta$  and  $b_{\text{Fierz}}$  has produced the results:

$$b_{\text{Fierz}} = 0.033 \pm 0.084(\text{stat}) \pm 0.039(\text{sys}) \quad (6.4)$$

$$A_\beta = -0.5738 \pm 0.0082(\text{stat}) \pm 0.0041(\text{sys}), \quad (6.5)$$

where uncertainties are evaluated at  $1\sigma$ . This measurement of  $b_{\text{Fierz}}$  is consistent with the Standard Model value of  $b_{\text{Fierz}} = 0$ , and  $A_\beta$  is consistent both with the collaboration's prior measurement of  $A_\beta$ , as well as with the value predicted by the Standard Model at  $A_\beta = -0.5706 \pm 0.0007$ .

The result for  $b_{\text{Fierz}}$  is dominated by statistical uncertainty, suggesting that the measurement could be improved simply by counting longer. There is also room for improvement in the systematic uncertainty, which is dominated by scattering and the related measurements of material thicknesses.

# Bibliography

- [1] Severijns, N., Beck, M. and Naviliat-Cuncic, O., *Tests of the standard electroweak model in nuclear beta decay*, Rev. Mod. Phys., Vol. 78, pp. 991–1040, September 2006.
- [2] Krane, K. S., Introductory Nuclear Physics, Wiley, New York, 1988.
- [3] Wong, S., Introductory Nuclear Physics, Prentice Hall Advanced Reference Series Prentice Hall Labora, Prentice Hall, 1990.
- [4] Wu, C. S., Ambler, E., Hayward, R. W., Hoppses, D. D. and Hudson, R. P., *Experimental Test of Parity Conservation in Beta Decay*, Phys. Rev., Vol. 105, pp. 1413–1415, Feb 1957.
- [5] Lee, T.-D. and Yang, C.-N., *Question of parity conservation in weak interactions*, Physical Review, Vol. 104, No. 1, pp. 254, 1956.
- [6] Falkowski, A., González-Alonso, M. and Naviliat-Cuncic, O., *Comprehensive analysis of beta decays within and beyond the Standard Model*, Journal of High Energy Physics, Vol. 2021, No. 4, pp. 1–36, 2021.
- [7] Hong, R., Sternberg, M. G. and Garcia, A., *Helicity and nuclear  $\beta$  decay correlations*, American Journal of Physics, Vol. 85, No. 1, pp. 45–53, 2017.
- [8] Jackson, J. D., Treiman, S. B. and Wyld, H. W., *Possible Tests of Time Reversal Invariance in Beta Decay*, Phys. Rev., Vol. 106, pp. 517–521, May 1957.
- [9] Jackson, J. D., Treiman, S. B. and Wyld, H. W., *Coulomb Corrections in Allowed Beta Transitions*, Nuclear Physics, Vol. 4, pp. 206–212, Nov. 1957.

- [10] Holstein, B. R., *Recoil effects in allowed beta decay: The elementary particle approach*, Reviews of Modern Physics, Vol. 46, No. 4, pp. 789–814, Oct. 1974.
- [11] Levinger, J. S., *Effects of Radioactive Disintegrations on Inner Electrons of the Atom*, Phys. Rev., Vol. 90, pp. 11–25, Apr 1953.
- [12] Raab, E. L., Prentiss, M., Cable, A., Chu, S. and Pritchard, D. E., *Trapping of Neutral Sodium Atoms with Radiation Pressure*, Phys. Rev. Lett., Vol. 59, pp. 2631–2634, Dec 1987.
- [13] Corney, A., Atomic and Laser Spectroscopy, Oxford University Press, New York, 1977.
- [14] Anholm, M., Characterizing the AC-MOT, Master's thesis, University of British Columbia, 2014.
- [15] Fenker, B., Behr, J. A., Melconian, D., Anderson, R. M. A., Anholm, M., Ashery, D., Behling, R. S., Cohen, I., Craiciu, I., Donohue, J. M., Farfan, C., Friesen, D., Gorelov, A., McNeil, J., Mehlman, M., Norton, H., Olchanski, K., Smale, S., Thériault, O., Vantyghem, A. N. and Warner, C. L., *Precision measurement of the nuclear polarization in laser-cooled, optically pumped  $^{37}\text{K}$* , New Journal of Physics, Vol. 18, No. 7, pp. 073028, 2016.
- [16] Gorelov, A., Behr, J., Melconian, D., Trinczek, M., Dubé, P., Häusser, O., Giesen, U., Jackson, K., Swanson, T., D'Auria, J., Dombsky, M., Ball, G., Buchmann, L., Jennings, B., Dilling, J., Schmid, J., Ashery, D., Deutsch, J., Alford, W., Asgeirsson, D., Wong, W. and Lee, B., *Beta-neutrino correlation experiments on laser trapped  $^{38m}\text{K}$ ,  $^{37}\text{K}$* , Hyperfine Interactions, Vol. 127, No. 1, pp. 373–380, 2000.
- [17] Swanson, T. B., Asgeirsson, D., Behr, J. A., Gorelov, A. and Melconian, D., *Efficient transfer in a double magneto-optical trap system*, J. Opt. Soc. Am. B, Vol. 15, No. 11, pp. 2641–2645, Nov 1998.
- [18] Harvey, M. and Murray, A. J., *Cold Atom Trap with Zero Residual Magnetic Field: The AC Magneto-Optical Trap*, Phys. Rev. Lett., Vol. 101, pp. 173201, Oct 2008.

- [19] Fenker, B., Gorelov, A., Melconian, D., Behr, J. A., Anholm, M., Ashery, D., Behling, R. S., Cohen, I., Craiciu, I., Gwinner, G., McNeil, J., Mehlman, M., Olchanski, K., Shidling, P. D., Smale, S. and Warner, C. L., *Precision Measurement of the  $\beta$  Asymmetry in Spin-Polarized  $^{37}\text{K}$  Decay*, Phys. Rev. Lett., Vol. 120, pp. 062502, Feb 2018.
- [20] Audi, G., Wapstra, A. and Thibault, C., *The AME2003 Atomic Mass Evaluation*, Nuclear Physics A, Vol. 729, No. 1, pp. 337 – 676, 2003.
- [21] Fenker, B. B., Precise measurement of the  $\beta$ -asymmetry in the decay of magneto-optically trapped, spin-polarized  $^{37}\text{K}$ , Ph.D. thesis, 2016.
- [22] Behling, R. S., Measurement of the Standard Model Beta Asymmetry Parameter,  $\beta$ , in  $^{37}\text{K}$ , Ph.D. thesis, 2015.
- [23] Clifford, E., Hagberg, E., Koslowsy, V., Hardy, J., Schmeing, H. and Azuma, R., *Measurements of the response of a hybrid detector telescope to mono-energetic beams of positrons and electrons in the energy range 0.8–3.8 MeV*, Nuclear Instruments and Methods in Physics Research, Vol. 224, No. 3, pp. 440–447, 1984.
- [24] Landau, L. D., *On the energy loss of fast particles by ionization*, J. Phys., Vol. 8, pp. 201–205, 1944.
- [25] Moyal, J., *XXX. Theory of ionization fluctuations*, The London, Edinburgh, and Dublin Philosophical Magazine and Journal of Science, Vol. 46, No. 374, pp. 263–280, 1955.
- [26] Severijns, N. and Naviliat-Cuncic, O., *Symmetry tests in nuclear beta decay*, Annual Review of Nuclear and Particle Science, Vol. 61, pp. 23–46, 2011.
- [27] Melconian, D. G., Measurement of the Neutrino Asymmetry in the Beta Decay of Laser-Cooled, Polarized  $^{37}\text{K}$ , Ph.D. thesis, Simon Fraser University, 2005.
- [28] Holstein, B. R., *Erratum: Recoil effects in allowed beta decay: The elementary particle approach*, Rev. Mod. Phys., Vol. 48, pp. 673–673, Oct 1976.

# Appendix A

## Notable Differences in Data Selection between this and the Previous Result

### A.1 Polarization Cycle Selection

Data used for our recent PRL article was slightly less polarized than we thought it was, due to an oversight in the data selection procedure. See Ch. ?? for a discussion of the effects.

### A.2 Leading Edge / Trailing Edge and Walk Correction

Using the leading edge rather than the trailing edge to mark the timing of TDC pulses cleans up jitter, eliminates background, and changes the relative delays between different inputs. It is immediately relevant to the shape of the ‘walk correction’ on scintillator timing pulses, which give a different prediction for beta arrival time as a function of scintillator energy.

### A.3 TOF Cut + Background Modelling

A SOE-beta time-of-flight cut is necessary to reduce background. The above mentioned walk correction directly results in an change in which specific events are

selected in a given TOF cut. It further results in an adjustment to the expected fraction of background events in any such cut.

## A.4 BB1 Energy Threshold

I use an overall 50 keV threshold, (taking +/- 10 keV from that as a systematic to be propagated/checked), but the collaboration's previous analysis used 60 keV as the default threshold.

## Appendix B

# A PDF For The People

### B.1 JTW

Here's a master equation from JTW to describe beta decay kinematics [8], [9]:

$$\begin{aligned} d^5\Gamma_{\text{JTW}} \equiv & \frac{F_{\mp}(Z, E_\beta)}{(2\pi)^5} p_\beta E_\beta (E_0 - E_\beta)^2 dE_\beta d^3\hat{\Omega}_\beta d^3\hat{\Omega}_\nu \\ & \times \xi \left[ 1 + a_{\beta\nu} \frac{\vec{p}_\beta \cdot \vec{p}_\nu}{E_\beta E_\nu} + b_{\text{Fierz}} \frac{m_e c^2}{E_\beta} + c_{\text{align}} T_{\text{align}}(\vec{J}) \left( \frac{\vec{p}_\beta \cdot \vec{p}_\nu}{3E_\beta E_\nu} - \frac{(\vec{p}_\beta \cdot \hat{\vec{j}})(\vec{p}_\nu \cdot \hat{\vec{j}})}{E_\beta E_\nu} \right) \right. \\ & \left. + \frac{\vec{J}}{J} \cdot \left( A_\beta \frac{\vec{p}_\beta}{E_\beta} + B_\nu \frac{\vec{p}_\nu}{E_\nu} + D_{\text{TR}} \frac{\vec{p}_\beta \times \vec{p}_\nu}{E_\beta E_\nu} \right) \right] \end{aligned} \quad (\text{B.1})$$

where, for convenience, we have defined a nuclear alignment term,

$$T_{\text{align}}(\vec{J}) \equiv \frac{J(J+1) - 3\langle(\vec{J} \cdot \hat{\vec{j}})^2\rangle}{J(2J-1)}. \quad (\text{B.2})$$

Note that this master equation depends on neutrino momentum, which we cannot observe directly. Furthermore, we cannot reconstruct neutrino momenta in our decay events either, because it would be necessary to account for the momentum of the recoiling daughter nucleus, treating the decay as a three-body problem. From an experimental standpoint, we failed to measure the momenta of the daughters in conjunction with the “tagged” beta decay events with which we are primarily con-

cerned in this thesis. From a theoretical standpoint, JTW has intentionally neglected recoil-order terms – meaning that the daughter nucleus is treated, for the purpose of kinetic energy calculations, as being infinitely massive, and as such it must have no change in kinetic energy from the decay. This approximation makes it a bit tricky to correctly re-formulate Eq. (B.1) in terms of the momentum of the daughter instead of the momentum of the neutrino.

Fortunately, it is possible to simplify Eq. (B.1) by integrating over all possible neutrino directions, such that the result no longer depends on parameters that we do not observe. The neutrino energy itself is not a free variable in this equation, because the energy release in the decay is fixed, and given the approximation that none of that energy is allocated to the recoiling daughter, it is very straightforward to calculate the neutrino energy for a decay event in which the beta energy is known.

The result of performing this integration over neutrino direction is:

$$\begin{aligned} d^3\Gamma dE_\beta d^3\hat{\Omega}_\beta &= \frac{2}{(2\pi)^4} F_{\mp}(Z, E_\beta) p_\beta E_\beta (E_0 - E_\beta)^2 dE_\beta d^3\hat{\Omega}_\beta \xi \\ &\times \left[ 1 + b_{\text{Fierz}} \frac{m_e c^2}{E_\beta} + A_\beta \left( \frac{\vec{J}}{J} \cdot \frac{\vec{p}_\beta}{E_\beta} \right) \right], \end{aligned} \quad (\text{B.3})$$

which is a great simplification on Eq. (B.1). We still must write the remaining parameters in terms of the relevant nuclear matrix elements and fundamental coupling constants. These coupling constants are, in general, complex-valued, and JTW does not choose a phase angle for us. We write them out in Eqs. (B.4-B.6).

$$\begin{aligned} \xi &= |M_F|^2 (|C_S|^2 + |C_V|^2 + |C'_S|^2 + |C'_V|^2) \\ &+ |M_{GT}|^2 (|C_T|^2 + |C_A|^2 + |C'_T|^2 + |C'_A|^2) \end{aligned} \quad (\text{B.4})$$

$$b_{\text{Fierz}} \xi = \pm 2\gamma \text{Re}[|M_F|^2 (C_S C_V^* + C'_S C'^*_V) + |M_{GT}|^2 (C_T C_A^* + C'_T C'^*_A)] \quad (\text{B.5})$$

$$\begin{aligned} A_\beta \xi &= |M_{GT}|^2 \lambda_{J'J} \left[ \pm 2\text{Re}[C_T C'^*_T - C_A C'^*_A] + 2 \frac{\alpha Z m_e}{p_\beta} \text{Im}[C_T C'^*_A + C'_T C_A^*] \right] \\ &+ \delta_{J'J} M_F M_{GT} \left( \frac{J}{J+1} \right)^{1/2} \left[ 2 \text{Re}[C_S C'^*_T + C'_S C_T^* - C_V C'^*_A - C'_V C_A^*] \right. \\ &\left. \pm 2 \frac{\alpha Z m_e}{p_\beta} \text{Im}[C_S C'^*_A + C'_S C_A^* - C_V C'^*_T - C'_V C_T^*] \right] \end{aligned} \quad (\text{B.6})$$

Note that JTW presents slightly different expressions for the sign convention in

components of  $A_\beta$  within [8] and [9]. Here, we adopt the convention from the latter publication. Furthermore, we do not require that either  $M_F$  or  $M_{GT}$  be positive (which would allow us to safely drop their absolute value indicators and make the conventions of these two papers equivalent). In order to obtain the correct, physically observed value for  $A_\beta$ , we require that the  $M_F M_{GT}$  term in Eq. (B.6) have an overall positive value. Because we know that the scalar and tensor couplings must be small, and any imaginary contributions to the term must be small, we conclude that

$$M_F M_{GT} (C_V C_A'^* + C_V' C_A^*) < 0. \quad (\text{B.7})$$

## B.2 Holstein

Holstein [10] [28] generously provides explicit equations to match both Eq. (B.1) (i.e. Holstein's Eq. (51), where neutrino direction is a parameter of the probability distribution) and Eq. (B.3) (Holstein's Eq. (52), where neutrino direction has already been integrated over).

Here's Holstein's Eq. (52):

$$\begin{aligned} d^3\Gamma_{\text{Holstein}} = & 2G_v^2 \cos^2 \theta_c \frac{F_{\mp}(Z, E_\beta)}{(2\pi)^4} p_\beta E_\beta (E_0 - E_\beta)^2 dE_\beta d^3\hat{\Omega}_\beta \\ & \times \left\{ F_0(E_\beta) + \Lambda_1 F_1(E_\beta) \hat{\mathbf{n}} \cdot \frac{\vec{p}_\beta}{E_\beta} + \Lambda_2 F_2(E_\beta) \left[ \left( \hat{\mathbf{n}} \cdot \frac{\vec{p}_\beta}{E_\beta} \right)^2 - \frac{1}{3} \frac{p_\beta^2}{E_\beta^2} \right] \right. \\ & \left. + \Lambda_3 F_3(E_\beta) \left[ \left( \hat{\mathbf{n}} \cdot \frac{\vec{p}_\beta}{E_\beta} \right)^3 - \frac{3}{5} \frac{p_\beta^2}{E_\beta^2} \hat{\mathbf{n}} \cdot \frac{\vec{p}_\beta}{E_\beta} \right] \right\} \end{aligned} \quad (\text{B.8})$$

A careful reader will eventually note that Holstein's spectral functions  $F_i(E_\beta)$  are not the same as the  $F_i(E_\beta, u, v, s)$  in any limit, despite the notational similarities. Among other rules, Holstein's spectral functions obey these:

$$F_i(E_\beta) \neq F_i(E_\beta, u, v, s) \quad (\text{B.9})$$

$$F_i(E_\beta) = H_i(E_\beta, u, v, 0) \quad (\text{B.10})$$

$$f_i(E_\beta) = F_i(E_\beta, u, v, 0). \quad (\text{B.11})$$

For the  $F_i(E_\beta)$  functions of interest to us here, we find the following relationships:

$$\begin{aligned}
F_0(E_\beta) &= H_0(E_\beta, J, J', 0) = F_1(E_\beta, J, J', 0) &= f_1(E_\beta) \\
F_1(E_\beta) &= H_1(E_\beta, J, J', 0) = F_4(E_\beta, J, J', 0) + \frac{1}{3}F_7(E_\beta, J, J', 0) &= f_4(E_\beta) + \frac{1}{3}f_7(E_\beta) \\
F_2(E_\beta) &= H_2(E_\beta, J, J', 0) = F_{10}(E_\beta, J, J', 0) + \frac{1}{2}F_{13}(E_\beta, J, J', 0) &= f_{10}(E_\beta) + \frac{1}{3}f_{13}(E_\beta) \\
F_3(E_\beta) &= H_3(E_\beta, J, J', 0) = F_{18}(E_\beta, J, J', 0) &= f_{18}(E_\beta). \quad (\text{B.12})
\end{aligned}$$

Note that the  $f_i(E_\beta)$  in Eq. B.12 are the same spectral functions used to describe a polarized decay spectrum when the neutrino (ie, the recoil) is also observed – though of course such a spectrum must have other terms as well. For the spectrum of interest to us here, in which the neutrino direction has already been integrated over, we can simply look up the  $H_i(E_\beta, J, J', 0) = H_i(E, u, v, s=0)$  spectral functions, and leave it at that. We find:

$$\begin{aligned}
F_0(E_\beta) &= |a_1|^2 + 2 \operatorname{Re}[a_1^* a_2] \frac{1}{3M^2} \left[ m_e^2 + 4E_\beta E_0 + 2 \frac{m_e^2}{E_\beta} E_0 - 4E_\beta^2 \right] \\
&\quad + |c_1|^2 + 2 \operatorname{Re}[c_1^* c_2] \frac{1}{9M^2} \left[ 11m_e^2 + 20E_\beta E_0 - 2 \frac{m_e^2}{E_\beta} E_0 - 20E_\beta^2 \right] \\
&\quad - 2 \frac{E_0}{3M} \operatorname{Re}[c_1^*(c_1 + d \pm b)] + \frac{2E_\beta}{3M} (3|a_1|^2 + \operatorname{Re}[c_1^*(5c_1 \pm 2b)]) \\
&\quad - \frac{m_e^2}{3ME_\beta} \operatorname{Re} \left[ -3a_1^* e + c_1^* \left( 2c_1 + d \pm 2b - h \frac{E_0 - E_\beta}{2M} \right) \right] \quad (\text{B.13})
\end{aligned}$$

$$\begin{aligned}
F_1(E_\beta) &= \delta_{u,v} \left( \frac{u}{u+1} \right)^{1/2} \left\{ 2 \operatorname{Re} \left[ a_1^* \left( c_1 - \frac{E_0}{3M} (c_1 + d \pm b) + \frac{E_\beta}{3M} (7c_1 \pm b + d) \right) \right] \right. \\
&\quad + 2 \operatorname{Re}[a_1^* c_2 + c_1^* a_2] \left( \frac{4E_\beta(E_0 - E_\beta) + 3m_e^2}{3M^2} \right) \Big\} \\
&\quad \mp \frac{(-1)^s \gamma_{u,v}}{u+1} \operatorname{Re} \left\{ c_1^* \left( c_1 + 2c_2 \left( \frac{8E_\beta(E_0 - E_\beta) + 3m_e^2}{3M^2} \right) - \frac{2E_0}{3M} (c_1 + d \pm b) \right. \right. \\
&\quad \left. \left. + \frac{E_\beta}{3M} (11c_1 - d \pm 5b) \right) \right\} + \frac{\lambda_{u,v}}{u+1} \operatorname{Re} \left\{ c_1^* \left[ -f \left( \frac{5E_\beta}{M} \right) \right. \right. \\
&\quad \left. \left. + g \left( \frac{3}{2} \right)^{1/2} \left( \frac{E_0^2 - 11E_0E_\beta + 6m_e^2 + 4E_\beta^2}{6M^2} \right) \pm 3j_2 \left( \frac{8E_\beta^2 - 5E_0E_\beta - 3m_e^2}{6M^2} \right) \right] \right\} \quad (\text{B.14})
\end{aligned}$$

$$\begin{aligned}
F_2(E_\beta) = & \theta_{u,v} \frac{E_\beta}{2M} \operatorname{Re} \left[ c_1^* \left( c_1 + c_2 \frac{8(E_0 - E_\beta)}{3M} - d \pm b \right) \right] \\
& - \delta_{u,v} \frac{E_\beta}{M} \left[ \frac{u(u+1)}{(2u-1)(2u+3)} \right]^{1/2} \operatorname{Re} \left\{ a_1^* \left( \left(\frac{3}{2}\right)^{1/2} f + g \frac{E_\beta + 2E_0}{4M} \right. \right. \\
& \left. \left. \pm \left(\frac{3}{2}\right)^{1/2} j_2 \frac{E_0 - E_\beta}{2M} \right) \right\} + (-1)^s \kappa_{u,v} \frac{E_\beta}{2M} \operatorname{Re} \left[ c_1^* \left( \pm 3f \pm \left(\frac{3}{2}\right)^{1/2} g \frac{E_0 - E_\beta}{M} \right. \right. \\
& \left. \left. + 3j_2 \frac{E_0 - 2E_\beta}{2M} \right) \right] + \epsilon_{u,v} \operatorname{Re}[c_1^* j_3] \left( \frac{21E_\beta^2}{8M^2} \right)
\end{aligned} \tag{B.15}$$

$$\begin{aligned}
F_3(E_\beta) = & -\delta_{u,v} (3u^2 + 3u - 1) \left[ \frac{u}{(u-1)(u+1)(u+2)(2u-1)(2u+3)} \right]^{1/2} \\
& \times \operatorname{Re}[a_1^* j_3] \left( \frac{E_\beta^2 \sqrt{15}}{4M^2} \right) + \frac{\rho_{u,v}}{u+1} \operatorname{Re} \left[ c_1^* (g\sqrt{3} + j_2\sqrt{2}) \left( \frac{5E_\beta^2}{4M^2} \right) \right] \\
& \pm \frac{(-1)^s \sigma_{u,v}}{u+1} \operatorname{Re}[c_1^* j_3] \left( \frac{5E_\beta^2}{2M^2} \right)
\end{aligned} \tag{B.16}$$

and we might really appreciate if these things could be simplified a bit.

The terms  $a_1, a_2, b, c_1, c_2, d, e, f, g, h, j_2, j_3$  are “structure functions”. Holstein gives some predictions for their form, assuming the impulse approximation holds, in his Eq. (67). For the most part, the values and form of these structure functions are beyond the scope of this thesis, so I will not re-write them all here. It should be noted that the numerical values used for these parameters came from a private communication from Ian Towner to the collaboration. However, it is important to note the expressions for  $a_i$  and  $c_i$ , because these will directly come into play when we try to reconcile Holstein’s expression with JTW’s. Therefore,

$$a(q^2) \approx \frac{g_V(q^2)}{\left(1 + \frac{\Delta}{2M}\right)} \left[ M_F + \frac{1}{6}(q^2 - \Delta^2)M_{r^2} + \frac{1}{3}\Delta M_{\mathbf{r} \cdot \mathbf{p}} \right] \tag{B.17}$$

$$\begin{aligned}
c(q^2) \approx & \frac{g_A(q^2)}{\left(1 + \frac{\Delta}{2M}\right)} \left[ M_{GT} + \frac{1}{6}(q^2 - \Delta^2)M_{\sigma r^2} + \frac{1}{6\sqrt{10}}(2\Delta^2 + q^2)M_{1y} \right. \\
& \left. + A \frac{\Delta}{2M} M_{\sigma L} + \frac{1}{2}\Delta M_{\sigma rp} \right]
\end{aligned} \tag{B.18}$$

...where the  $M_{xxx}$ ’s are certain nuclear matrix elements. However, Eqs. (B.13-B.16) are not written in terms of  $a(q^2)$  and  $c(q^2)$ , but rather in terms of  $a_1, a_2, c_1$ , and  $c_2$ .

In fact, Holstein is implicitly using series expansions to remove the dependence on recoil momentum, so that

$$a(q^2) = a_1 + \left(\frac{q^2}{M^2}\right) a_2 + \dots \quad (\text{B.19})$$

$$c(q^2) = c_1 + \left(\frac{q^2}{M^2}\right) c_2 + \dots \quad (\text{B.20})$$

Next, Holstein goes and tweaks those  $F_i(E_\beta)$  terms that we've already written out, by adding in an adjustment for Coulomb corrections. Those corrections have this form:

$$F_i(E_\beta) \rightarrow \tilde{F}_i(E_\beta) := F_\mp(Z, E_\beta) [F_i(E_\beta) + \Delta F_i(E_\beta)] \quad (\text{B.21})$$

To obtain expressions for the  $\Delta F_i(E_\beta)$ , Holstein invokes some Feynman diagrams and provides expressions for several integrals, all of which are both complex and complicated. The modified spectral functions are provided in terms of functions of these integrals. Since nobody wants to have to evaluate those integrals, Holstein makes a further approximation by taking only the first term in an expansion of the  $\Delta F_i(E_\beta)$  in terms of  $Z\alpha$ , where  $Z\alpha \ll 1$ . Then, the resulting expressions for  $\Delta F_i(E_\beta)$  can be written in terms of much more straightforward integrals over form factors for electric charge and weak charge.

If we make the further assumption that these form factors are identical, and that both types of charge are spread over a ball of uniform density with radius  $R$ , then we find:

$$X = Y = \frac{9\pi R}{140} \quad (\text{B.22})$$

in the Eqs. (B.23 - B.25) that follow.

Because Holstein doesn't actually write this stuff out in terms of  $F_i(E_\beta)$ , but rather in terms of  $F_i(E_\beta, u, v, s)$ , this correction presents yet another opportunity for the reader to interpret his notation incorrectly. We note that one must remember to make use of the relations in Eq. (B.12). Furthermore, Holstein notes that some of the terms  $F_i(E_\beta, u, v, s)$  are suppressed already, and he does not consider those terms further. We will take this approximation to be adequate for our purposes here.

So, we'll write out the functions for these corrections.

$$\begin{aligned}\Delta F_1(E_\beta, u, v, s) = & \mp \left( \frac{8\alpha Z}{3\pi} \right) X \left[ E_\beta \left( 8|a|^2 + \frac{28}{3}|c|^2 \right) + E_0 \left( |a|^2 - \frac{1}{3}|c|^2 \right) \right. \\ & \left. + 3 \left( \frac{m_e c^2}{E_\beta} \right) (|a|^2 + |c|^2) \right]\end{aligned}\quad (\text{B.23})$$

$$\Delta F_4(E_\beta, u, v, s) = \mp \left( \frac{8\alpha Z}{3\pi} \right) 9XE_\beta \left[ 2\delta_{u,v} \left( \frac{u}{u+1} \right)^{1/2} \text{Re}[a^*c] \mp (-1)^s \left( \frac{\gamma_{u,v}}{u+1} \right) |c|^2 \right]\quad (\text{B.24})$$

$$\begin{aligned}\Delta F_7(E_\beta, u, v, s) = & \mp \left( \frac{8\alpha Z}{3\pi} \right) X (E_0 - E_\beta) \left[ 2\delta_{u,v} \left( \frac{u}{u+1} \right)^{1/2} \text{Re}[a^*c] \right. \\ & \left. \mp (-1)^s \left( \frac{\gamma_{u,v}}{u+1} \right) |c|^2 \right]\end{aligned}\quad (\text{B.25})$$

We note that the above corrections have been written in terms of  $a(q^2)$  and  $c(q^2)$ , and we must use Eqs. (B.19, B.20) to put the results in terms of  $a_1$ ,  $a_2$ ,  $c_1$ , and  $c_2$  so that they can be correctly combined with Eqs. (B.13-B.16).

If we evaluate Holstein's Eqs. (B8), which I will absolutely not type out here, for the case  $u = v = J = J' = 3/2$ , we find the following values:

$$\begin{aligned}\delta_{u,v} &= 1 & \theta_{u,v} &= 1 & \rho_{u,v} &= \frac{-41}{40} \\ \gamma_{u,v} &= 1 & \kappa_{u,v} &= \frac{1}{2\sqrt{2}} & \sigma_{u,v} &= \frac{-41}{4\sqrt{35}} \\ \lambda_{u,v} &= \frac{-\sqrt{2}}{5} & \epsilon_{u,v} &= \frac{-1}{2\sqrt{5}} & \phi_{u,v} &= 0\end{aligned}\quad (\text{B.26})$$

Furthermore, in our calculations here, we will be considering only the  $\beta^+$  decay modes, and therefore we take the *lower* sign when the option arises. We also will use  $s = 0$ , so that  $(-1)^s = +1$ .

We proceed by defining some notational conventions. Firstly,

$$\text{Holstein's } \hat{n} = \text{JTW's } \mathbf{j}, \quad (\text{B.27})$$

and the  $\Lambda_i$  are given by Holstein's Eq. (48):

$$\Lambda_1 := \frac{\langle M \rangle}{J} \quad (\text{B.28})$$

$$\Lambda_2 := 1 - \frac{3\langle M^2 \rangle}{J(J+1)} \quad (\text{B.29})$$

$$\Lambda_3 := \frac{\langle M \rangle}{J} - \frac{5\langle M^3 \rangle}{J(3J^2 + 3J - 1)}. \quad (\text{B.30})$$

It can be immediately seen that Holstein's  $\Lambda_1$  is closely related to JTW's  $\frac{\vec{J}}{J}$ , and Holstein's  $\Lambda_2$  is closely related to JTW's  $T_{\text{align}}$ . JTW has no equivalent to  $\Lambda_3$ . We find:

$$\Lambda_1 \hat{\mathbf{j}} = \frac{\langle M \rangle}{J} \hat{\mathbf{j}} = \frac{\vec{\mathbf{j}}}{J} \quad (\text{B.31})$$

$$\Lambda_2 = T_{\text{align}} \frac{(2J-1)}{(J+1)}. \quad (\text{B.32})$$

## Appendix C

# Comparing Notation between Holstein and JTW

This section provides several equations and tables intended to be used as a quick reference for comparing differences in notation, sign convention, and normalization between two different descriptions of the beta decay probability distribution. This section also includes several pages of handwritten notes.

The following equations provide a term-by-term comparison between the Holstein and JTW conventions, intentionally neglecting ROC terms.

$$\xi = G_v^2 \cos \theta_C f_1(E) \quad (\text{C.1})$$

$$a_{\beta\nu} = f_2(E) / f_1(E) \quad (\text{C.2})$$

$$\frac{\langle \vec{J} \rangle}{J} \cdot \frac{\vec{p}}{E} A_\beta = \Lambda_1 \hat{n} \cdot \frac{\vec{p}}{E} f_4(E) / f_1(E) \quad (\text{C.3})$$

$$\frac{\langle \vec{J} \rangle}{J} \cdot \frac{\vec{p}_\nu}{E_\nu} B_\nu = \Lambda_1 \hat{n} \cdot \vec{k} f_6(E) / f_1(E) \quad (\text{C.4})$$

$$\frac{\langle \vec{J} \rangle}{J} \cdot \frac{(\vec{p} \times \vec{p}_\nu)}{EE_\nu} D_{\text{TR}} = \Lambda_1 \hat{n} \cdot \left( \frac{\vec{p}}{E} \times \hat{k} \right) f_8(E) / f_1(E) \quad (\text{C.5})$$

$$\begin{aligned} & \left[ \frac{J(J+1) - 3\langle (\vec{J} \cdot \hat{j})^2 \rangle}{J(2J-1)} \right] \left[ \frac{1}{3} \frac{\vec{p} \cdot \vec{p}_\nu}{EE_\nu} - \frac{(\vec{p} \cdot \hat{j})(\vec{p}_\nu \cdot \hat{j})}{EE_\nu} \right] c_{\text{align}} \\ &= \Lambda_2 \left[ (\hat{n} \cdot \frac{\vec{p}}{E})(\hat{n} \cdot \hat{k}) - \frac{1}{3} (\frac{\vec{p}}{E} \cdot \hat{k}) \right] f_{12}(E) / f_1(E) \end{aligned} \quad (\text{C.6})$$

Holstein	JTW	Thesis	Comments
$k$			Neutrino momentum 4-vector
	$E_\nu$		Neutrino energy
$\hat{k}$	$\frac{\mathbf{p}_\nu}{E_\nu}$		3D Neutrino emission direction unit vector. Neutrinos are always treated as massless.
$p$			Beta momentum 4-vector, or sometimes the magnitude of the beta momentum 3-vector. Never the magnitude of the 4-vector.
$E$	$E_e$	$E_\beta$	Beta energy
$\mathbf{p}$	$\mathbf{p}_e$	$\vec{p}_\beta$	Beta momentum 3-vector
$q$			Recoil momentum 4-vector, or sometimes a magnitude.

Table C.1: A comparison of some kinematic terms in JTW [8] [9] and Holstein [10][28]. Bolding/italicization carries meaning.

Holstein	JTW	Comments
$u$	$J$	Initial state total nuclear angular momentum.
$v$	$J'$	Final state total nuclear angular momentum.
$s$	No equivalent	

Table C.2: A comparison of some angular momenta in JTW [8] [9] and Holstein [10][28].

Holstein	JTW	Thesis	Comments
$G_v^2 \cos \theta_C f_1(E)$	$\xi$	$\xi(E_\beta)$	Normalization. Proportional to the fractional decay rate.
$\hat{n}$	$\mathbf{j}$	$\hat{\mathbf{j}}$	Nuclear polarization unit vector. Also the axis of quantization.
$J$	$J$		Total nuclear angular momentum quantum number
$\langle M \rangle$	$ \langle \mathbf{J} \rangle $		Angular momentum projection along the axis of quantization
$\Lambda^{(1)} \hat{n} = \frac{\langle M \rangle}{J} \hat{n}$	$\frac{\langle \mathbf{J} \rangle}{J}$	$\Lambda_1 \hat{\mathbf{n}}$	Dipole element vector. Proportional to nuclear polarization.
$\Lambda^{(2)}$	$\frac{J(J+1)-3\langle (\vec{\mathbf{J}} \cdot \hat{\mathbf{j}})^2 \rangle}{J(2J-1)} \frac{(2J-1)}{(J+1)}$	$T_{\text{align}}(\vec{\mathbf{J}}) \frac{(2J-1)}{(J+1)}$	Quadrupole element
$\Lambda^{(3)}$	No equivalent	$\Lambda_3$	Octopole element
$\Lambda^{(4)}$	No equivalent	$\Lambda_4$	Hexadecapole element

Table C.3: A comparison of terms relating to multipole elements and their normalizations in JTW [8] [9] and Holstein [10] [28].

Term	Integral
$f_1(E_\beta)$	$\int 1 \, d\hat{\Omega}_k = 4\pi$
$f_2(E_\beta)$	$\int \left( \frac{\vec{p}_\beta \cdot \hat{k}}{E_\beta} \right) d\hat{\Omega}_k = 0$
$f_3(E_\beta)$	$\int \left( \left( \frac{\vec{p}_\beta \cdot \hat{k}}{E_\beta} \right)^2 - \frac{1}{3} \frac{p_\beta^2}{E_\beta^2} \right) d\hat{\Omega}_k = 0$
$f_4(E_\beta)$	$\int \left( \hat{n} \cdot \frac{\vec{p}_\beta}{E_\beta} \right) d\hat{\Omega}_k = 4\pi \left( \hat{n} \cdot \frac{\vec{p}_\beta}{E_\beta} \right)$
$f_5(E_\beta)$	$\int \left( \hat{n} \cdot \frac{\vec{p}_\beta}{E_\beta} \right) \left( \frac{\vec{p}_\beta \cdot \hat{k}}{E_\beta} \right) d\hat{\Omega}_k = 0$
$f_6(E_\beta)$	$\int \left( \hat{n} \cdot \hat{k} \right) d\hat{\Omega}_k = 0$
$f_7(E_\beta)$	$\int \left( \hat{n} \cdot \hat{k} \right) \left( \frac{\vec{p}_\beta \cdot \hat{k}}{E_\beta} \right) d\hat{\Omega}_k = \frac{1}{3} 4\pi \left( \hat{n} \cdot \frac{\vec{p}_\beta}{E_\beta} \right)$
$f_8(E_\beta)$	$\int \hat{n} \cdot \left( \frac{\vec{p}_\beta \times \hat{k}}{E_\beta} \right) d\hat{\Omega}_k = 0$
$f_9(E_\beta)$	$\int \hat{n} \cdot \left( \frac{\vec{p}_\beta \times \hat{k}}{E_\beta} \right) \left( \frac{\vec{p}_\beta \cdot \hat{k}}{E_\beta} \right) d\hat{\Omega}_k = 0$
$f_{10}(E_\beta)$	$\int T_2(\hat{n}) : \left[ \frac{\vec{p}_\beta}{E}, \frac{\vec{p}_\beta}{E} \right] d\hat{\Omega}_k = 4\pi T_2(\hat{n}) : \left[ \frac{\vec{p}_\beta}{E}, \frac{\vec{p}_\beta}{E} \right]$
$f_{11}(E_\beta)$	$\int T_2(\hat{n}) : \left[ \frac{\vec{p}_\beta}{E}, \frac{\vec{p}_\beta}{E} \right] \left( \frac{\vec{p}_\beta \cdot \hat{k}}{E} \right) d\hat{\Omega}_k = 0$
$f_{12}(E_\beta)$	$\int T_2(\hat{n}) : \left[ \frac{\vec{p}_\beta}{E}, \hat{k} \right] d\hat{\Omega}_k = 0$
$f_{13}(E_\beta)$	$\int T_2(\hat{n}) : \left[ \frac{\vec{p}_\beta}{E}, \hat{k} \right] \left( \frac{\vec{p}_\beta \cdot \hat{k}}{E} \right) d\hat{\Omega}_k = \frac{1}{3} 4\pi T_2(\hat{n}) : \left[ \frac{\vec{p}_\beta}{E}, \frac{\vec{p}_\beta}{E} \right]$
$f_{14}(E_\beta)$	$\int T_2(\hat{n}) : \left[ \hat{k}, \hat{k} \right] d\hat{\Omega}_k = 0$
$f_{15}(E_\beta)$	$\int T_2(\hat{n}) : \left[ \hat{k}, \hat{k} \right] \left( \frac{\vec{p}_\beta \cdot \hat{k}}{E} \right) d\hat{\Omega}_k = 0$
$f_{16}(E_\beta)$	$\int T_2(\hat{n}) : \left[ \frac{\vec{p}_\beta}{E}, \frac{\vec{p}_\beta}{E} \times \hat{k} \right] d\hat{\Omega}_k = 0$
$f_{17}(E_\beta)$	$\int T_2(\hat{n}) : \left[ \hat{k}, \frac{\vec{p}_\beta}{E} \times \hat{k} \right] d\hat{\Omega}_k = 0$
$f_{18}(E_\beta)$	$\int T_3(\hat{n}) : \left[ \frac{\vec{p}_\beta}{E}, \frac{\vec{p}_\beta}{E}, \frac{\vec{p}_\beta}{E} \right] d\hat{\Omega}_k = 4\pi T_3(\hat{n}) : \left[ \frac{\vec{p}_\beta}{E}, \frac{\vec{p}_\beta}{E}, \frac{\vec{p}_\beta}{E} \right]$

Table C.4: Integrals of terms from Holstein's Eq. (51) [10] [28].

$C_A = C'_A$ ;  $g = \pm \frac{1}{\sqrt{2}} M_{GT} (C_A + C'_A)$  ← prefer  $\oplus$   
 $C_V = C'_V$ ;  $a_1 = \pm \frac{1}{\sqrt{2}} M_F (C_V + C'_V)$  ← depends on above sign.

In our code:  
 $M_F = 1.0$   
 $M_{GT} = -0.62376$

Also in our Code:  
 $g_V = 1.00$   
 $g_A = 0.91210$

\* Really, the conversion above doesn't include the extra terms in  $a_1$  and  $g$  that couple to <sup>nuclear</sup> matrix elements other than  $M_F$  and  $M_{GT}$ .

I think the point is that I should actually interpret:

$$g_V = \pm \frac{1}{\sqrt{2}} (C_V + C'_V) = 1.0 \rightarrow a_1 = g_V M_F \Rightarrow C_V = C'_V = \frac{1}{\sqrt{2}}$$

$$g_A = \pm \frac{1}{\sqrt{2}} (C_A + C'_A) \approx 0.91210 \rightarrow C_1 = g_A M_{GT} \Rightarrow C_A = C'_A = \frac{-0.91210}{\sqrt{2}} \approx -0.644952$$

\* Check: with  $C_A = C'_A$  and  $C = C'_V$ , does JTW give the right  $A_\beta$ ?  
 $A_\beta = 0.763683; A_\beta = 0.496903 \rightarrow A_\beta = \underline{\underline{0.375394}}$  (bad!)

$A_\beta = 0.763671 \leftarrow$  Allow  $M_{GT}$  and  $M_F$  to have opposite signs. (Bad!)  
 $A_\beta = -0.568045 \leftarrow$  enforce  $\oplus M_{GT}$ . Or earlier JTW "convention".  
 Because Holstein insists on his own sign convention, we get  $M_{GT-Holstein} = -M_{GT-JTW}$

Figure C.1: "Notes 0"

In our code:

$$\boxed{\begin{array}{lll} M_F = 1.0 & ; g_V = 1.0 & \rightarrow g_V M_F = 1.0 \\ M_{GT} = -0.62376 & ; g_A = 0.91210 & \rightarrow g_A M_{GT} = -0.568931 \end{array}} \Rightarrow \rho \equiv \frac{g_A M_{GT}}{g_V M_F} \approx -0.568931$$

Holstein

\* If we require that  $C_A, C_A', C_V, C_V', M_F, M_{GT}$  are all real, and enforce that these can all take values which allow for Holstein and JTWW to be equivalent in some limits, we require:

$$\begin{array}{lll} \text{JTWW} & \text{Holstein} & \text{Holstein} \quad \text{JTWW} \\ \left\{ \begin{array}{l} f_1(E) \\ f_4(E) \end{array} \right. & \rightarrow \begin{array}{l} |a_1|^2 = |M_F|^2 (|C_V|^2 + |C_V'|^2) \\ |C_1|^2 = |M_{GT}|^2 (|C_A|^2 + |C_A'|^2) \end{array} \\ \downarrow \quad \downarrow & & \downarrow \quad \downarrow \\ \rightarrow |a_1|^2 = 2|M_{GT}|^2 \cdot \text{Re}[C_A C_A'^*] \end{array}$$

$$\begin{aligned} \text{Re}[a_1^* C_1] &= -\text{Re}[M_F M_{GT} (C_V C_A'^* + C_V' C_A^*)] \leftarrow \text{later} \\ \text{Re}[a_1^* C_1] &= -\text{Re}[|M_F| |M_{GT}| (C_V C_A'^* + C_V' C_A^*)] \leftarrow \text{earlier.} \end{aligned}$$

The Results:

$$\begin{array}{lll} C_V = C_V' & \text{Holstein} & \text{JTWW} \\ C_A = C_A' & a_1 = \pm \frac{1}{\sqrt{2}} M_F (C_V + C_V') = \pm M_F (\pm \sqrt{2}) (C_V) \\ & C_1 = \pm \frac{1}{\sqrt{2}} M_{GT} (C_A + C_A') = \pm M_{GT} (\pm \sqrt{2}) (C_A) \end{array}$$

$$a_1 \approx g_V M_{F,H};$$

$$C_1 \approx g_A M_{GT,H};$$

~~Holstein~~

$$\boxed{M_{GT, \text{Holstein}} = -M_{GT, \text{JTWW}}}$$

which sign?!

$$a_1 \approx g_V M_F; \quad g_V = \pm \frac{1}{\sqrt{2}} (C_V + C_V') = 1.0; \quad M_F = 1.0; \quad ; \quad C_V = C_V'$$

$$C_1 \approx g_A M_{GT}; \quad g_A = \pm \frac{1}{\sqrt{2}} (C_A + C_A') \approx 0.91210; \quad M_{GT} = -0.62376; \quad C_A = C_A'$$

$\uparrow \uparrow$   
JTWW terms!

Figure C.2: "Notes 1"

$$\begin{aligned}
 b \cdot \bar{z} &= \pm 2\gamma \operatorname{Re} \left[ |M_F|^2 (C_S C_V^* + C'_S C_V'^*) + |M_{GT}|^2 (C_T C_A^* + C'_T C_A'^*) \right] \\
 &= -2\gamma \left[ |M_F|^2 (C_S C_V^* + C'_S C_V'^*) + |M_{GT}|^2 (C_T C_A^* + C'_T C_A'^*) \right] \\
 &= -2\gamma |M_F|^2 (C_S + C'_S) C_V^* + -2\gamma |M_{GT}|^2 (C_T + C'_T) C_A^* \\
 &= -2\gamma |M_F|^2 \cdot \frac{1}{\sqrt{2}} g_V \underbrace{(C_S + C'_S)}_{+\sqrt{2} g_S} + -2\gamma |M_{GT}|^2 \frac{(-1)}{\sqrt{2}} g_A \underbrace{(C_T + C'_T)}_{-\sqrt{2} g_T} \\
 &= -2\gamma |M_F|^2 \cdot g_V \cdot g_S - 2\gamma |M_{GT}|^2 \cdot g_A \cdot g_T \\
 \boxed{b \cdot \bar{z} = -2\gamma [ |M_F|^2 g_V g_S + |M_{GT}|^2 g_A g_T ]}
 \end{aligned}$$

~~BYE~~  $\gamma = (1 - \alpha^2 z^2)^{1/2}$

Figure C.3: "Notes 2"

To Match Up Holstein and JT W:

$$g_V = \frac{1}{\sqrt{2}}(C_V + C_V') ; \quad C_V = C_V' = \frac{1}{\sqrt{2}}g_V = \frac{1}{\sqrt{2}}$$

$$a_1 \approx g_V M_F$$

$$g_A = \frac{-1}{\sqrt{2}}(C_A + C_A') ; \quad C_A = C_A' = \frac{-1}{\sqrt{2}}g_A \approx \frac{-1}{\sqrt{2}}(0.91210) \quad c_1 \approx g_A M_{GT}$$

Also define:

$$g_S \equiv \frac{1}{\sqrt{2}}(C_S + C_S') ; \quad C_S = C_S' = \frac{1}{\sqrt{2}}g_S \approx 0$$

$$g_T \equiv \frac{-1}{\sqrt{2}}(C_T + C_T') ; \quad C_T = C_T' = \frac{-1}{\sqrt{2}}g_T \approx 0$$

Then, we find:

$$\dot{\xi} = |M_F|^2(g_V^2 + g_S^2) + |M_{GT}|^2(g_A^2 + g_T^2)$$

$$A_p \dot{\xi} = \frac{2}{5}|M_{GT}|^2(g_A^2 + g_T^2) + 2(\frac{3}{5})^{\frac{1}{2}}M_F M_{GT}(g_V g_A - g_S g_T)$$

$$b \cdot \ddot{\xi} = -2\gamma [ |M_F|^2 g_V g_S + |M_{GT}|^2 g_A g_T] ; \quad \gamma \equiv (1 - \alpha^2 \zeta^2)^{\frac{1}{2}}$$

$$(E) \rightarrow F_o(E) + |M_F|^2 g_S^2 + |M_{GT}|^2 g_T^2$$

$$F_i(E) \rightarrow F_i(E) + \delta_{uv} \left( \frac{u}{u+1} \right) (-2) \cdot M_F M_{GT} \cdot g_S g_T + \alpha_{uv} \left( \frac{1}{u+1} \right) |M_{GT}|^2 g_T^2$$

Figure C.4: "Notes 3"

- \* In some limits, Holstein and JT<sub>W</sub> are equivalent. For simplicity, we will require that JT<sub>W</sub>'s terms  $C_A, C_A', C_V, C_V', M_F$ , and  $M_{GT}$  are entirely real.
- \* The physical interpretation of this is that we ~~do not~~ require time-reversal symmetry to be obeyed.
- \* We use the following relationships:

$$\begin{aligned} \zeta &= f(E) \rightarrow |C_V|^2 = |M_F|^2 \cdot (|C_V|^2 + |C_V'|^2) \\ A_B \zeta &= f'(E) \rightarrow |C_V'|^2 = |M_{GT}|^2 \cdot (|C_A|^2 + |C_A'|^2) \\ \end{aligned}$$

use the later JT<sub>W</sub> sign convention.

$$\begin{aligned} |C_V|^2 &= 2 \cdot |M_{GT}|^2 \cdot \operatorname{Re}[C_A C_A'^*] \\ \operatorname{Re}[a_i^* C_V] &= -M_F M_{GT} \cdot \operatorname{Re}[C_V C_A'^* + C_V' C_A] \end{aligned}$$

- \* Then, via trial and error, we find that the following set of relationships gives consistent results:

$$\begin{aligned} C_V &= C_V'; & a_i &= \left( \pm \frac{1}{\sqrt{2}} M_F (C_V + C_V') \right) \\ C_A &= C_A'; & g_i &= \left( \mp \frac{1}{\sqrt{2}} M_{GT} (C_A + C_A') \right) \end{aligned} \quad \text{Thus far, either set of signs is consistent. But they must be opposite.}$$

- \* In our code, which evaluates Holstein, we use these:

$a_i \approx g_V M_F$	$M_F = 1.0$	$g_V = 1.0$	Note that we believe we know $M_F$ better than we know $g_A$ . So, to measure " $A_B$ ", we vary $g_A$ and leave $M_{GT}$ fixed.
$g_i \approx g_A M_{GT}$	$M_{GT} = -0.62376$	$g_A \approx 0.91210$	

- \* We'll define some quantities,  $\rho$ :

$$\rho_{JT\bar{W}} = \frac{C_A \cdot M_{GT}}{C_V \cdot M_F}; \quad \rho_{\text{Holstein}} = \frac{g_A \cdot M_{GT}}{g_V \cdot M_F} \approx -0.568931$$

\* This  $\rho_{JT\bar{W}}$  uses our own definition from PRL.

\* Note that  $A_B$  comes out physically wrong unless  $\rho_{JT\bar{W}}$  is  $\oplus$ , ie, in  $A_B$ , there's a term  $\sim [C_V C_A'^* + C_V' C_A]$  and we need the whole thing to come out  $\oplus$ .  $\therefore C_V$ 's and  $C_A$ 's must have opposite signs.

- \* We'll take the convention that every body has the same matrix elements:

$$\begin{aligned} M_{GT, JT\bar{W}} &= M_{GT, \text{Holstein}} \\ M_{F, JT\bar{W}} &= M_{F, \text{Holstein}} \end{aligned}$$

- \* Then:

$$\begin{aligned} C_V &= C_V' \Rightarrow \oplus \\ C_A &= C_A' \Rightarrow \ominus \end{aligned} \quad \text{This because at the end of the day, we want Holstein's } a_i \text{ to be } \oplus, \text{ and } g_i \text{ to be } \ominus, \text{ or else we don't produce the right physics.}$$

$g_V = \frac{1}{\sqrt{2}} (C_V + C_V') = 1.0$	$C_V = C_V' = \frac{+1}{\sqrt{2}} g_V = \frac{1}{\sqrt{2}}$
$g_A = \frac{-1}{\sqrt{2}} (C_A + C_A') \approx +0.91210$	$C_A = C_A' = \frac{-1}{\sqrt{2}} g_A \approx \frac{-1}{\sqrt{2}} (0.91210)$

Figure C.5: "Notes 4"

- \* In some limits, Holstein and JTW are equivalent. We require that JTW's terms  $C_A, C_A', C_V, C_V', M_F$ , and  $M_{GT}$  must all be entirely real. We can probably do this WLOG. (Or without very much loss of generality, at least.)
- \* Use the following relationships:

$$\xi = f_x(E) \rightarrow |q_i|^2 = |M_F|^2 (|C_V|^2 + |C_V'|^2)$$

$$|q_i|^2 = |M_{GT}|^2 (|C_A|^2 + |C_A'|^2)$$

$$A \cdot \xi = f_x(E) \rightarrow |C_V|^2 = 2 \cdot |M_{GT}|^2 \cdot \text{Re}[C_V C_A'^*]$$

$$\text{Re}[q_i] = -\text{Re}[M_F M_{GT} (C_V C_A'^* + C_V' C_A)] \leftarrow \text{later JTW convention.}$$

we'll only use this.

- \* Then, the following relationships give us internally consistent results:

$$\begin{aligned} C_V &= C_V' ; & q_i &= \pm \frac{1}{\sqrt{2}} M_F (C_V + C_V') \\ C_A &= C_A' ; & C_i &= \pm \frac{1}{\sqrt{2}} M_{GT} (C_A + C_A') \end{aligned} \quad \begin{array}{l} \text{either set of signs is consistent.} \\ \text{But they must be opposite.} \end{array}$$

Code has these signs for  $q_i$  and  $C_i$ .  
Do I know why?

- \* In our code (which evaluates Holstein), we use these values:

$\oplus$	$q_i \approx g_V M_F$	$M_F = 1.0$	$g_V = 1.0$
$\ominus$	$C_i \approx g_A M_{GT}$	$M_{GT} = -0.62376$	$g_A = 0.91210$

- \* We can also define:

$\rho_{\text{Holstein}} \equiv \frac{g_A M_{GT}}{g_V M_F} \approx -0.568931$	$\rho_{\text{JTW}} \equiv \frac{C_A M_{GT}}{C_V M_F} \leftarrow \text{we use } \rho_{\text{JTW}} \text{ def. in PRL.}$
--	--

- \* We do not get the correct JTW  $A_B$  unless we require that  $\rho_{\text{JTW}}$  is  $\oplus$ . Equivalently, we require that  $\text{Re}[M_F M_{GT} (C_V C_A'^* + C_V' C_A)]$  must be  $\oplus$ . But  $M_{GT}$  is  $\ominus$ !  $\rightarrow$  Option 1: Take  $M_{GT, \text{JTW}} = -M_{GT, \text{Holstein}}$ .  $\rightarrow$  Option 2: Take  $C_A = C_A'$  to be  $\ominus$ , and  $C_V = C_V'$  to be  $\oplus$ .

(really, there are other options.  
But let's leave  $M_F$  and  $C_V$  alone.)

- \* For Holstein to come out right, we need  $C_i$  to be  $\ominus$ , and  $q_i$  to be  $\oplus$ . I think.

$$\begin{aligned} g_V &= \frac{1}{\sqrt{2}} (C_V + C_V') = 1.0 \\ g_A &= \frac{-1}{\sqrt{2}} (C_A + C_A') = 0.91210 \Rightarrow C_A \text{ must be } \ominus \text{ then, bc } g_A \text{ is } \oplus \text{ and} \\ &\quad M_{GT, \text{Holstein}} \text{ is } \ominus, \text{ and we need } C_A \text{ to be } \ominus. \end{aligned}$$

- \* OK. Now what do I do with  $C_i$  and  $G_i$ ?  $\rightarrow$  can't just stick them into  $M_F$  and  $M_{GT}$ . even in JTW it doesn't come out consistent.
- \* Have to write JTW in Holstein notation so I can figure out where to put  $C_i, G_i$  in.

Figure C.6: "Notes 5"

## Appendix D

# Derivation of the $b_{\text{Fierz}}$ Dependence of the Superratio Asymmetry

Recall the integrated JTW probability distribution for outgoing beta particles from Eq. (B.3):

$$\begin{aligned} d^3\Gamma(E_\beta, \hat{\Omega}_\beta) dE_\beta d^3\hat{\Omega}_\beta &= \frac{2}{(2\pi)^4} F_{\mp}(Z, E_\beta) \xi p_\beta E_\beta (E_0 - E_\beta)^2 dE_\beta d^3\hat{\Omega}_\beta \\ &\times \left[ 1 + b_{\text{Fierz}} \frac{m_e c^2}{E_\beta} + A_\beta \left( \frac{\vec{J}}{J} \cdot \frac{\vec{p}_\beta}{E_\beta} \right) \right]. \end{aligned} \quad (\text{D.1})$$

We note that the only angular dependence remaining in this equation is the dot product between the direction of beta emission and the direction of nuclear spin-polarization. This allows us to pull out a further factor of  $2\pi$  by choosing the axis of polarization as defining our coordinate system, and integrating over the “ $\phi_\beta$ ” coordinate. The result is a bit more friendly to work with:

$$d^2\Gamma(E_\beta, \theta) dE_\beta d\theta = W(E_\beta) \left[ 1 + b_{\text{Fierz}} \frac{m_e c^2}{E_\beta} + A_\beta \frac{v_\beta}{c} |\vec{P}| \cos \theta \right] dE_\beta d\theta, \quad (\text{D.2})$$

where  $\theta$  is the angle between the beta emission direction and the polarization direction, and is the only angular dependence that remains. Here, we have grouped the overall energy dependence into  $W(E_\beta)$ , so that

$$W(E_\beta) = \frac{2}{(2\pi)^3} F_{\mp}(Z, E_\beta) \xi p_\beta E_\beta (E_0 - E_\beta)^2, \quad (\text{D.3})$$

where we note that the Fermi functions in the above make Eq. D.3 integrable only by numerical methods. Because it would be difficult to make this expression *more* challenging to work with, it is therefore easy enough to include in this expression any small corrections to overall energy dependence that might arise from e.g. recoil-order corrections, as described by Holstein [10].

In the TRINAT geometry with two polarization states (+/-) and two detectors (T/B) aligned along the axis of polarization, we are able to describe four different count rates, with different combinations of polarization states and detectors. Thus, neglecting beta scattering effects, we have:

$$r_{T+}(E_\beta) = W(E_\beta)\varepsilon_T(E_\beta)\Omega_T N_+ \left[ 1 + b_{\text{Fierz}} \frac{m_e c^2}{E_\beta} + A_\beta \frac{v}{c} |\vec{P}_+| \langle \cos \theta \rangle_{T+} \right] \quad (\text{D.4})$$

$$r_{B+}(E_\beta) = W(E_\beta)\varepsilon_B(E_\beta)\Omega_B N_+ \left[ 1 + b_{\text{Fierz}} \frac{m_e c^2}{E_\beta} + A_\beta \frac{v}{c} |\vec{P}_+| \langle \cos \theta \rangle_{B+} \right] \quad (\text{D.5})$$

$$r_{T-}(E_\beta) = W(E_\beta)\varepsilon_T(E_\beta)\Omega_T N_- \left[ 1 + b_{\text{Fierz}} \frac{m_e c^2}{E_\beta} + A_\beta \frac{v}{c} |\vec{P}_-| \langle \cos \theta \rangle_{T-} \right] \quad (\text{D.6})$$

$$r_{B-}(E_\beta) = W(E_\beta)\varepsilon_B(E_\beta)\Omega_B N_- \left[ 1 + b_{\text{Fierz}} \frac{m_e c^2}{E_\beta} + A_\beta \frac{v}{c} |\vec{P}_-| \langle \cos \theta \rangle_{B-} \right], \quad (\text{D.7})$$

where  $\varepsilon_{T/B}(E_\beta)$  are the (top/bottom) detector efficiencies,  $\Omega_{T/B}$  are the fractional solid angles for the (top/bottom) detector from the trap position,  $N_{+/-}$  are the number of atoms trapped in each (+/-) polarization state, and  $|\vec{P}_{+/-}|$  are the magnitudes of the polarization along the detector axis for each polarization state.  $\langle \cos \theta \rangle_{T/B,+/-}$  is the average of  $\cos \theta$  for *observed* outgoing betas, for each detector and polarization state combination. This latter term is approximately  $\pm 1$  as a result of our detector geometry, but contains important sign information. For a pointlike trap in the center of the chamber, 103.484 mm from either (DSSSD) detector, each of which is taken to be circular with a radius of 15.5 mm, we find that  $\langle |\cos \theta| \rangle_{T/B,+/-} \approx 0.994484$ , and is the same for all four cases. Note that a horizontally displaced trap will decrease the magnitude of  $\langle |\cos \theta| \rangle$ , but as it is an expectation value of an absolute value, all four will remain equal to one another. In the case of a vertically displaced trap, these four values will no longer all be equal, however it will still be the case that  $\langle |\cos \theta| \rangle_{T+} = \langle |\cos \theta| \rangle_{T-}$ , and  $\langle |\cos \theta| \rangle_{B+} = \langle |\cos \theta| \rangle_{B-}$ .

In the case of the present experiment, we note that  $|\vec{P}_+| = |\vec{P}_-|$  is correct to a high degree of precision.

We define the ‘superratio’,  $s$ , to be:

$$s = s(E_\beta) := \frac{r_{T+} r_{B-}}{r_{T-} r_{B+}}, \quad (\text{D.8})$$

and the ‘superratio asymmetry’,  $A_{\text{super}}$ , as

$$A_{\text{super}} = A_{\text{super}}(E_\beta) := \frac{1 - \sqrt{s}}{1 + \sqrt{s}} \quad (\text{D.9})$$

$$= \frac{\sqrt{r_{T-} r_{B+}} - \sqrt{r_{T+} r_{B-}}}{\sqrt{r_{T-} r_{B+}} + \sqrt{r_{T+} r_{B-}}} \quad (\text{D.10})$$

This is explicitly an experimental quantity that is measured directly by the above combination of count rates, however it is obvious that it reduces, under appropriate limits, to be equivalent to a naive asymmetry. In particular, if we require that the physical conditions and relative detector positions and sensitivities are identical when the polarization is flipped, then we have  $r_{T+}(E_\beta) = r_{B-}(E_\beta)$  and  $r_{T-}(E_\beta) = r_{B+}(E_\beta)$ . It follows that we can simplify the superratio asymmetry into a more intuitive quantity that we might use for a measurement with only a single polarization state, e.g.,

$$A_{\text{super},+} \rightarrow \frac{r_T - r_B}{r_T + r_B}. \quad (\text{D.11})$$

While Eq. D.11 is conceptually encouraging, the assumptions that gave rise to that expression are too simplifying. We will introduce some more limited assumptions for what follows, along with shorthand notation for improved readability. First, we require that the magnitude of the polarization vector is the same for both polarization states, and also that the average of the magnitude of  $\cos \theta$  for a given detector does not change when the polarization is flipped (equivalent to a requirement that the trap position doesn’t change when the polarization is flipped). Then:

$$P := |\vec{P}_+| = |\vec{P}_-| \quad (\text{D.12})$$

$$\langle |\cos \theta| \rangle_T := \langle |\cos \theta| \rangle_{T+} = \langle |\cos \theta| \rangle_{T-} \quad (\text{D.13})$$

$$\langle |\cos \theta| \rangle_B := \langle |\cos \theta| \rangle_{B+} = \langle |\cos \theta| \rangle_{B-}, \quad (\text{D.14})$$

and we can further define

$$c = \langle |\cos \theta| \rangle := \frac{1}{2} (\langle |\cos \theta| \rangle_T + \langle |\cos \theta| \rangle_B) \quad (\text{D.15})$$

$$\Delta c = \Delta \langle |\cos \theta| \rangle := \frac{1}{2} (\langle |\cos \theta| \rangle_T - \langle |\cos \theta| \rangle_B) \quad (\text{D.16})$$

and

$$\tilde{A} = \tilde{A}(E_\beta) := A_\beta \frac{v}{c} \quad (\text{D.17})$$

$$\tilde{b} = \tilde{b}(E_\beta) := b_{\text{Fierz}} \frac{mc^2}{E_\beta}, \quad (\text{D.18})$$

$$\tilde{r} = \tilde{r}(E_\beta) := 1 + \tilde{b}. \quad (\text{D.19})$$

With this new set of variables defined, we can re-write Eqs. (D.4-D.7) as

$$r_{T+}(E_\beta) = W(E_\beta) \varepsilon_T(E_\beta) \Omega_T N_+ [\tilde{r} + \tilde{A}P(c + \Delta c)] \quad (\text{D.20})$$

$$r_{B+}(E_\beta) = W(E_\beta) \varepsilon_B(E_\beta) \Omega_B N_+ [\tilde{r} - \tilde{A}P(c - \Delta c)] \quad (\text{D.21})$$

$$r_{T-}(E_\beta) = W(E_\beta) \varepsilon_T(E_\beta) \Omega_T N_- [\tilde{r} - \tilde{A}P(c + \Delta c)] \quad (\text{D.22})$$

$$r_{B-}(E_\beta) = W(E_\beta) \varepsilon_B(E_\beta) \Omega_B N_- [\tilde{r} + \tilde{A}P(c - \Delta c)], \quad (\text{D.23})$$

and the superratio becomes

$$s = \frac{(\tilde{r} + \tilde{A}Pc)^2 - (\Delta c)^2}{(\tilde{r} - \tilde{A}Pc)^2 - (\Delta c)^2} \quad (\text{D.24})$$

where all factors of  $W(E_\beta)$ ,  $\varepsilon_{T/B}(E_\beta)$ ,  $\Omega_{T/B}$ , and  $N_{+/}$  have been cancelled out entirely.

For simplicity we take  $\Delta c = 0$  in what follows. Although this is not strictly accurate within the present experiment, this assumption greatly simplifies the expressions that follow. Then, absent other corrections (*e.g.* backscattering, unpolarized background, ...), it is clear that if  $\tilde{b} = 0$  as in the Standard Model,

$$A_{\text{super}} = \tilde{A}Pc = A_\beta \frac{v}{c} |\vec{P}| \langle |\cos \theta| \rangle \quad (\text{D.25})$$

In the case where  $\tilde{b} \neq 0$ , we find that

$$A_{\text{super}} = \frac{\tilde{A}Pc}{1 + \tilde{b}} \quad (\text{D.26})$$

$$\approx \tilde{A}Pc(1 - \tilde{b} + \tilde{b}^2), \quad (\text{D.27})$$

where we have utilized the assumption that  $\tilde{b} \ll 1$ . Thus, to leading order in terms of  $\tilde{b}$ ,

$$A_{\text{super}} \approx A_\beta \frac{v}{c} |\vec{P}| \langle |\cos \theta| \rangle \left( 1 - b_{\text{Fierz}} \frac{mc^2}{E_\beta} \right). \quad (\text{D.28})$$